Universidad Nacional Mayor de San Marcos
Universidad del Perú. Decana de América

Dirección General de Estudios de Posgrado
Facultad de Ciencias Físicas
Unidad de Posgrado

Generación y propagación de maremotos producido por una distribución de fuente sísmica

TESIS

Para optar el Grado Académico de Doctor en Física

AUTOR

César Omar JIMÉNEZ TINTAYA

ASESORES

Carlos Augusto CARBONEL HUAMÁN

Juan Carlos VILLEGAS LANZA (Co-asesor)

Lima, Perú

2019

Referencia bibliográfica

Jiménez, C. (2019). *Generación y propagación de maremoto producido por una distribución de fuente sísmica*. Tesis para optar el grado de Doctor en Física. Unidad de Posgrado, Facultad de Ciencias Físicas, Universidad Nacional Mayor de San Marcos, Lima, Perú.

Hoja de Metadata

Universidad Nacional Mayor de San Marcos
(Universidad del Perú. Decana de América).

Facultad de Ciencias Físicas.

Unidad de Posgrado en Física

Título del Documento: "Generación y propagación de maremotos producido por una distribución de fuente sísmica"

Tipo de trabajo: Tesis

Para optar el Grado Académico de Doctor en Física

Autor: César Omar Jiménez Tintaya

Asesores:
Dr. Carlos Augusto Carbonel Huamán
Dr. Juan Carlos Villegas Lanza

Lima (2019)

Hoja de metadata complementaria

Código ORCID del autor:
Mg. César Omar Jiménez Tintaya: https://orcid.org/0000-0002-3671-4748

Código ORCID de los Asesores:
Dr. Carlos Augusto Carbonel Huamán: https://orcid.org/0000-0001-9465-8118
Dr. Juan Carlos Villegas Lanza: https://orcid.org/0000-0002-2772-1508

Grupo de Investigación:
Física de Cambios Ambientales y la Teledetección (LABTEL)

Ubicación geográfica donde se realizó la investigación:
Facultad de Ciencias Físicas - UNMSM

Año o rango de años que la investigación abarcó: 2015 al 2018

UNIVERSIDAD NACIONAL MAYOR DE SAN MARCOS
(Universidad del Perú, Decana de América)
FACULTAD DE CIENCIAS FÍSICAS
Vicedecanato de Investigación y Posgrado

UNIDAD DE POSGRADO

ACTA DE SUSTENTACIÓN DE TESIS PARA OPTAR EL GRADO ACADÉMICO DE DOCTOR EN FÍSICA

A los seis días del mes de setiembre del dos mil diecinueve, siendo las seis de la tarde, se reunió el Jurado Examinador, en el auditorio 304 de la Unidad de Posgrado de la Facultad de Ciencias Físicas de la Universidad Nacional Mayor de San Marcos, presidido por el señor Dr. Víctor Anthony García Rivera como presidente, y con la asistencia de los siguientes miembros del Jurado Examinador:

Dr. Víctor Anthony García Rivera	(Presidente)
Dr. Alberto Delgado Pérez	(Miembro integrante)
Dr. Juan Carlos Villegas Lanza	(Miembro integrante)
Dr. Carlos Carbonel Huamán	(Asesor)

Para la sustentación oral y pública del trabajo de Tesis para optar el Grado Académico de Doctor en Física, del Mg. **César Omar Jiménez Tintaya** con código Nº 15137001.

Después de darse lectura al expediente de Grado en el que consta haberse cumplido con todas las disposiciones reglamentarias, los señores Miembros del Jurado Examinador, atendieron a la exposición de la Tesis titulada:

 "Generación y propagación de maremotos producido por una distribución de fuente sísmica"

Y formuladas las preguntas, éstas fueron absueltas por el graduando.

Acto seguido, en privado, el Jurado Examinador procedió a la calificación. El Presidente determinó el promedio de la calificación, obteniendo como resultado de:

 Diesiocher... (18) Muy bueno.

A continuación el Presidente del Jurado Examinador recomienda que la Facultad de Ciencias Físicas proponga que se le otorgue el Grado Académico de Doctor en Física, al Mg. **César Omar Jiménez Tintaya.**

Siendo las *20 : 45* se levantó la sesión; recibiendo el graduando las felicitaciones de los señores Miembros del Jurado Examinador y público asistente.

Los Miembros del Jurado Examinador suscriben el Acta de sustentación de tesis en Lima, a los seis días del mes de setiembre del dos mil diecinueve.
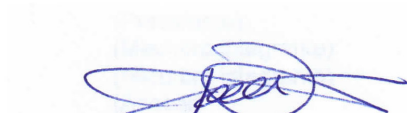

Lima, 06 de setiembre de 2019

... Acta de sustentación de Tesis del Mg. César Omar Jiménez Tintaya….
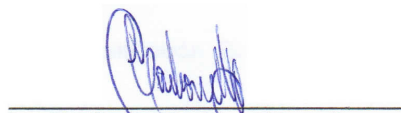
_____
Dr. Víctor Anthony García Rivera
Presidente

_____
Dr. Alberto Delgado Pérez
Miembro integrante

_____
Dr. Juan Carlos Villegas Lanza
Miembro integrante

_____
Dr. Carlos Carbonel Huamán
Asesor

Dirección: Ciudad Universitaria, Pabellón de Ciencias Físicas
Calle Germán Amézaga 375 – Cercado de Lima
Apartado Postal: 14-0149 – Lima 14 Perú

Unidad de Posgrado
Teléfono: 619-7000 Anexo 3802
E-mail postfis@unmsm.edu.pe

Resumen

"Generación y propagación de maremotos producido por una distribución de fuente sísmica"

por César Omar JIMÉNEZ TINTAYA

El Perú se encuentra ubicado dentro del Cinturón Sísmico del Pacífico, por lo que es una de las zonas sísmicas más activas del mundo. De acuerdo a la teoría de los gaps sísmicos, es muy probable la ocurrencia de un sismo tsunamigénico en la región central del Perú. En esta investigación se propone desarrollar una metodología para obtener la distribución de la fuente sísmica para sismos tsunamigénicos a partir de la inversión de formas de onda de tsunami y datos geodésicos.

Se plantea las aplicaciones a eventos sísmicos y tsunamis que han afectado el litoral costero peruano. Por ejemplo, el sismo y tsunami de Lima de 1940 (8.0 Mw), el sismo y tsunami de Huacho de 1966 (8.1 Mw), a partir de la inversión de 3 registros mareográficos. El sismo y maremoto de Camaná de 2001 (8.4 Mw) a partir de la inversión combinada de datos mareográficos y geodésicos. El sismo y maremoto de Pisco 2007 (8.0 Mw), a partir de la inversión de datos mareográficos. El sismo y maremoto de Chile 2014 (8.1 Mw) a partir de la inversión combinada de datos mareográficos y geodésicos. Se enfatiza la aplicación de la prueba de confiabilidad para evaluar la resolución y el rango de aplicación de los métodos sísmicos, mareográfico y geodésico.

Se ha implementado un procedimiento numérico para el pronóstico de parámetros del tsunami (máxima altura y tiempo de arribo) a partir de una base de datos de fuentes sísmicas unitarias pre-simuladas.

Los resultados de esta investigación permitirán obtener la distribución de las asperezas (zonas de mayor liberación de energía sísmica), lo cual permitirá desarrollar planes de prevención, previsión y mitigación de desastres por fenómenos naturales.

Abstract

"Generation and propagation of tsunami waves produced by a seismic source distribution"

by César Omar Jiménez Tintaya

Peru is located within the Pacific Seismic Belt, making it one of the most active seismic zones in the world. According to the theory of "seismic gaps", the occurrence of a tsunamigenic earthquake in the central region of Peru is very likely. In this research, it is proposed to develop a methodology to obtain the seismic source distribution for tsunamigenic earthquakes from the inversion of tsunami waveforms and geodetic data.

It considers the applications to seismic events and tsunamis that have affected the Peruvian coasts. For example, the 1940 Lima earthquake and tsunami (Mw 8.0), the 1966 Huacho earthquake and tsunami (Mw 8.1), from the inversion of 3 tsunami waveforms. The earthquake and tsunami of Camana of 2001 (Mw 8.4) from the joint inversion of tsunami and geodetic data. The Pisco earthquake and tsunami of 2007 (Mw 8.0), from the inversion of tsunami data. The earthquake and tsunami of Chile 2014 (Mw 8.1) from the joint inversion of tide and geodetic data. The application of the reliability test is emphasized to evaluate the resolution and the range of application of the seismic, tsunami and geodetic methods.

A numerical procedure to forecast the tsunami parameters (maximum tsunami height and arrival time) has been implemented from a database of pre-simulated seismic unitary sources.

The results of this investigation will allow to obtain the distribution of the asperities (zones of greater seismic energy release), which will allow to develop plans of prevention, forecast and mitigation of disasters by natural phenomena.

Acknowledgements

Contents

List of Figures

List of Tables

List of Symbols

CMT	"**C**entroid **M**oment **T**ensor"
CNAT	"**C**entro **N**acional de **A**lerta de **T**sunamis"
DART	"**D**eep Ocean **A**ssessment and **R**eporting of **T**sunamis"
DHN	"**D**irección de **H**idrografía y **N**avegación"
GEBCO	"**G**eneral **B**athymetric **C**hart of the **O**cean"
GNSS	"**G**lobal **N**avigation **S**atellite **S**ystem"
GPS	"**G**lobal **P**osittioning **S**ystem"
IGP	"**I**nstituto **G**eofísico del **P**erú"
InSAR	"**In**terferometry of **S**ynthetic **A**perture **R**adar"
IRIS	"**I**ncorporated **R**esearch Institutions for **S**eismology"
ITRF	"**I**nternational **T**errestrial **R**eference **F**rame"
LABFIT	"**LAB**oratorio de **FI**sica de la **T**ierra"
NEIC	"**N**ational **E**arthquake **I**nformation **C**enter"
SOAM	"**SO**uth **AM**erican"
UNESCO	"**U**nited **N**ations **E**ducational, **S**cientific and **C**ultural **O**rganization"
UNMSM	"**U**niversidad **N**acional **M**ayor de **S**an Marcos"
USGS	"**U**nited **S**tates **G**eological **S**urvey"
UTC	"**U**niversal **T**ime **C**oordinated"
TUNAMI	"**T**ohoku **U**niversity's **N**umerical **A**nalysis for Tsuna**M**i **I**nvestigation"

Dedicated to my beloved wife Monica, to my children: César Augusto and Rebeca Sofia and my parents: Héctor (RIP) and Herlinda ...

Chapter 1

Introduction

1.1 Background

Peru is located in the interaction zone of the tectonic plates of Nazca and South America, where the subduction process occurs, in which the Nazca plate is introduced below the South American continental plate at a relative speed of 6 to 7 cm/year (Kendrick et al., 2003; Norabuena et al., 1998) [Ken03]. This zone has a high seismicity, where large tsunamigenic earthquakes have been reported (Silgado, 1978) [Sil78]. A large percentage of the epicenters of earthquakes of intermediate to high magnitude occur in the sea, so the possibility of occurrence of tsunamis is high.

The occurrence of earthquakes is the result of the sudden slip of two fault planes, where tectonic forces and seismic energy accumulated by tens or hundreds of years are released by radiating seismic waves. The best way to characterize the rupture area of an earthquake is by studying the seismic source.

Historically, the first seismic source models were based on near field and far field seismic data. Near-field seismic data are usually not available, and when they are, good knowledge of the velocity structure of the crust is required, and high-frequency signals can not be modeled appropriately due to the local heterogeneity of the crust. This is one of the reasons why teleseismic signals are widely used, because for these epicentral distances (between 30° and 90°) the high frequency components are damped by the elastic medium (Ioualalen et al, 2013) [Iou13].

Since the 1990s, the tsunami waveform inversion has been applied "to obtain the distribution of the seismic source" (Satake and Kanamori, 1991) [Sat91], this methodology provides good results for the bandwidth of low frequencies or long periods. This methodology is useful for studying historical earthquakes that have generated tsunami waves, for which there are no

seismic signals, but with tsunami records that have recorded the event (such as the Huacho earthquake of 1966). However, with this method it is not possible to obtain the temporal evolution of the seismic source, using the old tide records, given that the sampling interval of the tide signals is 1 minute, which is comparable with the duration of the rupture process from the seismic source, which can last from a few seconds to a few minutes, depending on the magnitude of the seismic event.

In the last two decades, the geodetic data such as GPS (Global Posittioning System) and satellite images from InSAR (Interferometry of Synthethic Aperture Radar) have allowed to obtain important contributions to the knowledge about the geodynamic processes associated to the occurrence of earthquakes, since they can detect the displacements and the slow deformations in the long term, being very useful in the near field. Geodetic data can capture signals that may be omitted by seismic stations, especially for slow-slip propagation earthquakes that generate "tsunami earthquakes" or much slower transient displacements.

The importance of this research is framed within the generation of knowledge of hazard and risk for the prevention, forecasting and mitigation of a possible disaster by earthquake and tsunami, for which it is necessary to use numerical simulation models to represent the physical properties of the seismic source, the stresses and deformations of the crust for stratified media and the numerical models of the dynamics of tsunamis.

1.2 Objectives

General objectives

Study the seismic source of large tsunamigeni earthquakes using the tsunami waveforms recorded in the coastal tide gauges and buoys in the high seas as well as the shallow coseismic displacements of the earth's crust recorded by the GPS geodetic stations, with the purpose of obtaining the physical parameters that characterize the seismic source.

Study the physics of the generation of large tsunamigenic earthquakes, by calculating the deformations of the crust in the near field and of the waves of the tsunami in the regional field.

Development of a methodology to determine the physical parameters of the seismic source model from a joint inversion process of tsunami and geodetic data.

Implementation of a computational system to forecast the parameters of a tsunami from a database of pre-simulated seismic unit sources.

Particular objectives

Evaluation of seismic, geodetic and tidal data sources to be used in the investigation. Evaluation of numerical simulation models of tsunamis.

Digital processing of geophysical data: seismic, geodetic and tidal. Software implementation for data processing.

Application of the methodology to study earthquakes of magnitude (greater than Mw 7.5) of nearby-origin tsunami that have affected Peru since 1940 to the present, emphasizing the events of the 21st century because they are better recorded instrumentally.

Study the effects of the generation of tsunami waves in the near field, such as the variation of sea level (by uplift or coseismic subsidence) due to the occurrence of large earthquakes and the impact of the respective tsunami.

1.3 Problem statement

How is the area with the greatest release of seismic energy (and with the greatest impact) within the rupture area for large-scale tsunamigenic earthquakes (greater than 7.0 Mw) identified? For the purposes of reactive management it is important to know the area with the greatest impact of the earthquake and tsunami event since this area of greater impact is not always in the vicinity of the epicenter, because the rupture area can reach up to more than 500 km in length in the case of the central region and the southern region of Peru.

Due to the geographical location of Peru within the Pacific Seismic Belt, which corresponds to a highly seismic zone, every certain interval of years there is an earthquake of great magnitude (Mw > 7.0) that can generate a tsunami. Therefore, it is necessary to study the seismic source or slip distribution to obtain information from the deformations field. The deformation field would be used as an initial condition for the simulation of the propagation of the respective tsunami. In that sense, the tsunami modelers would have more realistic (and reliable) information for their respective investigations.

The importance of solving the problem lies in the fact that its application will allow taking the appropriate actions to effect the forecasting, prevention and mitigation of disasters due to large earthquakes and floods caused by the tsunami along the Peruvian coast.

1.4 Study cases

The history of the last 500 years shows that Peru has been affected by many earthquakes that have generated tsunami waves [Sil78]. Among the most important historical mega-events are: the earthquake and tsunami of Callao 1746 [Jim13] [Dor90] and the earthquake and tsunami of Tacna in 1868 (Beck and Ruff, 1989) [Bec89].

Within the last 80 years (for which there are events recorded instrumentally), there are the following events that have generated tsunami waves (near and regional) that have affected (to a lesser or greater degree) Peru (Figure 1.1):

a) Earthquake of Lima Peru, May 24, 1940
b) Earthquake of Lambayeque Peru, Nov 20, 1960
c) Earthquake of Huacho Peru, Oct 17, 1966
d) Earthquake of Lima Peru, Oct 03, 1974
e) Earthquake of Chimbote Peru, Feb 21, 1996
f) Earthquake of Nazca Peru, Nov 12, 1996
g) Earthquake of Camana Peru, Jun 23, 2001
h) Earthquake of Pisco Peru, Aug 15, 2007
i) Earthquake of Maule Chile, Feb 27, 2010
j) Earthquake of Iquique Chile, Apr 01, 2014 (can be considered as a near field for southern Peru).

In fact, as of the year 2000, the availability of seismic, tsunami and geodetic data of good quality and free available in the global network, suggests the investigation of the events of Camana 2001, Pisco 2007 and Chile 2014.

1.5 State of the knowledge on research of seismic sources

Peru, throughout its history, has suffered the recurrent impact of disasters caused by seismic phenomena. The solution to this problem requires the knowledge of the physical properties of the terrestrial globe, properties and physical processes of the seismic sources, of the appropriate distribution of data acquisition systems in the territory, implementation of qualified software to process the huge amount of data and metadata, and meet the requirements of society by anticipating the occurrence of dangerous events to take preventive measures. Seismic sources are places where seismic waves are generated that shake the Earth's terrain and interior, and cause associated phenomena such as tsunamis, geological faults, coseismic luminescence, etc.
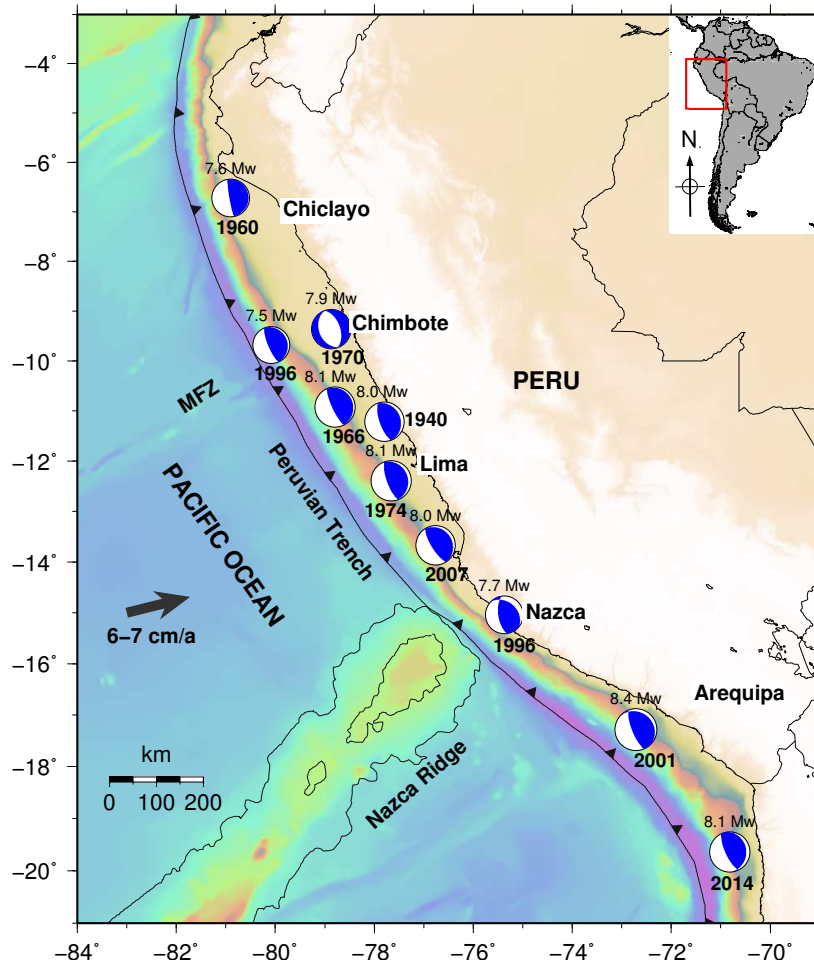
FIGURE 1.1: Seismic events that have generated tsunamis (in the near field) that have affected Peru from 1940 to 2014. The main tectonic units are also shown, such as: the marine trench, the Mendaña Fracture Zone (MFZ) and the Nazca ridge. The Nazca plate converges at a speed of 6 to 7 cm/year.

In the PhD Program in Physics of the "Universidad Nacional Mayor de San Marcos" (UN-MSM): Line of research in Earth Sciences, progress is being evaluated in the characterization and description of the numerical data inversion processes of earthquakes recorded in the far field for the characterization of seismic sources (Kikuchi and Kanamori, 1991) [Kik91]. The results show that the most of the software considers models based on elastic media, with limits of resistance to fracturing or friction, rupture propagation with finite velocities, simple rupture surfaces, unimodal or multimodal rupture mechanisms, that satisfy the waveforms recorded in seismograms-accelerograms, mareograms (Satake and Kanamori, 1991) [Sat91], continuous GPS records in the near field, radar image interferograms, etc.

The characterization of the great majority of seismic sources results from the inversion of the seismic waveforms of the far field, long period waves recorded at epicentral distances between 30º and 90º. The inversion of the long-period waves of the far field minimizes the effects of the heterogeneity of the terrestrial globe. The inversion of high frequency seismic waveforms from the near field of earthquakes requires detailed information on the structure of

the earth's crust in the epicentral zone, usually not available. Continuous GPS records have extended the frequency range of seismic instrumentation. These systems document seismic phenomenology from finite displacements in the near field to relatively high frequencies of ground vibrations [Iou13].

The frontier of knowledge in the numerical modeling of seismic sources goes through into the development of the theory of rheological behavior of non-elastic materials, evaluation of the rheological constants of the crust and upper mantle using the recovery of the post-seismic deformation pattern from GPS data and the inversion of seismograms, tsunami waveforms, geodetic data and satellite radar images InSAR [Wan12].

Currently, several geophysical inversion models have been developed to get the distribution of the seismic source and the parameters that characterize it:

a) Wave inversion model of strong motion accelerograms (near field). It is necessary to have a good model of velocity structure of the crust [Jor02].

b) Inversion model of teleseismic waves for epicentral distances greater than $30°$ (far field) [Kik91].

c) Tsunami waveform inversion model (near and regional field), which includes coastal tide stations and buoys located offshore [Sat91].

d) Geodetic inversion model with GPS + InSAR data + field observations on the coast: uplift and/or subsidence (in the near field) [Bar90].

e) Joint inversion model, that uses two or more data sets (seismic, geodetic and tide gauge) [Sat93].

Most of these models are based on the theory of propagation of seismic waves in a stratified elastic medium and in the theory of deformation for an elastic medium, homogeneous and semi-infinite (Okada, 1992) [Oka92]. In the case of the inversion of tsunami waves, it is based on the linear theory of wave propagation in shallow waters. In this research it is proposed to model the deformation for an elastic medium, heterogeneous and stratified by layers; model the propagation of tsunami waves with a linear and non-linear theory with sponge oceanic boundary conditions to avoid reflection at oceanic boundary or open boundary.

At the national level, researchers from the "Instituto Geofísico del Perú" (IGP) have applied models to obtain the focal mechanism from inversion of seismic waves (Tavera and Buforn, 2001). Villegas (2014) has obtained the distribution of the coefficient of interseismic coupling from the inversion of GPS geodetic data for the subduction zone of Peru. On the other hand, researchers from the "Laboratory of Earth Physics" (UNMSM), such as Jiménez et al. (2014), have published their results on the determination of the seismic source or distribution of the dislocation (slip) of the 2007 Pisco earthquake from tsunami waveform inversion [Jim14].
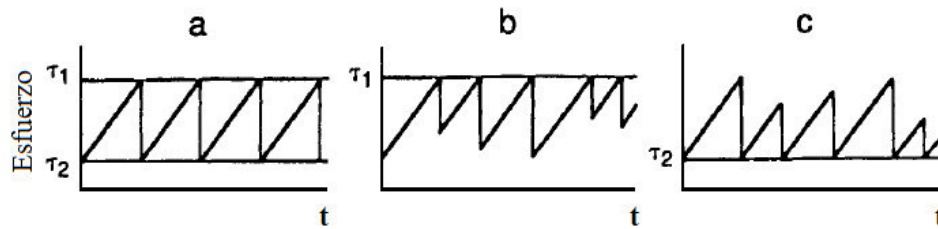
FIGURE 1.2: Relationship of the stress as a function of time for different types of seismic cycle: a) Regular model, b) Predictable time model, c) Predictable slip model. (Modified from Lay and Wallace, 1995).

The process of seismic recurrence in subduction zones

This process is also known as the *seismic cycle*. However, when talking about *cycle* implicit reference is made to the concept of frequency or periodicity, which implies the predictability of large seismic events, which does not yet occur at present. Therefore, large seismic events are not cyclical but recurrent over time.

In general, subduction zones produce the largest earthquakes worldwide. Almost all large shallow earthquakes (of magnitude greater than 7.0 Mw) are not isolated or episodic events, but occur in pre-existing faults. This implies that the great majority of earthquakes represent a repetition of the rupture of an established fault (Lay and Wallace, 1995) [Lay95].

In the last two decades, satellite geodesy has revolutionized the vision of deformation of the crust between large consecutive earthquakes. "The small time window of modern measurements requires comparative studies of subduction zones that are in different stages of the deformation process" (Wang et al., 2012) [Wan12]. The types or models of the seismic cycle are shown in Figure 1.2, and are classified into: a) Regular model, where the dislocation in the fault would be the same for each event and the recurrence interval would be constant. b) Predictable time model, when τ_1 is constant the fall of stress can vary from event to event, so the time to the next event is variable, this time can be obtained from the time-displacement line for a movement of stationary fault and c) Predictable slip model, where stresses in the fault are always relaxed at a constant value τ_2 (Lay and Wallace, 1995) [Lay95].

The tectonic plates, which have a quasi-rigid and elastic nature at the same time, are floating on the upper mantle or asthenosphere, which is considered as a highly deformable solid with visco-elastic rheological properties.

A subduction zone can be locked for hundreds of years accumulating stress and elastic energy and then suddenly tectonic stress can be released to produce an earthquake. After a large earthquake in the subduction zone, 3 primary processes take place (Wang et al., 2012) [Wan12]:

a) The post-seismic slip (afterslip) continues in the direction of the slip of the main shock.
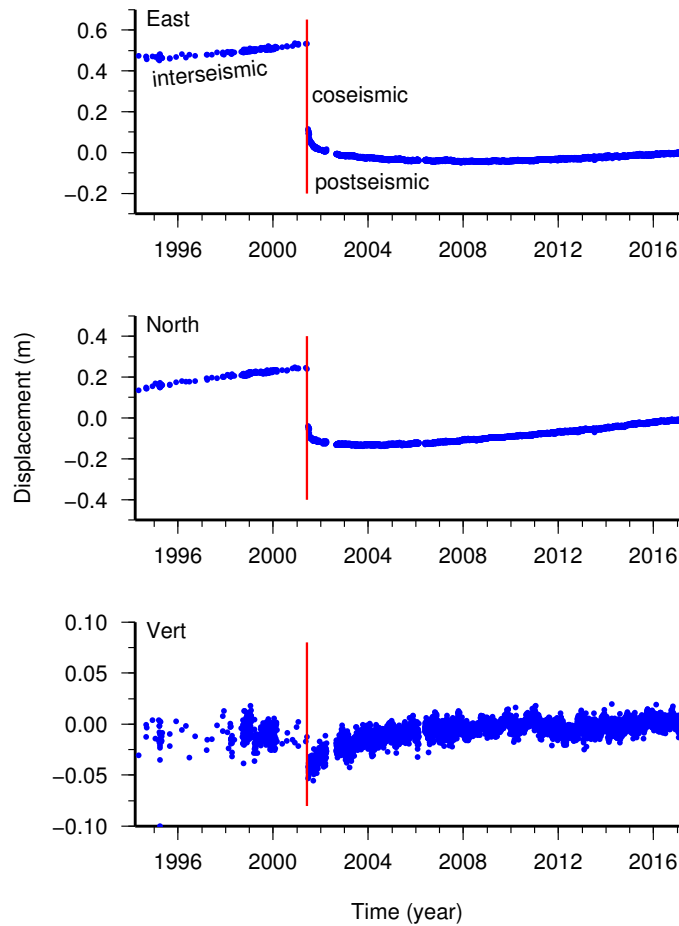
FIGURE 1.3: Geodetic signal of the Arequipa station (AREQ). The discontinuity (red line) corresponds to the coseismic displacement produced by the earthquake of Camana 2001 (Mw 8.4). Notice that the noise has greater amplitude in the vertical component.

b) Viscoelastic relaxation of the tectonic forces occurs and the slip changes to the opposite direction.

c) The rupture zone is locked again, starting a new process of seismic recurrence (or seismic cycle).

In Figure 1.3, we can see the 3 components of the time series of the geodetic station of Arequipa (AREQ), from 1994 to 2017, with a time window of more than 23 years. The discontinuity (vertical red line) corresponds to the occurrence of the Camaná earthquake of 2001 (Mw 8.4). The process of seismic recurrence in subduction zones can be divided into 3 phases:

a) Interseismic phase: can last tens or hundreds of years (elastic deformation) before the next big earthquake occurs. It is a secular regime process. The slope of the displacement graph (Figure 1.3) represents the interseismic velocity (which has displacements in the order of mm to cm per year), which is an important parameter for the calculation of the coefficient of interseismic coupling.

b) Coseismic phase: it can last in the order of seconds to a few minutes depending on the magnitude of the earthquake, this duration is related to the time of the rupture process of the seismic source. It is a process of transitory regime. The amplitude of the discontinuity of the graph in Figure 1.3 represents the coseismic displacement (in the order of several cm to meters).

c) Post-seismic phase: "it starts immediately after the occurrence of the earthquake and can last in the order of months to a few years" depending on the magnitude of the earthquake [Wan12]. The dynamics of this process is governed by the equations that govern the viscoelastic rheological behavior of the upper mantle; In general, the rheology of Burgers is used to model this process.

There are several representative models that explain the dynamics of interaction between the lithosphere and the asthenosphere to explain the post-seismic phase of the seismic recurrence process [Wan12], for example:

a) One-dimensional model of tectonic stress diffusion.

b) Maxwell viscoelastic bi-dimensional rheological model.

c) Burgers viscoelastic three-dimensional rheological model.

Also, the technology of observation and measurement of the displacements and deformation of the earth's crust has developed rapidly. A few decades ago, the geodetic measurements of deformation of the crust were made mainly by the leveling method. Currently, deformation of the crust is measured by the GPS satellite system or by interferometry of radar satellite images (InSAR) [Wan12].

Topics to be investigated

There are several topics currently that have not been investigated in their entirety, which will be addressed in this doctoral research. For example:

1. The variation of the physical properties (coefficient of rigidity and density) of the elastic medium (lithosphere) with respect to the depth for the calculation of the coseismic deformation will be approached: elastic model stratified by layers. This topic is not considered in current researches, most of them are based in the Okada model [Oka92].

2. In the case of the theory of tsunami propagation waves, we will review the problems of computational reflection effects in the open boundaries (because it is one of the fragile points in the current numerical models), non-linear effects of the waves at the arrive at the coast, etc.

3. In the case of geodetic data, the problem of the correction by attenuation of the deformation with respect to the epicentral distance will be addressed, which is why in many studies an underestimated seismic moment has been obtained.

4. It is also important to perform a reliability test of the model with synthetic data, in which a seismic source is simulated, obtaining the mareograms and synthetic displacements for the different stations. Then the inversion of the synthetic data is conducted and it is evaluated if the original distribution can be reproduced with a certain approximation.

1.6 General outline of the Thesis

Chapter I corresponds to the introduction and overview of the thesis, in which the background of the research topic is stated, the objectives of the Thesis are presented, the state of knowledge is described in terms of the seismic source and finally, the topics to be investigated are described.

Chapter II describes the theory of geophysical inversion: the forward problem and the inverse problem. The algorithm of the generalized inversion method and the non-negative least squares method are described, which is widely used in applications. The reliability test is described to evaluate its applicability for a given seismic event.

From Chapter III the applications to seismic events and tsunamis that have affected the Peruvian coast are presented. For example, in this chapter the earthquake and tsunami of Lima of 1940 (Mw 8.0) is studied. An important result is that the first period of tsunami waveforms from linear and non linear models fits with a very good correlation. This fact allows the use of linear equations in tsunami waveform inversion, where only the first period is used.

In Chapter IV, the 1966 Huacho earthquake and tsunami (Mw 8.1) is studied. The slip distribution is obtained from the inversion of 3 tsunami waveforms of the Peruvian tidal network. The tsunami moment agrees very well with the seismic moment for a corresponding magnitude of Mw 8.1.

Chapter V studies the Camaná earthquake and tsunami of 2001 (Mw 8.4) based on the joint inversion of tsunami and geodetic data. This is the only event in Peru for which the post-seismic process can be studied from the time series of displacements (1994-2017) of the geodetic station of Arequipa.

Chapter VI studies the earthquake and tsunami of Chile 2014 (Mw 8.1) based on the joint inversion of tsunami and geodetic data. A reliability test is applied to evaluate the resolution

and range of application of the tsunami and geodetic method. Emphasis is given to methods of obtaining geodetic deformation.

Chapter VII describes "a numerical model to forecast the parameters of a tsunami from a database of pre-calculated seismic unit sources" [Jim18]. This procedure is used in the Pre-Tsunami application, coded in Matlab, which is useful in the National Tsunami Warning Center (CNAT) of Peru.

Finally, Chapter VIII describes the Discussion and Conclusions of the investigation. The discussion focuses on the role played by the number and dimensions of the subfaults within the inversion process and the optimization of the numerical model of wave propagation through open ocean boundary conditions to avoid numerical reflection.

Chapter 2

Inversion theory of geophysical data to obtain slip distribution

In this chapter, we review the inversion theory applied to the geophysical processes to obtain the slip distribution of the seismic source. The forward method and the inverse method are described. The generalized inversion method and the non-negative least squares method are explained. The reliability indicators of the inversion process are important because they allow knowing the level of reliability of the results of the inversion. The inversion method of tsunami waveforms and geodetic data is explained, as well as the joint inversion of 2 data sets. Finally, the chessboard reliability test is described, which allows to conduct a synthetic test with the available data.

2.1   Introduction

In general, a signal (data set or time series) contains information about the physical process that generates the phenomenon, the medium by which the disturbance (waves) has propagated and the instrument by which the signal has been recorded. If the effect of the properties of the medium and the parameters of the instrument are known and removed, it is possible to determine the parameters of the phenomenon that generated the process (source), from the observed signals or data.

An alternative to the use of seismic data to study the "seismic source of an earthquake is the use of the tsunami waveforms and the coseismic displacements" recorded by the GPS geodetic stations or by the InSAR satellite interferometry images. "When an earthquake occurs, seismic waves propagate through the interior of the Earth and are recorded by seismic stations as time series" (Johnson and Satake, 1997) [Joh97]. Since the 1960s, earthquakes
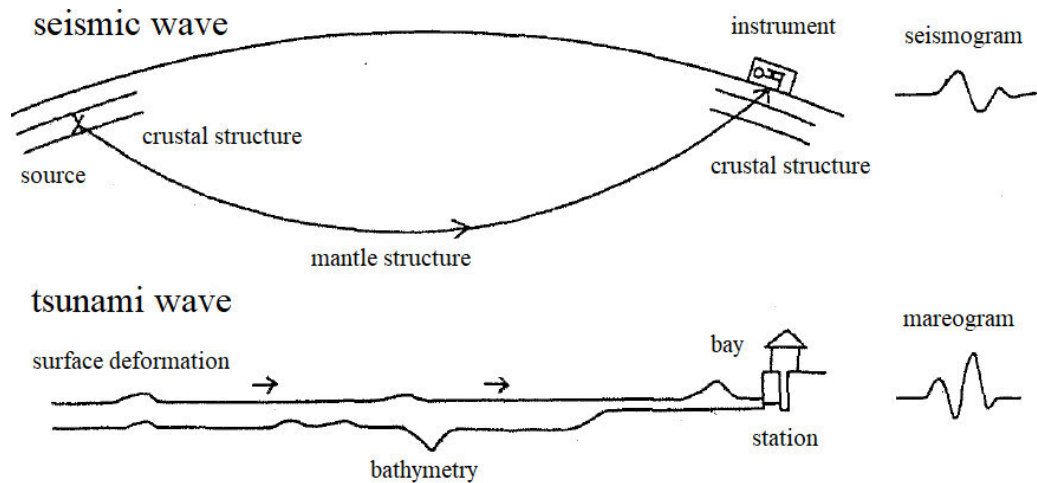
FIGURE 2.1: Comparison of propagation and records of seismic and tsunami waves in the context of inversion process (modified from Satake, 1987).

in Peru have been recorded by the global seismic network. Figure 2.1 compares the use of seismic data and tsunami data.

Seismic signals contain information about the seismic source, but they also depend on the structure of the Earth through which the seismic waves propagate and the instrument by which they are recorded. Similarly, "when an earthquake generates a tsunami, the waves of the tsunami propagate through the ocean and are recorded as waveforms on the tide gauges located in bays and ports or on buoys in the high seas" (Johnson and Satake, 1997) [Joh97]. Similar to seismic waves, the waveforms of the tsunami contain information about the seismic source, the effects of propagation on the ocean and the instrument by which they are recorded. For seismic waves, the most important effect on propagation is the velocity structure of the Earth; for tsunami waves, the most important effect on the propagation is the depth of the ocean (bathymetry), since the speed of the waves depends on the bathymetry. Of these two factors, "the bathymetry is better known than the velocity structure of the Earth" (Satake and Kanamori, 1991 [Sat91]); therefore, propagation effects can be simulated more accurately by computational methods for tsunamis than for seismic waves. Once the effects of propagation and the instrument have been taken into account, the waveforms of the tsunami can be used to determine the parameters of the seismic source (Johnson, 1999) [Joh99].

2.2 Inversion theory

"Inversion theory is an organized set of mathematical techniques to obtain information from data about the physical world on the basis of inferences inferred from observations. Observations of the physical world consist of a tabulation of measurements or data" (Menke,
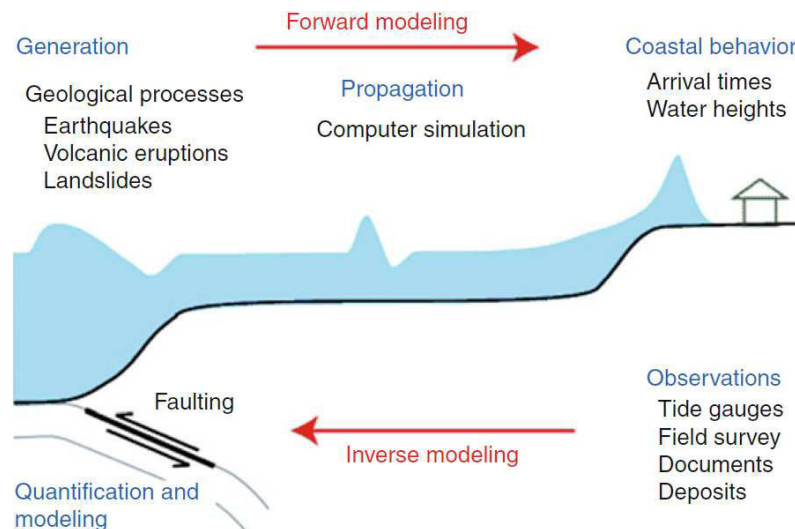
FIGURE 2.2: Explanatory diagram of the geophysical inversion process (modified from Satake, 2015).

1989). The questions to be answered are established in terms of numerical values of properties specific to the physical world, which are known as model parameters. "It is assumed that there is some specific method (usually a theory or mathematical model) that relates the parameters of the model with the data" (Menke, 1989) [Men89].

In the inverse problems, there is a mathematical relationship that links the observed data (which will be called the data vector) with the parameters of the model that we want to know (which will be called the *model*).

Figure 2.2 shows the Physics of the forward process and the inverse process. In the first case, from the parameters of the source and the tsunami propagation equations, it is possible to predict some parameters such as the arrival time and the wave height at a point of observation, including the synthetic mareogram in that observation point. While in the second case, from the data observed in one or several observation points and taking into account the equations that govern the system (propagation of tsunami waves), the parameters of the model that characterize the seismic source are estimated.

Forward method

"The term inverse theory is used in contrast to forward theory which is defined as the process of predicting measurement results based on a general principle or model and a set of initial conditions relevant to the problem in question" (Menke, 2018) [Men18].

The forward method is the procedure by which data is generated that can be compared with observations. When a forward model is found to approximate the observed data, it is

considered that the model describes the problem's physics quite well. Mathematically, it can be described in matrix notation:

$$G_{ij} \times m_j = d_i \tag{2.1}$$

Where G (Green functions or transfer functions matrix) is an operator that applies to the parameter model m to obtain the data vector d. The vector of the model m has N_j parameters (unknowns that we want to know), for each dislocation (or *slip*) of the subfaults. The data vector d contains the information of the observed data: the tidal signals, geodetic data or seismic signals, i represents the i -th data (station or observation point) and j represents the j-th unknown, in particular to the slip or dislocation of the j-th subfault (Tarantola, 2005) [Tar05].

In general, the forward procedure consists of assuming an initial model m_0, and obtaining by direct calculation the simulated data vector d_s, then it is compared with the observed data vector d_i and the result is adjusted by successive iterations until obtaining the minimum residual R previously determined (equation 2.2).

$$R = |G_{ij}m_j - d_i|^2 \to 0 \tag{2.2}$$

The generalized inversion method

In the inversion theory, the inverse problem is determined starting from the data and from a model or general principle; then the estimation of the parameters that characterize the physical model is conducted. In most cases, there are more equations (or data) than unknowns $(N_i > N_j)$, which represents an overdetermined problem, being the solution non-unique. In this case, the G matrix is not square, so formally it has no inverse.

From the equation 2.1, multiplying by the transpose of G (that is, G^T or G') to each member of the equation:

$$(G'G) \times m = G'd \tag{2.3}$$

The equation 2.3 is a very useful form called "normal equations". Now $G'G$ is a square matrix, so it has an inverse (provided it is not singular). Also $G'G$ is a symmetric matrix, which means that its eigenvalues are real and non-negative and its eigenvectors are mutually perpendicular. Therefore, we can write an equation of the form:

$$m = (G'G)^{-1}G'd \tag{2.4}$$

Where $G^{-g} = (G^T G)^{-1} G'$ it is called the generalized inverse of G. Strictly speaking, this is the inverse by least squares; if it is non-singular, then it will be the generalized inverse. The equation 2.4 provides the best solution from the point of view of least squares, since the error square is minimized. The equation 2.4 is one of the most important equations in Geophysics for both linear and non-linear problems. In general, most of the problems that arise are non-linear. Thus, m will only serve as a correction of the initial model, so the inversion process should be repeated iteratively, with G updated for the new model in each iteration until the error is lower at a certain value (Lay and Wallace 1995) [Lay95].

The non-negative least squares method

Although the least squares problem is well defined and a solution is guaranteed, this solution may not be physically acceptable. For example, most shallow and large-scale seismic events (Mw > 7.0) in subduction zones have a reverse fault focal mechanism, so the dislocation vector (*slip vector*) points in the same direction. The least squares solution can contain both positive and negative values for m_j, which would be an unrealistic solution. To avoid this mathematically correct, but physically absurd solution because the dislocation in the seismic source can not be negative, the non-negative least squares method should be used (Lawson and Hanson, 1974) [Law74]. This method requires, as a condition, that the solution of all values m_j be positive or zero (equation 2.6):

$$R = |G_{ij} m_j - d_i|^2 \to 0 \tag{2.5}$$

$$m_j \geq 0 \tag{2.6}$$

The numerical algorithm is encoded in the subroutine in Fortran *nnls.f* cited in [Law74], the file can be downloaded from www.netlib.org. There is also a Matlab function *lsqnonneg.m*, which has been included in the coding of the inversion program.

Reliability and error calculation indicators

Correlation coefficient

The correlation coefficient is a measure of the linear relationship between two quantitative random variables (equation 2.7). Less formally, the correlation coefficient is defined as an index that can be used to measure the degree of similarity of two signals or time series. In general, this coefficient varies between -1 and +1. The value +1 represents a perfect correlation and the value -1 represents a perfect anticorrelation. The closer the unit is to the

value of this coefficient, the better the similarity between the variables and signals observed and simulated.

$$r_{xy} = \frac{N \sum (x_k y_k) - \sum (x_k) \sum (y_k)}{\sqrt{N \sum [x_k]^2 - [\sum (x_k)]^2} \sqrt{N \sum [y_k]^2 - [\sum (y_k)]^2}} \qquad (2.7)$$

Where N is the data number, $i = 1..N$, x and y represent the set of data or time series of signals to be compared.

Normalized variance

To evaluate the similarity between the waveforms of the observed and simulated signal, we calculate the value of the relative square-root error of the simulated amplitude with respect to that observed (Kikuchi et al., 1993) [Kik93].

The normalized variance (also called error or residual) is defined in the equation 2.8. This parameter indicates the degree of global reliability of the inversion process [Kik93].

$$Var = \frac{\sum_{j=1}^{N_j} \sum_{i=1}^{N_i} [d_i - G_{ij} m_j]^2}{\sum_{i=1}^{N_i} (d_i)^2} \qquad (2.8)$$

Where N_i is the data number and N_j is the number of unknowns (subfaults). The smaller the value of the normalized or residual variance, the better the correlation between the observed and simulated data.

The "delete half jack knife" method

There is no analytical expression for the calculation of errors in the non-negative least squares method, so a technique different from statistical methods should be used. Tichelaar and Ruff (1989) developed the jack knife technique [Tic89]. This method is a resampling technique designed to avoid the problem inherent in the determination of errors from the minimum squares method. A fixed number j of random data is deleted from the set of n data, which produces a resampling of data that is inverted to obtain the parameters of the model. This procedure is repeated several times, theoretically until all the possible combinations of $(n-j)$ resampling have been inverted. Errors are simply the standard deviations of the result of each inversion multiplied by the scale factor: $\sqrt{(1 + k - p)/(n - k)}$, where $k = n - j$ and p is the number of model parameters (ie. the number of subfaults). When half of the data is deleted, the scale factor is unitary [Tic89].
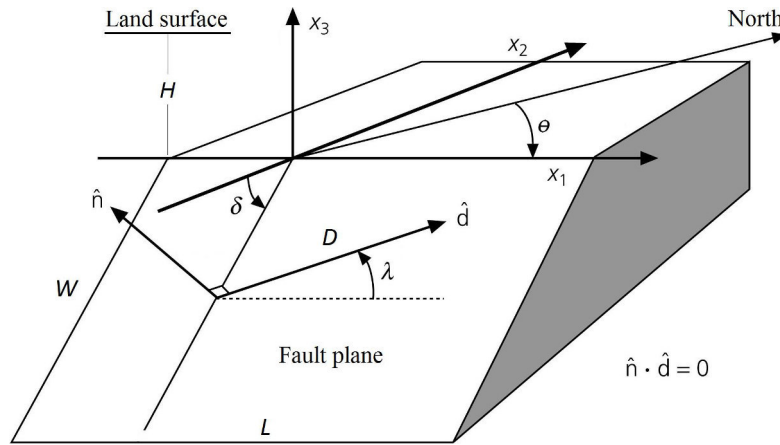
FIGURE 2.3: Parameters of the geometry of the seismic source. The Cartesian system X_1 X_2 X_3 does not match the geographic system (modified from Stein and Wysession, 2003).

2.3 Inversion of tsunami waveforms

The speed of the tsunami (linear wave of long period, in the order of minutes), is much lower than any type of seismic wave or rupture speed of the seismic source. The velocity of the P wave in the upper mantle is about 8 km/s, while the velocity of the tsunami wave for a depth of 4 km, for example, is 0.2 km/s. This difference is important for the formulation of the method of inversion (Satake, 1987) [Sat87].

The inversion of tsunami waveforms can be used to study earthquakes that occur in the ocean, but naturally can not be used for earthquakes that occur in the continent. In some cases, the rupture area may cover part of the ocean and part of the continent, so, in this case, tsunami data and geodetic data are combined to better constrain the parameters of the seismic source [Joh99].

The calculation of Green functions (elementary mareograms) using the finite difference scheme would be the forward problem. This requires specifying the initial conditions of the tsunami, including the amount of slip or dislocation of the rupture (usually a unitary slip) to generate the synthetic tsunami waveforms.

There are many parameters of the seismic source (focal mechanism, dimensions of the rupture area, location and depth of the source and the slip or dislocation) for which the tsunami waveforms should be inverted (Figure 2.3). However, if we try to invert for all parameters, the m space model would be very complex. The problem would be underdetermined and the parameters of the model could not be determined in a unique way. To avoid this problem, the values of the focal mechanism and the dimensions of the rupture area are fixed and inverted only to determine the value of the slip or dislocation [Joh99].

The parameters of focal mechanism can be taken from the catalog of the Global CMT (website: www.globalcmt.org) or by calculation of teleseismic waveforms inversion. "The

dimensions of the rupture area of large earthquakes can be determined from the distribution of the aftershocks within the first day" (Kanamori, 1977) [Kan77]. This leaves only one parameter to be calculated: the slip or dislocation. The dislocation is associated with the seismic scalar moment of the earthquake, which is a measure of the size of an earthquake. The relationship between the seismic moment and the slip or dislocation is given by:

$$M_0 = \mu L W D \tag{2.9}$$

Where M_0 is the scalar seismic moment, μ is the average rigidity of the elastic medium, L is the length of the rupture area, W is the width of the rupture area and D is the slip or dislocation.

For large-scale earthquakes, the slip distribution over the rupture area is not homogeneous, but it can be heterogeneous and constituted by several asperities or zones of greater seismic energy release. The inversion method (of tsunami data and geodetic data) of this investigation can determine the distribution of the asperitues on the rupture plane.

The seismic rupture area "is divided into several smaller subfaults (Figure 2.4). The parameters of the source, such as the depth and the focal mechanism for each subfault, correspond to the parameters of the source of the earthquake". The deformation of the ocean floor for each subfault is calculated with a unitary slip (*slip*=1 m). "This dislocation is used as an initial condition to calculate the synthetic tsunami waveforms, or Green functions, for each subfault. The result is a Green function for each subfault for each observation point" (location of the tidal station).

It is assumed that the tsunami waveforms observed in the tide gauges are a combination or linear superposition of the synthetic elementary tsunamis of each subfault (Green functions), in this way, "the unknown slip or dislocation for each Green function, can be calculated by solving the linear equation" $G_{ij}(t) \times m_j = d_i(t)$ [Sat87], or explicitly (equation 2.10):

$$
\begin{pmatrix}
\begin{pmatrix}
G_{11}(t_1) & G_{12}(t_1) & ... & G_{1j}(t_1) \\
G_{11}(t_2) & G_{12}(t_2) & ... & G_{1j}(t_2) \\
... & ... & ... & ...
\end{pmatrix} \\
\begin{pmatrix}
G_{21}(t_1) & G_{22}(t_1) & ... & G_{2j}(t_1) \\
G_{21}(t_2) & G_{22}(t_2) & ... & G_{2j}(t_2) \\
... & ... & ... & ...
\end{pmatrix} \\
\vdots \quad \vdots \quad \vdots \quad \vdots \\
\begin{pmatrix}
G_{i1}(t_1) & G_{i2}(t_1) & ... & G_{ij}(t_1) \\
G_{i1}(t_2) & G_{i2}(t_2) & ... & G_{ij}(t_2) \\
... & ... & ... & ...
\end{pmatrix}
\end{pmatrix}
\times
\begin{pmatrix}
m_1 \\
m_2 \\
\vdots \\
m_j
\end{pmatrix}
=
\begin{pmatrix}
\begin{pmatrix}
d_1(t_1) \\
d_1(t_2) \\
...
\end{pmatrix} \\
\begin{pmatrix}
d_2(t_1) \\
d_2(t_2) \\
...
\end{pmatrix} \\
\vdots \\
\begin{pmatrix}
d_i(t_1) \\
d_i(t_2) \\
...
\end{pmatrix}
\end{pmatrix}
\tag{2.10}
$$
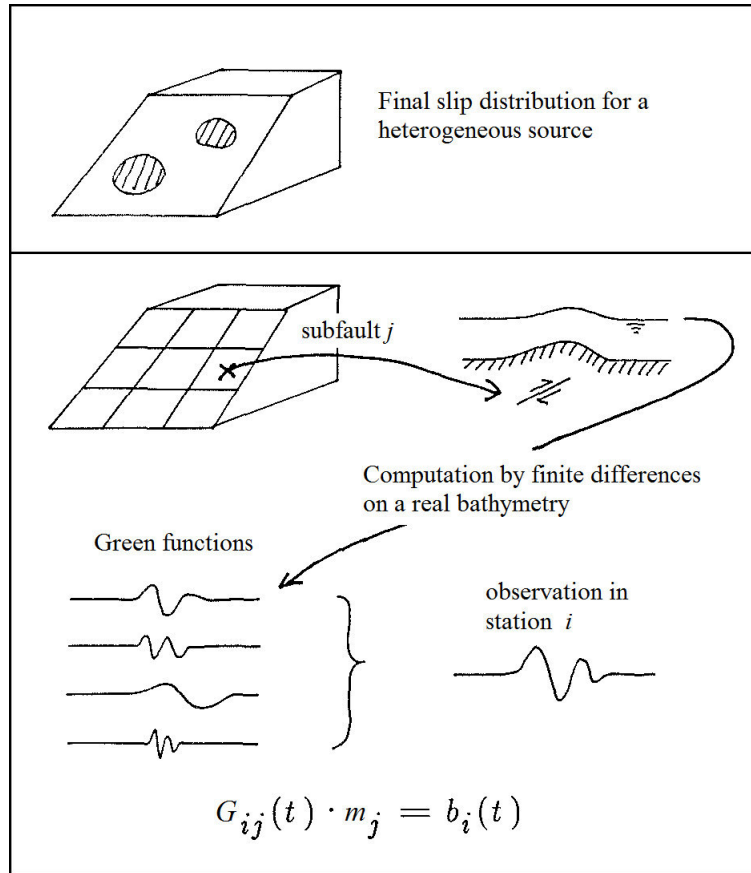
FIGURE 2.4: Explanatory diagram of the tsunami inversion process (modified from Satake and Kanamori, 1991).

Where $G_{ij}(t)$ is the array of functions of Green for the tidal station i due to the dislocation of the subfault j, $d_i(t)$ is the tsunami waveform observed in the tide gauge i, and m_j is the dislocation (or slip) of the subfault j. In general, this is an overdetermined problem because there is more data than unknowns (Menke, 1989) [Men89]. "The equation 2.10 is solved by applying the non-negative least squares method, which minimizes the square of the difference between the observed and synthetic waveforms, with the condition that all dislocations must be positive or zero" (Lawson and Hanson, 1974) [Law74]. The "unknowns" would be the dislocations of each subfault, resulting in the distribution of the asperities on the rupture plane.

2.4 Inversion of geodetic data

In the 1990s, "geodetic measurements using satellites became popular and these data were used in joint inversion to constrain the slip distribution. Only the final distribution (without temporal evolution) can be estimated using geodetic data". "These data can be combined with seismic signals or tsunami signals to better constrain the slip distribution". Examples of

geodetic data acquisition methods are triangulation, leveling, field observation of subsidence or offshore survey, GPS and InSAR radar interferometry (Ide, 2007) [Ide07].

Following the previous methodology, the seismic rupture area is divided into several smaller fragments (Figure 2.4). Also, the parameters of the source (such as focal mechanism and depth for each subfault) correspond to the parameters of the seismic source. The deformation field of the crust for each subfault is calculated for a unitary slip or dislocation ($slip = 1$ m), by means of the analytic equations of Okada (1992) [Oka92] or for an elastic medium stratified by layers (Wang et al. al., 2003) [Wan03]. These unitary dislocations are used to calculate Green's functions, for each subfault. The result is a unitary dislocation or Green function for each subfault for each observation point (location of the geodetic station, field observation point or InSAR).

Here, it is assumed that the displacements observed in the geodetic records (GPS, field observations or InSAR) are a linear superposition of the Green functions, in this way, the unknown dislocation or slip for each Green function, can be calculated solving the linear equation 2.1: $G_{ij} \times m_j = d_i$. To solve this equation the non-negative least squares method is also used.

As a restriction, this method should be applied only for geodetic stations in the near field to obtain a good resolution in the distribution of asperities (because the coseismic displacements in the regional or distant field are rapidly attenuated and are negligible).

2.5 Joint inversion process

When there are 2 data sets (eg, tsunami and geodetic), the equations 2.1 and 2.10 are modified in the following way:

$$\begin{pmatrix} G_t \\ G_g \end{pmatrix} \times m = \begin{pmatrix} d_t \\ d_g \end{pmatrix} \tag{2.11}$$

Where G_t represents the tsunami Green function, d_t the tsunami waveforms, G_g represents the geodetic Green function and d_g the coseismic displacements in its three components: north, east and vertical.

After combining the available data sets and the geodetic and tsunami Green functions, "the joint inversion is conducted using the non-negative least squares method, which compares

the simulated data with the observed data and minimize the square of the residual" [Law74]:

$$|G_{ij}m_j - d_i|^2 \to 0 \qquad (2.12)$$

With the condition $m_j \geq 0$. Due to the fact that the tidal stations are located in ports and bays, "it is advisable to consider the part of the tsunami signal corresponding to the first period of the wave to avoid problems of contamination of the signal with reflection effects and local resonances, due to the bathymetry and morphology of the coast around each station. So, for purposes of calculating the inversion, a time window is taken around a period from the beginning of the arrival of the wave" (Jimenez et al., 2014) [Jim14].

According to Jimenez et al., (2014): "The algorithm guarantees that all the values of the slip or dislocation are positive, as a necessary condition from the physical point of view. However, from the mathematical point of view it will not be the most optimal result" [Jim14].

2.6   Reliability test

The test of reliability or chessboard test consists of conducting the simulation of a synthetic seismic source with a distribution in the form of a chessboard. The mareograms are computed numerically in the corresponding tidal stations and/or the geodetic displacements in the appropriate observation points, then random noise is added to 5 percent of the amplitude of the signal. Finally, the inversion process of the synthetic data is carried out in order to reproduce the original distribution with a certain approximation (Figure 2.5).

From the application of the reliability test, it is evaluated and concluded that it is possible to reconstruct a complex process of seismic rupture with the tsunami and geodetic data available, taking into account that the azimuthal distribution of the tsunami stations and geodetic observation points be adequate.

Reliability test of tsunami inversion

Using this technique, it is possible to answer questions such as: How many tide stations, at least, is required to recover the original distribution of the seismic source? To what extent does the distribution of the gauge stations affect the calculation of the inversion?

It is possible to reconstruct a complex rupture process with only 3 tidal records, with an adequate azimuthal distribution of the stations, as was done by An et al. (2014) [Anc14] for the seismic source of the 2014 Chilean tsunami, by inverting tsunami data from only 3 DART stations. Similarly, with the tsunami records of only 3 coastal tidal stations, the distribution
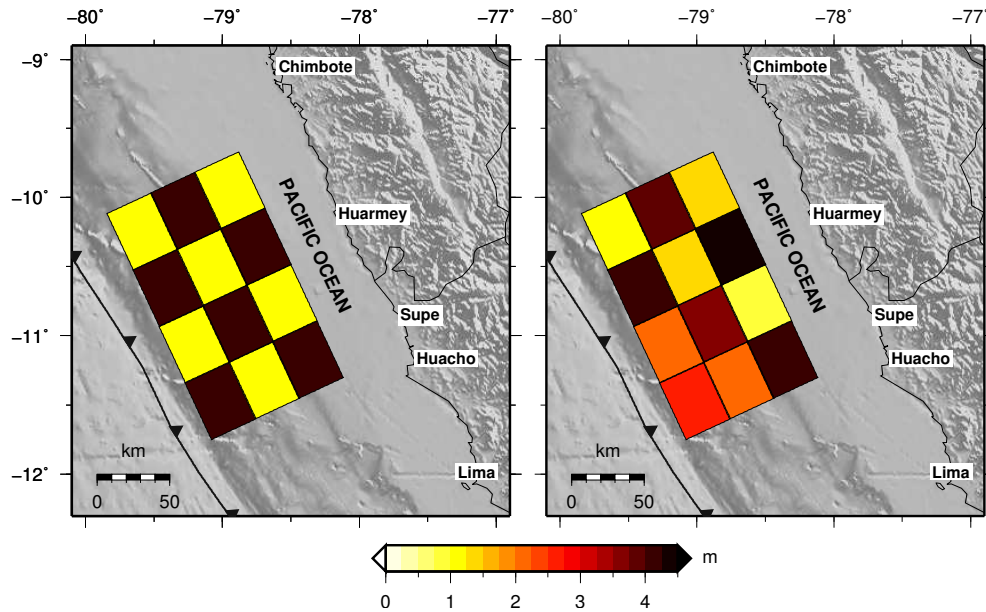
FIGURE 2.5: Reliability test for the 1966 Huacho earthquake: a) Distribution of the synthetic source in the form of a chessboard. b) Result of the inversion process.

of the seismic source of the 1966 Huacho earthquake was estimated (Jimenez et al., 2016) [Jim16].

Reliability test of geodetic inversion

To what extent can the geodetic stations located on the continent resolve the dislocation of the asperities located near the trench? Many investigations maintain that the GPS data from coastal stations does not resolve well the dislocation or slip of the asperities located on the side of the trench or far from the coast.

This statement may be true for a small event of magnitude Mw 7.0 to 8.0, but for earthquakes greater than Mw 9.0, with a dislocation of 20 to 50 m and coseismic displacements of several meters, this hypothesis will not be so true.

One way to solve this question is to conduct a reliability test of the chessboard for a virtual event of magnitude Mw 7.0, 8.0 and 9.0 and evaluate if the original distribution can be recovered after the inversion process.

Considering a resolution of the GPS data to the millimeter, one could generate synthetic displacements with an accuracy of 3 decimals (to the millimeter) to see if the dislocation or slip on the side of the trench is solved or not and to what extent.

2.7 Conclusions

In this review, the inversion theory of geophysical data has been explained (basically, using tsunami data and geodetic data) to obtain the slip distribution of the seismic source of a tsunamigenic earthquake.

In any geophysical inversion process, it is necessary to apply the forward method (to calculate the Green functions or time series and synthetic data) and the inverse method (to conduct the inversion of the time series and observed data).

It is worth noting the importance of the joint inversion of two data sets, which allow a better constrain of the solution with respect to the solution obtained from a single data set.

The reliability test (for example, the chessboard test) allows a synthetic test with the available data and allows to evaluate if it is possible to recover the original pattern of the seismic source.

Chapter 3

Numerical simulation of the 1940 Lima-Peru earthquake and tsunami (Mw 8.0)

In this chapter, it was conducted a numerical simulation to obtain the seismic source, coseismic deformation field and the tsunami propagation of the great Lima-Peru 1940 earthquake and tsunami, based on macroseismic information and focal mechanism from the literature. The seismic dimensions of our preferred model were set at 162×71 km^2 according to VIII isoseismal intensity. The slip distribution is homogeneous with a mean value of 2.7 m. The fault plane orientation was set at strike=330°, dip=20° and rake=90°. The maximum simulated uplift was 1.27 m and the maximum subsidence was 0.36 m. Due to the proximity of the seismic source to the coast, the city of Huacho was uplifted around 11 cm. The fault plane of the 1940 earthquake was located in the updip near the coast. The maximum tsunami height simulated in Huacho was 1.80 m. We suggest that there is a high tsunamigenic potential near the trench to generate a shallow earthquake.

3.1 Introduction

Based on macroseismic effects and historical information, it is posible to obtain the parameters of the seismic source using tsunami numerical modeling and an iterative approximation method to fit the results with observations (Jimenez et al., 2013). This technique is useful when there is not much geophysical information (seismic recordings, tsunami waveforms and geodetic data). Of course, the results would be a first approximation and must be considered with caution. For the 1940 Peruvian earthquake and tsunami, we only have macroseismic

information and some seismic data such as the focal mechanism obtained from old analogic seismic recordings (Beck and Ruff, 1989) [Bec89].

Several near field and far field tsunamis have impacted on the coast of central Peru region; for instance, 1960 and 2010 Chile tsunami, 2011 Japan tsunami, etc. However, the last 2017 Mexico tsunami has not impacted appreciably on Peruvian coasts (Ren, et al., 2018 [Ren18]; Jimenez, 2018 [Jim18b]).

On May 24, 1940, at 11:35 local time (16:35 UTC), the city of Lima and nearby towns were shaken by an earthquake, the maximum intensity of which was felt with VIII MM in Huacho. The shaking was felt from Guayaquil Ecuador to the north to Arica Chile to the south. It generated the destruction of many facilities in Lima, Callao, Chorrillos, Barranco, Chancay and Lurín. This earthquake left a balance of 179 dead and 3500 injured. The port of Callao suffered considerable damage due to the earthquake. In Chancay, 60 km north of Lima, damage to buildings was comparable to those observed in Lima. In Huacho, 130 km north of Lima, and in Lurin, 20 km south of Lima, the damages were minor and comparable to each other (Silgado, 1978) [Sil78].

Silgado (1978) has compiled a catalogue or database of earthquakes for Peru from ∼1500 (16th century) based on a recopilation of historical documents and observation field. According to Silgado (1978): "after the earthquake there was a small tsunami, in Ancon the sea retreated about 150 m, left the dock dry and filled slowly flooded land and passed over the defense wall of the pier, flooding the hangars of the Air Base, the phenomenon of the retreat of the sea was observed in La Punta, Callao and Pisco" [Sil78].

Background of previous research

The 1940 seismic event has been poorly studied due to the lack of seismic recordings of good quality, poor location of aftershocks, missing of tsunami waveforms and antiquity of the event (1940). However, Silgado (1978) reported the effects, damages on facilities and intensities in Lima and other cities; the isoseismal map is important, where the isoline of VIII bounds from Paramonga (to the north) until Lurín-Lima (to the south), (Figure 3.1).

Kanamori (1977), in his research about the energy released in great earthquakes, assigns to the 1940 Peruvian event a seismic moment of 2.5×10^{21} Nm equivalent to a magnitude of Mw 8.2, based on the aftershocks distribution and macroseismic effects [Kan77].

Lockridge (1985), in her report about tsunamis in Peru and Chile, reports a runup of 2 m, probably in Callao, due to the 1940 Peruvian tsunami [Loc85]. According to Beck and Nishenko (1990): "for the 1940 earthquake, there is a poorly documented report of a small (2 m) near field tsunami, and no report of a far field observation".
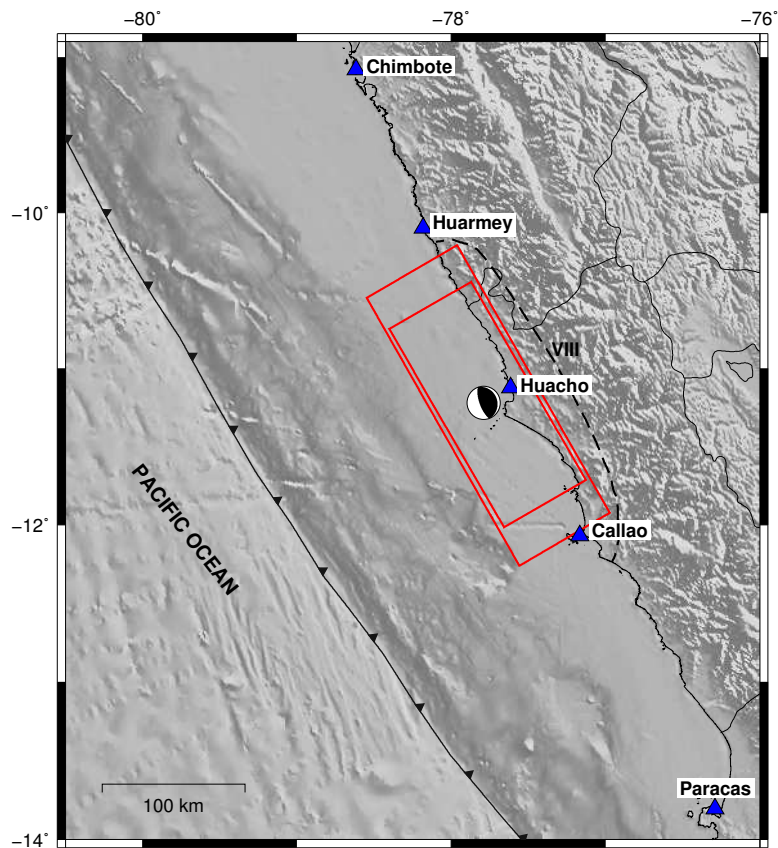
FIGURE 3.1: The larger red rectangle represents the fault geometry of event Mw8.2 according to VIII isoseismal intensity (dashed line), the smaller red rectangle represents the fault geometry of event Mw8.0. The focal diagram is located at the epicenter. The blue triangles represent the tidal stations.

Beck and Ruff (1989) recognize that there is very little information about the 1940 earthquake and the instruments constant and magnification factors of old seismographs are not always reliably known. They have calculated the focal mechanism of the 1940 earthquake (Table 3.1), which is an inverse fault type on the megathrust from teleseismic recordings of 8 stations. They obtained a simple source time function with one main pulse of moment release, the total duration of the rupture process was 30 s. The location of the asperity for the 1940 earthquake (to the south and near the epicenter) is estimated from the duration of the pulse of seismic moment release They demonstrated that this was an interplate earthquake and finished the debate in those years about the nature of the seismic rupture of this event [Bec89].

Beck and Nishenko (1990) stated that the 1940 earthquake was smaller than the 1966 (Mw 8.1) and the 1974 (Mw 8.1) events. A comparison of the P wave seismic recordings of 1940 and 1942 earthquakes indicates that the 1942 (Mw 8.2) event was approximately twice the size of the 1940 earthquake. We must take into account that twice the seismic moment corresponds to a difference of 0.2 in magnitude, therefore we can assign a moment magnitude of the Mw 8.0 to 1940 earthquake [Bec90].

TABLE 3.1: The hypocentral parameters of the 1940 Peru earthquake were recalculated by Dewey (according to Beck and Ruff, 1989). The focal mechanism was calculated by Beck and Ruff (1989).

Date	24 May 1940
Origin Time	16:35 UTC
Latitude	-11.22°
Longitude	-77.79°
Depth	10-30 km
Magnitude	8.0 - 8.2 Mw
Strike	$\theta = 340°$
Dip	$\delta = 20°$
Rake	$\lambda = 90°$

Dorbath et al. (1990) obtained "an empirical relation between the rupture length and the seismic moment" of great historical earthquakes in Peru. They suggested "that rupture zones are adjacent to regions of substantial destruction; in terms of isoseismal curves, the latter coincide roughly with the areas inside the isoseismal curve of intensity VIII" [Dor90]. So, they assigned a fault geometry dimension of 220 km length for the 1940 Peruvian earthquake.

Okal et al., (2006), conducted an evaluation of tsunami risk from regional earthquakes at Pisco-Peru. They simulated the 1940 tsunami source of parameters: 125 km length, 90 km width and a slip of 5.5 m, obtaining a runup of 0.8 m at Pisco [Oka06].

In this research, the seismic source of the 1940 Lima earthquake has been modeled (as a homogeneous slip distribution) for 2 seismic scenarios based on the seismic moment and focal mechanism given by Kanamori (1977) [Kan77] and Beck & Ruff (1989) [Bec89] respectively. The rupture geometry is based on the isoseismal of VIII according to Dorbath et al. (1990) [Dor90]. Then, the coseismic deformation pattern is calculated to obtain the coseismic displacements vectors and to simulate the tsunami propagation on a real bathymetry.

Seismotectonic setting of Central Peru

The ocurrence of great earthquakes (Mw>7.0) in Peru is a consequence of the subduction of the Nazca Plate under the South American Plate, with a convergence velocity of 6-7 cm/y [Nor98]. The Central region of Peru is bounded by two tectonic elements: the Mendaña Fracture Zone to the north and the Nazca Ridge to the south, separated by a distance around 600 km. These tectonic elements act as a barrier for propagation of the seismic rupture (Figure 3.2). The seismic profile in the Central Region of Peru indicates a flat or normal subduction, with absence of Quaternary volcanic activity (Barazangi, 1976) [Bar76].
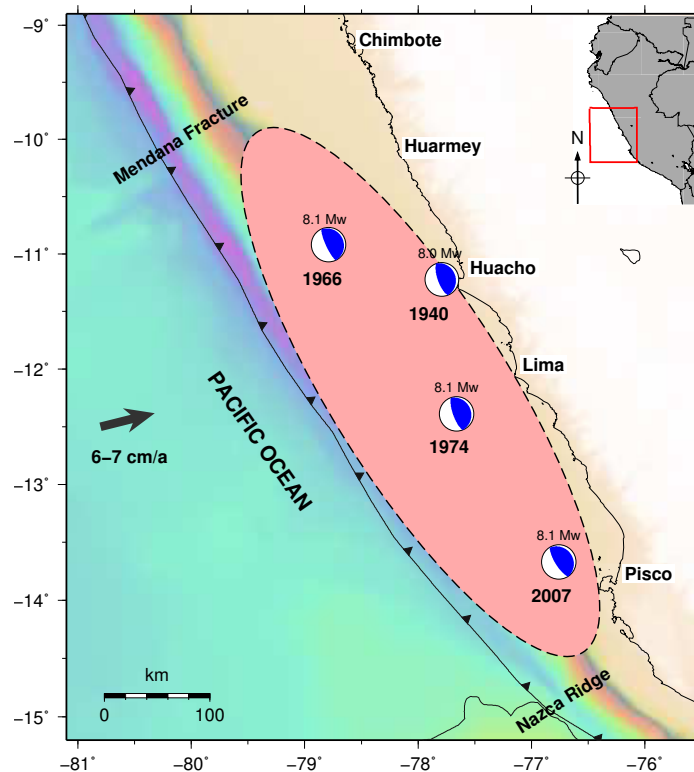
FIGURE 3.2: Seismotectonic setting of the Central Peru region. The pink ellipse represents the fault geometry of 1746 Callao earthquake (∼Mw 9.0). The focal diagrams represent the locations of events of the seismic sequence of 20th and 21st centuries.

The great tsunamigenic earthquakes (of shallow focal depth) are distributed, in general, between the coastline and the trench. In the history of Peru, there were several of these megathrust earthquakes and tsunamis generated in Peru and reported from the 16th century by the spanish conquerors (Dorbath et al., 1990 [Dor90]; Silgado, 1978 [Sil78]):

On July 9, 1586, a big earthquake destroyed the city of Lima, its main buildings collapsed. There were 22 victims. There was a collapse of rocks and stones on the hills, as well as cracks in the ground. The destruction spread to the valleys near Lima to Ica. This great earthquake was followed by a tsunami that flooded much of the coast. In Callao, the sea rose around 4 m and flooded part of the town. The shaking of the earthquake was felt from Trujillo in the north to Caraveli-Arequipa to the south [Sil78].

On October 20, 1687, two earthquakes ocurred in Lima, the first one at 16:15 (local time) and the second one at 17:30 approximately. The last event was the strongest and of greater duration. There were 100 dead due to the earthquake. The buildings were so damaged that people had to spend the night in stores in the square. The destruction was so great in the port of Callao and surrounding areas, the ruins extended to the south, especially in the valleys of Cañete, Ica, Palpa and Nazca. The tsunami was generated by the second earthquake. In the port of Callao 300 people died. The tsunami entered the harbor above the walls, causing 2 ships to run aground. The destrution caused by the tsunami was massive from Chancay

to Arequipa. The port of Pisco was destroyed by the earthquake and suffered great flooding because of the tsunami.

On October 28, 1746, a big earthquake destroyed the cities of Lima and Callao at 22:30 (local time). In Lima, around 3000 houses and buildings were destroyed, only 25 houses remained standing. A big tsunami destroyed the port of Callao, of the 5000 inhabitants only 200 people survived the tsunami. The shaking of the earthquake was felt from Guayaquil-Ecuador in the north to Tacna-Peru in the south. The magnitude of this megathrust earthquake was estimated in Mw 9.0 (Jimenez et al., 2013 [Jim13]; Mas et al., 2014 [Mas14a]).

After the ocurrence of the great ∼Mw9.0 megathrust earthquake and tsunami of Callao 1746, which destroyed the city of Lima and inundated the port of Callao (Jimenez et al., 2013), there was a quiescent period of around 200 years until the seismic event of Lima 1940 (Mw 8.0), which initiated the seismic sequence of the Central region of Peru, followed by the Huacho earthquake of 1966 (Mw 8.1), Lima 1974 (Mw 8.1) and Pisco 2007 (Mw 8.1) (Ioualalen et al., 2013; Jimenez et al., 2014). The seismic ruptures of all these events have been generated within the rupture geometry of the 1746 Callao earthquake (around 550 km length, from Mendaña fracture zone to Nazca Ridge). According to Beck and Nishenko (1990): "the mode of great earthquake rupture along the Central Peru subduction zone has changed" from big historic earthquakes (∼Mw 9.0) to smaller 20th and 21st century earthquakes (∼Mw 8.0) [Bec90].

Chlieh et al. (2011) and Villegas et al. (2016) argued that assuming that the current rate of change of the seismic moment deficit is stationary, then the accumulated moment since 1746 indicates that the occurrence of a large similar seismic event would be delayed, even considering that half of the seismic moment deficit was released asesimically there is still enough energy to reproduce an event similar to the 1746 earthquake.

The accumulation of the seismic moment released by the 1940 (Mw 8.0), 1966 (Mw 8.1), 1974 (Mw 8.1) and 2007 (Mw 8.1) seismic sequence represents only around 20% of the accumulated moment deficit since 1746 (∼Mw 9.0), suggesting that a significant amount of seismic moment would still be released in this segment of more than 550 km from the Nazca ridge to the Mendaña fracture zone.

3.2   Data

The geophysical data, as tsunami waveforms, geodetic displacements, seismic recordings of good quality and aftershocks distribution, are not available for the 1940 Peruvian historical event. However, Beck and Ruff (1989) have worked with seismic recordings from ancient

TABLE 3.2: The fault plane parameters of the 1940 Peru earthquake for 2 seismic scenarios considered in this research. $(X0, Y0)$ is the position of the lowerside corner of the source geometry.

Parameter	Event Mw 8.0	Event Mw 8.2
Length	162 km	220 km
Width	71 km	80 km
Slip	2.7 m	3.7 m
$X0$	-77.66°	-77.56°
$Y0$	-12.02°	-12.26°
Upperside depth	8 km	7 km
Strike	330°	330°
Dip	20°	20°
Rake	90°	90°

mechanical and analogic instruments, whose parameters and amplification factors are not very well known, hence their results are not reliable.

The tidal station of Callao, of the Peruvian Navy, was in maintenance when the earthquake ocurred; hence, we do not have tsunami waveforms for this event. The tidal stations of Matarani to the south and Talara to the north, have not been installed in 1940.

The information of the macroseismic effects and historical reports have been taken from Silgado (1978) and Dorbath et al. (1990). The seismic and hypocentral parameters (Table 3.1) have been taken from Beck and Ruff (1989). The focal mechanism has been taken from Beck and Ruff (1989), however the azimuthal angle (strike=340°) does not fit very well with the strike of the trench axis and has been slightly modified to 330° (to align the fault plane geometry orientation with the trench and coastline orientation), as it is observed in Figure 3.1 and Table 3.2.

The bathymetry data have been taken from the Gebco 30 model (www.gebco.net), which has a resolution of 30 arcsecond or 932 m approximately. This global bathymetry has been combined with finer bathymetry from the Peruvian Navy and finer topography from satellite images (SRTM1: http://www2.jpl.nasa.gov/srtm) in Chimbote, Huarmey, Huacho, Callao and Paracas, where the tsunami waveforms were calculated. All this bathymetry and topography data has been interpolated using the Kriging method to obtain a digital elevation model with a resolution of 10 arcsecond (approximately 309 m).

3.3 Methodology

In this section we present arguments to choose the best fault plane scenario according to macroseismic and historical information. Then, we describe the linear and non linear tsunami

TABLE 3.3: Location of tidal stations used in this research. N represents the number of the tidal station. H is the maximum tsunami height for non linear model and Ta is the tsunami travel time, both for the preferred model (Mw 8.0).

N	Station	Lat (°)	Lon (°)	H (m)	Ta (min)
1	Chimbote	-09.0800	-78.6170	0.87	68
2	Huarmey	-10.0992	-78.1824	0.39	20
3	Huacho	-11.1218	-77.6162	1.80	05
4	Callao	-12.0689	-77.1668	1.17	13
5	Paracas	-13.8061	-76.2919	0.96	46

numerical modeling used to simulate the tsunami waveforms.

Fault plane scenario

To choose the fault plane scenario, we have conducted two numerical simulations of tsunamis. The first scenario corresponds to a seismic event of Mw 8.2 (as proposed by Dorbath et al., 1990 and Kanamori, 1977) and the second one to an event of Mw 8.0 (as suggested by Beck and Ruff, 1989; Beck and Nishenko, 1990).

According to the methodology of Jimenez et al., (2013), we have constrained a homogeneous seismic source from macroseismic information reported in the literature (Silgado, 1978; Dorbath et al., 1990).

For the seismic scenario of magnitude of Mw 8.2, the length of the fault geometry was estimated in 220 km by Dorbath et al. (1990). The width of the fault geometry (80 km) was calculated according to scaling relations for subduction zones (Papazachos et al., 2004). The location of the rupture geometry fits with the isoseismal intensity of VIII according to Dorbath et al. (1990), (Figure 3.1). The depth of the upper side of the fault plane was calculated in 7 km, assuming a focal depth of 20 km. The slip distribution is homogeneous and the slip value was set in 3.7 m, taking into account the definition of the scalar seismic moment.

For the seismic scenario of magnitude of Mw 8.0, the dimensions and slip of the fault geometry have been calculated using the scaling relations of Papazachos et al. (2004). Hence, the length is 162 km, the width is 71 km and slip is 2.7 m. The upperside depth of the fault is set at 8 km. The location of the fault geometry fits the isoseismal intensity of VIII (Figure 3.1).

For both seismic scenarios, the focal mechanism parameters were taken from Beck and Ruff (1989). The azimuthal or strike angle was changed to 330°, similar to the strike angle of the trench axis, to take into account the mean value of this parameter according to Global CMT catalog (www.globalcmt.org) for the Central Peru region (Table 3.2).

Tsunami numerical modeling

To obtain the initial condition for tsunami propagation, we have calculated the coseismic deformation field (vertical, north and east components) using the formulation of Okada (1992) considering an elastic, homogeneous, linear and semi-infinite medium [Oka92]. We take into account that the sea surface deformation is similar to sea bottom deformation and the deformation process is instantaneous.

In this research, we use the linear shallow equations to simulate the tsunami propagation; however, the non-linear effects can not be ignored as the tsunami approached the coasts, because the tidal stations are located at very shallow region. Therefore, we have used also the non linear equations to simulate the propagation and inundation processes near the tidal stations.

The tsunami propagation process has been simulated according to the linear version of TUNAMI-F1 numerical model (Imamura, 1996) [Ima96], using a bathymetry with a resolution interpolated of 10 arcsecond. The tidal stations have been located in coastal cities (most of them correspond to real tidal stations, except the virtual tidal station of Huarmey) to obtain synthetic tsunami waveforms (Table 3.3). The computational grid, to conduct the linear tsunami modeling, has a dimension of 2521×2521 rows and columns, with geographical limits: -08.0° to the north, -15.0° to the south, -82.0° to the west and -75.0° to the east. The resolution have been interpolated to 10 arcsecond (309 m approximately).

The tsunami propagation and inundation processes have been simulated according to the non linear version of TUNAMI-N2 numerical model (Imamura et al., 2006) [Ima06]. The original Fortran code has been modified in order to take into account the format of the input and output data files. We have used two nested grids in the computational domain. The greater one has a dimension of 841×841 rows and columns, with a resolution of 30 arcsecond. The smaller grid has a dimension of 1225×1873 rows and columns, with a resolution of 10 arcsecond. The geographical limits are similar as the linear computational grid.

To obtain the maximum tsunami height in the whole Pacific Ocean, we have conducted a linear tsunami simulation with only one computational grid of dimensions 2461×2056 rows and columns, with a resolution of 240 arcsecond (4 arc-minute). The geographical limits are: 61.0° to the north, -76.0° to the south, 128.0° to the west and 292.0° to the east.
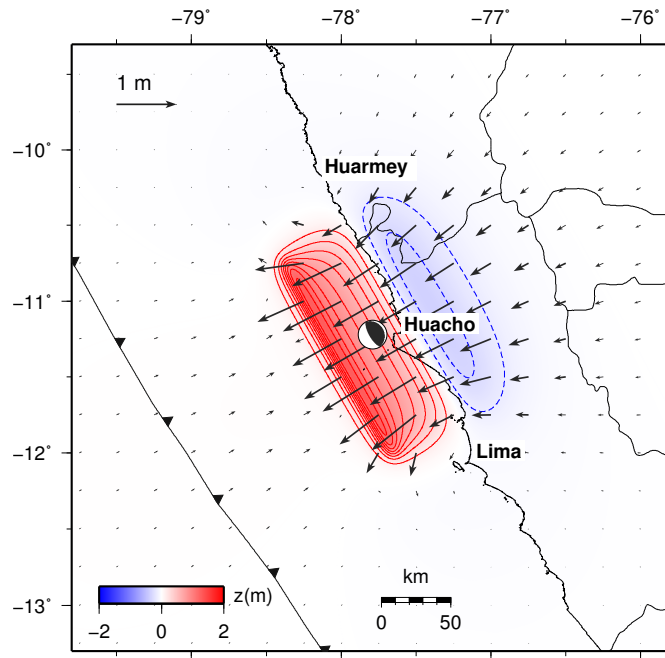
FIGURE 3.3: Deformation field for the preferred model (Mw8.0). The red zone represents the uplifted region and the blue represents the subsidence. The focal diagram is located on the epicenter. The curve lines represents 15 cm. The arrows represent the horizontal displacements.

3.4   Results and discussion

In this section, we present and discuss the main results obtained in this research: seismic source geometry, crustal deformation, tsunami waveforms, tectonic implications and assessment of seismic and tsunami hazard for the Central region of Peru. Because the tsunami generated by the seismic scenario of Mw 8.2 produced maximum tsunami heights between 2.3 to 2.5 m in Huacho and Callao respectively, and because there are not any reports about great damage in these ports, we have chosen the seismic scenario of Mw 8.0 as the preferred model.

Seismic source

The parameters and dimensions of the preferred seismic source geometry, mean slip, location of the fault plane and focal mechanism or fault plane orientation angles have been listed in Table 3.2. The seismic moment and magnitude equivalent was estimated in Mw 8.0.

The location of the seismic source geometry, near the coast and with a small fragment inland (Figure 3.1), indicates that the rupture was generated in the downdip of the megathrust. Hence, there is still a portion of the megathrust updip (near the trench) that has not been broken by the 1940 event nor the 1966 (Mw 8.1) event, with a high tsunamigenic potential
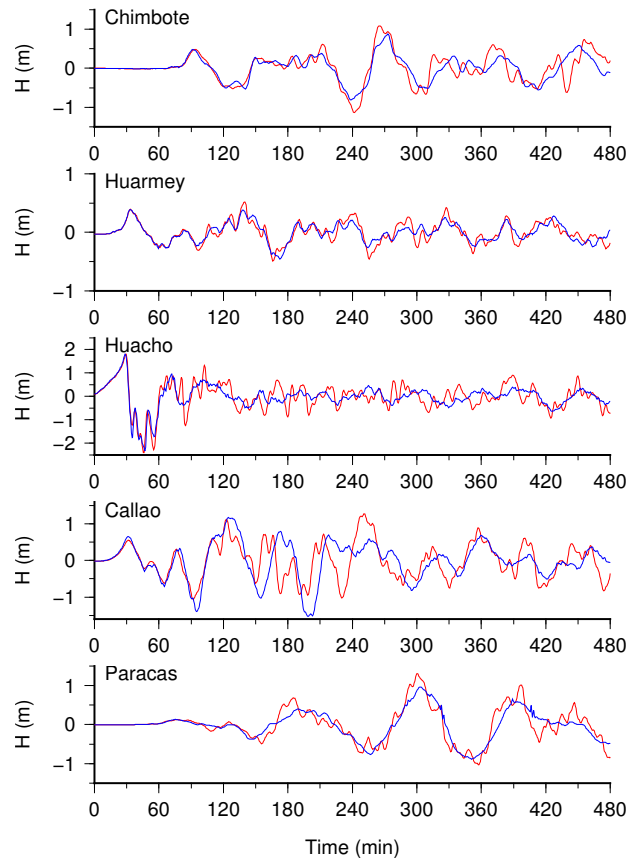
FIGURE 3.4: The synthetic tsunami waveforms recorded on the virtual tidal stations from the preferred model (Mw 8.0). The blue signals represent the non linear model and the red ones represent the linear model. For the first period, the linear and non-linear waveforms agree very well.

after several decades, according to the interseismic coupling model of Peru (Villegas et al., 2016) [Vil16].

Coseismic deformation field

Based on the location and parameters of the seismic source geometry, the vertical coseismic deformation field indicates that some locations in the coastline have suffered uplift rather than subsidence. For example, the city of Huacho has uplifted around 11 cm. Furthermore, the maximum uplift was 1.27 m and the maximum subsidence was 0.36 m, in the seismic source region.

We have calculated the horizontal vectors of coseismic displacements (north and east components), due to the 1940 earthquake, in the locations of selected points as shown in Figure 3.3. The maximum horizontal displacements exceeded 1 m. It is noticed that the displacement vectors point to the sea, in the opposite direction to the interseismic velocity vectors (in Central region of Peru the interseismic velocity has a magnitude of 2 cm/year approximately), which point to the continent. Hence, the elastic rebound theory is verified.
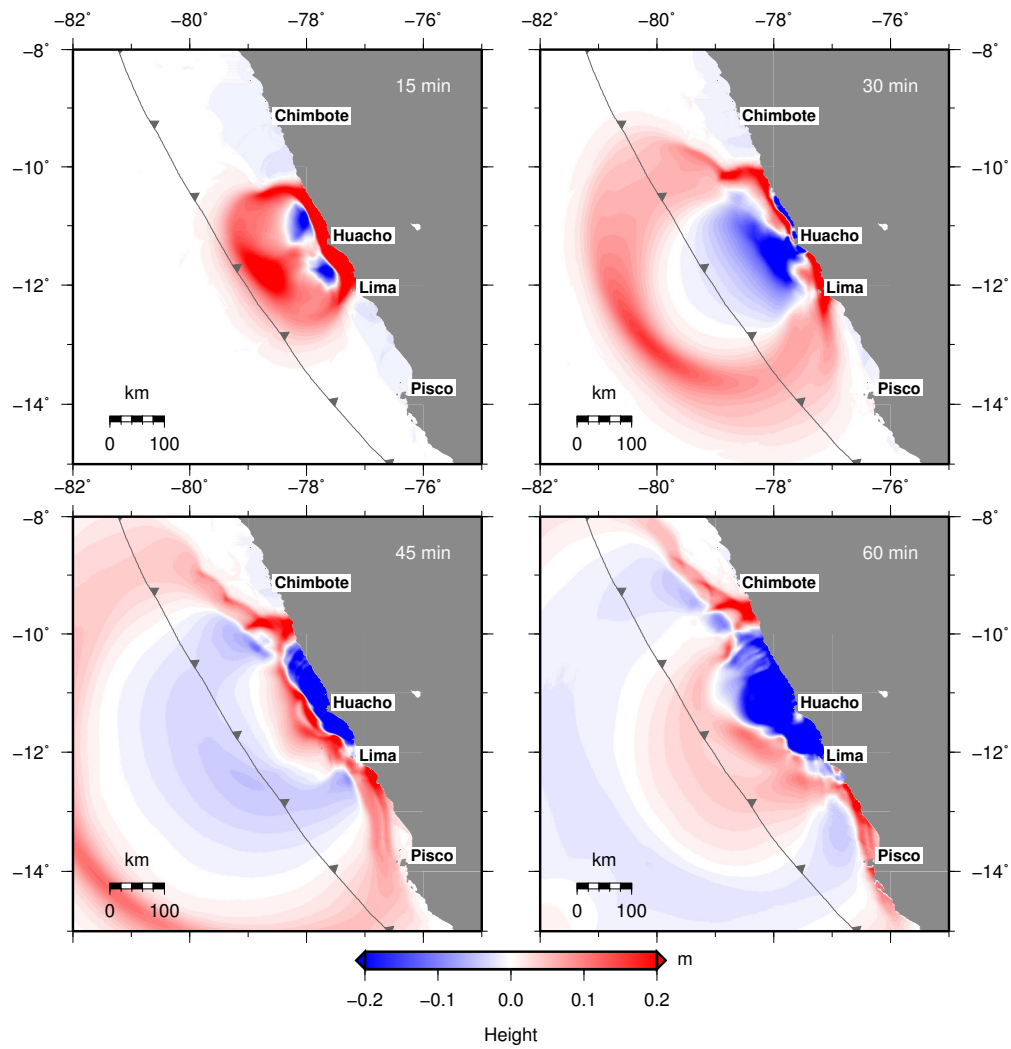
FIGURE 3.5: Propagation of the 1940 tsunami for $t = 15$, 30, 45 and 60 min. The red color represents the maximum values of wave height (m), while the blue color represents the minimum values. The barbed line represents the Peruvian trench.

TABLE 3.4: Correlation coefficients between the simulated signal from the linear model vs. the non linear model, for the preferred seismic source (Mw 8.0).

N	Station	Time window (min)	Correlation
1	Chimbote	0-130	0.98
2	Huarmey	0-090	0.99
3	Huacho	0-055	0.98
4	Callao	0-089	0.96
5	Paracas	0-106	0.92

Tsunami simulation

The synthetic tsunami waveforms were calculated in the locations of the tidal stations of Chimbote, Huarmey, Huacho, Callao and Paracas for two tsunami modeling: the linear and non linear models (Figure 3.4).

From these synthetic waveforms, we can obtain some important parameters of the tsunami: arrival times and maximum heigths. The maximum tsunami height was 1.80 m for Huacho and for Callao was 1.17 m. The tsunami travel time for Chimbote is 68 min, for Huacho it is almost inmediately with less than 5 min and for Callao is 13 min (Table 3.3).

We can noticed that the tsunami waveforms for the first period of linear and non linear models have a very good correlation (Table 3.4). This fact allows the use of linear equations in tsunami waveform inversion, where only the first waveform period is used. Another observation is that the maximum height of the linear waveform is slightly greater than the non linear waveform; furhtermore, the linear waveform is contaminated by short period noise due to reflections on the coast.

We do not have real information reported about observations of the tsunami heights and runups. According to Silgado (1978), we know that there was no significant damage due to the tsunami. However, with the results of the numerical modeling of the event scenario of magnitude Mw 8.0, we have an approximated idea of these parameters.

Figure 3.5 shows the propagation of the 1940 tsunami waves, for four snapshots: 15, 30, 45 and 60 min. The directivity of the propagation waves is towards the west, perpendicular to the fault plain direction. Figure 3.6 shows the maximum tsunami height on Pacific Ocean, the tsunami directivity points to central Pacific island, New Zealand and to Antarctica.

Tectonic implications

The 1940 Peruvian earthquake is a very important seismic event, due to it initiated the seismic sequence of the 20th and 21st century in the Central Peru region after a quiescent period of around 200 years from the 1746 megathrust earthquake.

From the results of Beck and Ruff (1989) for the seismic rupture duration (24-30 s), we assume that the seismic rupture is simple with only one asperity around the epicenter.

The map of interseismic coupling calculated by Villegas et al. (2016) shows significant asperity in the Central region of Peru. After the ocurrence of the 1940 earthquake (near the coastline) and the 1966 earthquake (between the coast and the trench), we suggest that there is a high potential of generation of tsunamis by shallow earthquakes near the trench.
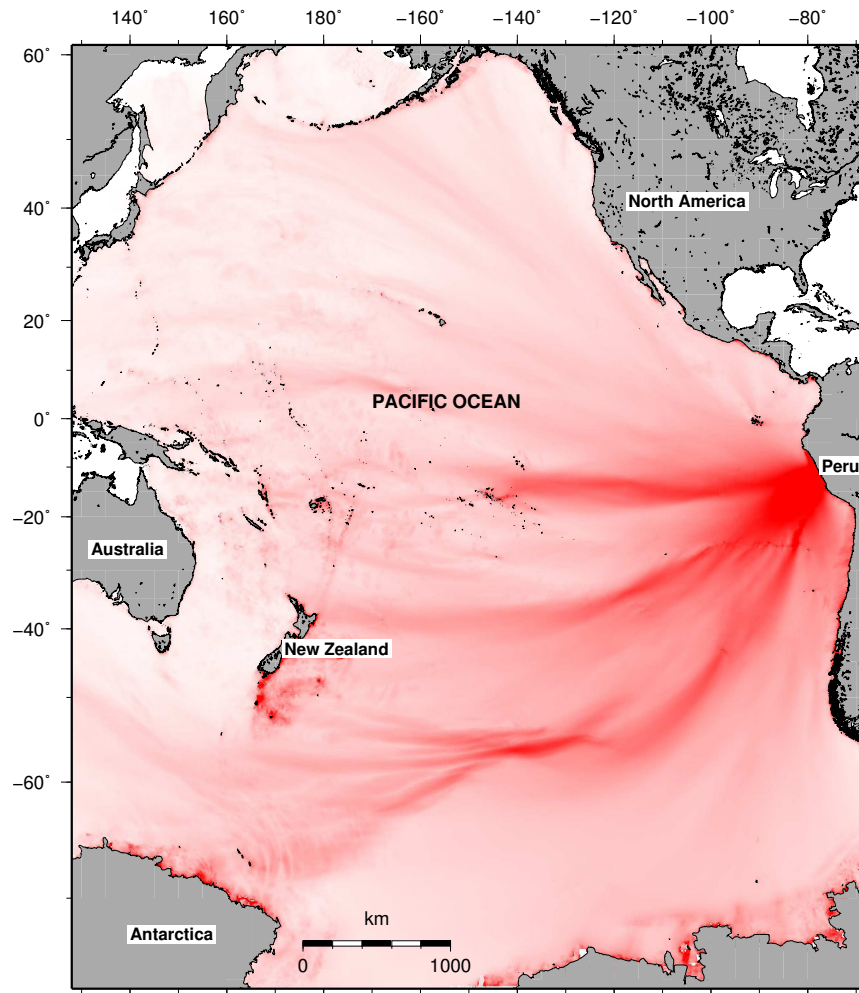
FIGURE 3.6: Maximum tsunami height (in colour red) of the 1940 tsunami propagation on Pacific Ocean. Tsunami directivity points mainly to central Pacific islands, New Zealand and continent of Antartica.

The sequence of 20th and 21st century earthquakes: 1940 (Mw 8.0), 1966 (Mw 8.1), 1974 (Mw 8.1) and 2007 (Mw 8.1), has not released all the seismic moment accumulated after the ocurrence of the great 1746 Callao earthquake and tsunami ($\sim$Mw 9), rather only around 20%.

3.5   Conclusions

The results obtained in this research are a first approximation based on macroseismic information and some data deduced by the researchers. However, at least, we have an idea of the impact of the 1940 seismic event and tsunami (according to our preferred model: Mw 8.0) through the numerical tsunami modeling.

We have modeled a homogeneous seismic source of magnitude Mw 8.0 (corresponding to the preferred model) with dimensions 162$\times$71 km^2, with a mean slip of 2.7 m. Due to the lack

of geophysical data, it is difficult to obtain a heterogeneous slip distribution and therefore to identify the main asperity.

We have obtained the vertical coseismic deformation field with uplift offshore and in the coastline (for example, the city of Huacho was uplifted around 11 cm) and subsidence inland. The maximum uplift was calculated in 1.27 m and the maximum subsidence was 0.36 m.

The first period of tsunami waveforms from linear and non linear models fits with a very good correlation. This fact allows the use of linear equations in tsunami waveform inversion, where only the first period is used. The maximum height of the linear waveform is slightly greater than the non linear waveform; furhtermore, the linear waveform is contaminated by short period noise due to reflections on the coast.

The maximum simulated tsunami height obtained for Huacho was 1.80 m and for Callao was 1.17 m, compatible with the historical reports of no significant damages in these ports. The tsunami travel time for Huacho would be immediate. For Callao, it would be 13 min and for Chimbote would be 68 min.

Considering that the seismic sequence of earthquakes ($\sim$Mw 8) in 20th and 21st centuries has released only around 20% of the seismic moment accumulated from the megathrust earthquake of 1746 ($\sim$Mw 9), and considering the interseismic coupling distribution for the Central Peru region, we suggest that there is a high potential for the generation of a shallow tsunamigenic earthquake offshore Huacho and near the trench.

Chapter 4

Estimation of the seismic source of 1966 Huacho-Peru earthquake (Mw 8.1)

In this chapter we have estimated the distribution of the seismic source of the Huacho earthquake that occurred on October 17 1966 (21:41 UTC) using tsunami data. This event took place offshore the Central Peru region and produced severe ground shaking in the cities of Supe and Huacho with intensities in the Mercalli modified scale of VIII, which lead to 100 fatalities. As a coseismic effect the earthquake produced a regional tsunami that inundated some coastal with major effects in Casma and Tortugas. Here we used the tsunami tide gauge records of three stations located in Chimbote, Callao and Marcona, in order to obtain the seismic source parameters from an inversion process, in which we compare the simulated and observed signals using the non-negative least square approach. Our results show a dislocation with a maximum slip of 6.9 m located in the southern part of the rupture area, which implies that the asperity or area with maximum energy release was located offshore the Supe city. These results are consistent with the maximum intensities reported in this area. Finally, our model indicates a tsunamigenic scalar moment of $2.07{\times}10^{21}$ Nm, which is equivalent to a moment magnitude of Mw 8.1.

4.1 Introduction

The tsunami waveforms contain information about the physical processes of generation in the seismic source and propagation of the tsunami (which depends on bathymetry, a known parameter). Taking into account the response of the instrument (former mechanical and

analog gauge of before 1966) it is possible to perfom the inversion of the tsunami waveforms to get the distribution of asperities (areas of greatest seismic energy release) or seismic source distribution.

"One way to verify a tsunami source model or coseismic deformation model is by simulating the corresponding tsunami wave". "Parameters such as arrival time, amplitude, period and polarity of the first wave and, in general, the shape of the simulated tsunami wave should have a good correlation with the corresponding digitally processed tsunami waveforms for the available stations" [Sat91].

From a physical point of view, the method of inversion of tsunami waveforms gives a better result in comparison to the method of inversion of teleseismic waves, to obtain the parameters of the tsunami source, because the model of velocity of the tsunami wave is a parameter that is known relatively well, since the speed of tsunami waves only depends on the bathymetry [Sat91]. On the other hand, in the inversion of the teleseismic waves, the velocity model of the seismic waves is not known with accuracy, due to the physical properties of the local heterogeneities of the earth's crust. "The goodness of the results obtained depends on the quality of the tsunami recordings, on the good azimuthal coverage of the stations and on the quality and resolution of the bathymetry data around the stations" [Jim14].

The tsunami waveform inversion method is not new, several works address historical tsunamis as well as past tsunami events using tsunami waveform inversion (Heidarzadeh and Satake, 2015 [Hei01]; Fujii and Satake, 2006 [Fuj06]).

Jimenez et al. (2016) [Jim16], have studied this event using a bathymetry with resolution of 30 arc min and fault plane with a constant dip angle. In this research we refine the results of Jimenez et al. (2016), considering a finer bathymetry in the ports, the fault plane was divided into 20 subfaults to obtain results in more detail.

We estimated the earthquake source distribution of the Huacho 1966 earthquake through the inversion of three near-field tsunami tide gauge records (Figure 4.1). As evidenced in other studies, to reconstruct a complex rupture process it is necessary at least three tsunami records with stations disposed in a good azimuthal distribution [Anc14]. It is worth to mention that the records we use in this study have not been used before in any technical or scientific report, so here by using this data we aim to contribute to the understanding of the characteristics of the earthquake source of one of the largest earthquakes occurred in the central Peru region in the last 20th century.
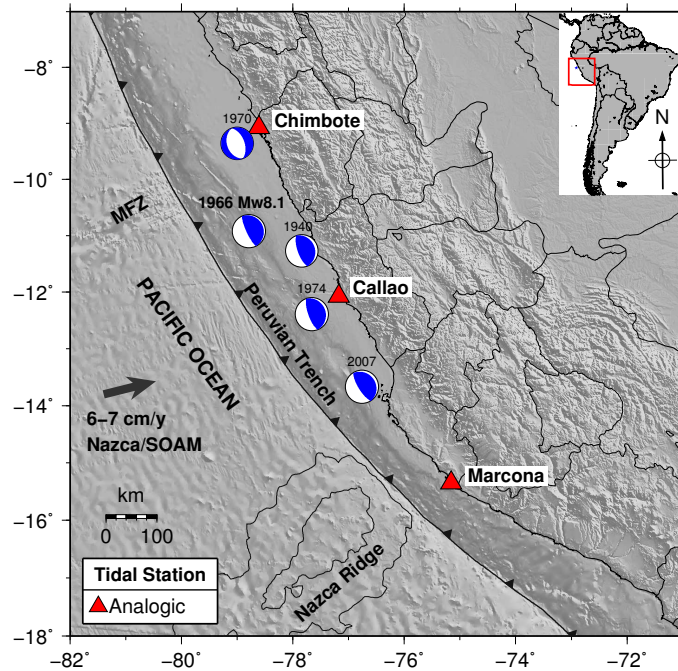
FIGURE 4.1: Seismotectonic setting and topography of the central region of Peru. The distribution of tidal stations (red triangles) is shown. MFZ: Mendaña Fracture Zone. The beach balls represent the seismic sources. The red rectangle within the inset shows the location of the study area.

Seismotectonic setting of Central Peru

The 1966 Huacho earthquake was generated due to the release of the tectonic stresses accumulated in the zone of interaction of the tectonic plates of Nazca and South America. The velocity of convergence of these two plates is 6-7 cm/y [Nor98], [Ken03]. The focal mechanism of this earthquake is of the thrust fault type at the boundary between two tectonic plates, with the Nazca plate moving below the continental plate, in a process called as subduction (Figure 4.1). "The dominant seismic activity along the coast of Peru is a direct consequence of the subduction process of the Nazca plate under the South American plate" (Tavera and Buforn, 2001), so "the coast of Peru has a history of big earthquakes, many of which have generated tsunamis" [Tav01].

During the 20th century and at the beginning of the 21st century, several destructive earthquakes of a magnitude around Mw 8.0 have been generated in central Peru region (between the Nazca ridge and Mendaña fracture zone): 1940 in Lima (Mw 8.0), 1970 in Ancash (Mw 7.9, intraplate earthquake with focal mechanism of normal fault type, occurred inside the Nazca plate), 1974 in Cañete-Lima (Mw 8.1) [Lan95], 1966 in Huacho-Lima (Mw 8.1) [Abe72]) [Bec89] and 2007 in Pisco-Ica (Mw 8.1) [Sla10]. Almost all of these seismic events have been generated within the area of rupture of the great Callao earthquake of 1746 ($\sim$ Mw 9.0) [Bec90], [Dor90], [Jim13].

The 1966 Huacho earthquake partially filled the seismic gap left by the great earthquake of 1746; however, after more than 50 years, it is feasible to consider this region of rupture as a new *seismic gap*, because the tectonic stresses have not been completely relaxed due to the earthquake of 1966 and also due to the accumulation of new tectonic stresses in the last 50 years. Chlieh et al. (2011) [Chl11] and Villegas et al. (2016) argue that assuming that the current rate of change of the seismic moment deficit is stationary, then the accumulated moment since 1746 indicates that the occurrence of a large similar seismic event would be delayed, even considering that half of the seismic moment deficit was released asesimically there is still enough energy to reproduce an event similar to the 1746 earthquake [Vil16]. "The accumulation of the seismic moment released by the 1940-2007 seismic sequence represents only 23% of the accumulated moment deficit since 1746, suggesting that a significant amount of seismic moment would still be released in this segment" of more than 500 km from the Nazca ridge to the Mendaña fracture zone (Villegas et al., 2016).

As a coseismic effect of the 1966 Huacho event, a tsunami was generated, which according to Silgado's report (1978): about 50 minutes after the earthquake there was a moderate tsunami, with the first wave recorded in the tide gauges of La Punta, Chimbote and San Juan de Marcona. There were inundations in Casma and Tortugas, with several fishing factories suffering heavy losses. The maximum intensity (probably IX MM) occurred in the San Nicolas farm located 3 km south of Supe city (Lomnitz and Cabré, 1968) [Lom68], an intensity of VIII MM was reported in Huacho and VII MM in Lima. There were also reported 100 deaths due to the earthquake, but none due to the tsunami [Sil78].

4.2 Methodology: acquisition and processing of tsunami data

In general, the tsunami recording is an important source of useful information to obtain the seismic source parameters and validating the numerical modeling of tsunamis. The waveforms recorded in buoys on the high seas (such as the Deep-ocean Assessment and Reporting of Tsunamis: DART) and the first waveform period for coastal stations provide information on the characteristics of the tsunami source, such as the geometry and extent of the rupture area, the slip distribution, among others. One fundamental difference between deep ocean tsunami records and tide gauges is: tide gauges can be greatly affected by the non-linear interaction of the tsunami wave with the shallow bathymetry and the harbor configuration; meanwhile, deep ocean tsunami records are not affected by non-linear processes.

In order to carry out the present investigation, the tsunami waveforms recorded in analogical format, a pencil mark on a sheet in a rotating cylinder, in a mechanical station composed by a system of pulleys and a floating buoy to measure the sea level were used. The time control was performed with a mechanical clock, which was calibrated periodically, this implied

some uncertainty in the control of time. These tsunami recordings were obtained from the "Direccion de Hidrografia y Navegacion" (DHN) of the Peruvian Navy; also, from the publication of Murty and Wigen (1975) [Mur75], which were then scanned and digitized, and correspond to three mechanical tidal stations belonging to the Peruvian Tidal Network located in the ports of Chimbote, Callao and San Juan de Marcona (Figure 4.1, Table 4.1).

In order to have a good azimuthal geometrical distribution of the stations with respect to the tsunami source, there should be more stations to the north and at least one buoy located offshore, which did not happen in this particular event due to the lack of more stations and recordings of good quality and noise free. Talara station (in the north, Lat = -04.57°) recorded a maximum amplitude of 5 cm and Matarani station (in the south, Lat = -17.00°) recorded a maximum amplitude of 35 cm, however, the signal to noise ratio was very close to unity, so the noisy Matarani recording was not used in the inversion process.

After a tsunamigenic earthquake, the tidal station would record the event and the corresponding waveform, in the frequency domain, would consist of a broadband spectrum, with three main components: tides (long period, in the order of hours), swell (short period, in the order of the seconds) and the tsunami waves (of intermediate period, in the order of the minutes). To study the tsunami recordings, the digital signal processing algorithms must be applied.

In the case of analogical recordings, these were scanned and digitized. The choice of the sampling rate will depend on the quality and resolution of the scanned image and the computational algorithm used to digitize it. Once the digitized time series is obtained, the data are interpolated for a sampling rate of one minute, using a cubic polynomial interpolation method, with the purpose of homogenizing the sampling rate. Then, the average value of the signal was removed to center it with respect to the abscissa axis. Also, an 80-term polynomial interpolation filter was applied to remove the very long period components (tides) and a low pass filter consisting of the moving average of 3 consecutive samples of the signal to remove the short periods (waves). Finally, we don't take into account the absolute time, but a relative time and this is referenced with respect to the origin time of the seismic event.

It should be noted that this was the second tsunami recorded by Peruvian tidal stations after the 1964 Alaska tsunami. At great distances, the 1966 Peruvian tsunami was recorded at stations off the coast of California with amplitudes smaller than 10 cm.

"For computational effects of the inversion method, all the recordings were synchronized in such a way that the arrival time of the first wave matchs to the 51th minute, a value similar or close to the shortest arrival time that corresponds to the station of Callao" [Jim14] (Table 4.1). It is observed that the arrival time for the station of Marcona is slightly smaller than that of the station of Chimbote, this is due to the effect of the bathymetry of the Peruvian

TABLE 4.1: The tide gauge stations used in the inversion process. The arrival time (TA) is measured with respect to the earthquake origin time. N represents the number of the tidal station.

N	Station	Lon (°)	Lat (°)	TA (min)
1	Chimbote	-78.6127	-09.0763	66
2	Callao	-77.1740	-12.0710	51
3	Marcona	-75.1580	-15.3467	64

trench and to the phenomenon of refraction that controls the directivity of the propagation of the tsunami waves, as explained by Lomnitz and Cabré, 1968 [Lom68].

"Because the velocity and directivity of the tsunami waves depend on the bathymetry or marine topography, it is essential to have a good bathymetric model for the calculation of the Green functions or elemental mareograms" [Jim14]. The global bathymetry has been taken from the model GEBCO 30 (avalaible on http://www.gebco.net), with a resolution of 30 arc sec or approximately ∼ 927 m.

The bathymetry is relatively shallow in the north of Peru near Chimbote (Figure 4.1). "The velocity of the tsunami waves is proportional to the square root of the bathymetry", so that the arrival time of the first tsunami wave to the station of Chimbote does not keep a proportionality with respect to the location of the epicenter. The bathymetry is also shallow for Callao; both Callao and Chimbote seem to be affected by this shallow submarine shelf, so linearity between source-station distance and arrival time is difficult to evaluate.

Hypocentral parameters, focal mechanism and aftershocks

Hypocentral parameters were calculated and reported by several researchers, which are summarized in Table 4.2. Dewey and Spence (1979) conducted a recalculation of the hypocentral parameters using the Joint Hypocenter Determination (JHD) method [Dew79], these parameters were: Latitude = -10.92°, Longitude = -78.79°, and Depth = 21 km (Table 4.2). Abe (1972) calculated a scalar seismic moment of 2.0×10^{21} Nm and the orientation of the fault plane or focal mechanism from the inversion of teleseismic waves, these parameters being: strike = 335°, dip = 12°, and rake or dislocation angle = 90°, (Table 4.2). Kanamori (1977) reported a magnitude of Mw 8.1 [Kan77]. Therefore, the 1966 earthquake represents an event of reverse fault type with a small dip angle on the megathrust, whose rake angle is almost perpendicular to the axis of the marine trench [Abe72].

Kelleher (1972) recalculated the epicentral location of the aftershocks. A total of 22 depth shallow aftershocks (less than 60 km) of magnitude greater than Mw 4.0 have been counted since the occurrence of the main shock (Oct 17, 1966) until December 9 of the same year.

TABLE 4.2: Hypocentral parameters were reported by Dewey and Spence (1979). The magnitude was reported by Kanamori (1977), the focal mechanism was calculated by Abe (1972) and the duration of the source rupture process was calculated by Beck and Ruff, (1989).

Date	Oct 17, 1966
Origin time	21:41:51 UTC
Latitude	-10.92°
Longitude	-78.79°
Depth	21 km
Magnitude	Mw 8.1
Strike	$\theta = 335°$
Dip	$\delta = 12°$
Rake	$\lambda = 90°$
Source duration	45 s

Also, Kelleher reported the occurrence of 2 intermediate depth aftershocks, which have not been plotted in Figure 4.2 [Kel72].

Past and recent observations of earthquakes of great magnitude in the world show that the aftershocks occur around the rupture area (Henry and Das, 2001) [Hen01]. It is assumed that the distribution of aftershocks occurring in the first hours fit the rupture area (Lay and Wallace, 1995) [Lay95]. The criterion of taking the distribution of the aftershocks (occurring over several months) as a rupture area might overestimate the results. However, no further information is available on the aftershocks on the first day, for the Peruvian earthquake of October 17, 1966.

The aftershocks of shallow depth are mainly distributed between the marine trench and the coastline, along the rupture geometry, approximately from the zone of Huacho to Casma, covering a surface with an effective area of around 200 km length by 120 km wide (Figure 4.2). On the other hand, Pararas-Carayannis (1974) applied the inverse refraction method to estimate the area of the tsunami source, which covered approximately from Huacho to Caleta Culebras (around 150 km) [Par74]. Besides, Dorbath et al. (1990) assigned an underestimated length of 120 km to the rupture geometry, then used this value to obtain an equation of magnitude scaling with the dimension of the rupture area [Dor90]. However, the distribution of relocated aftershocks from Dewey and Spence (1979) (Figure 4.2) implies a larger size of the rupture area.

4.3   Inversion method

If the parameters or governing equations that characterize a system, the initial and boundary conditions are known, then the behavior of that system can be predicted at any instant of
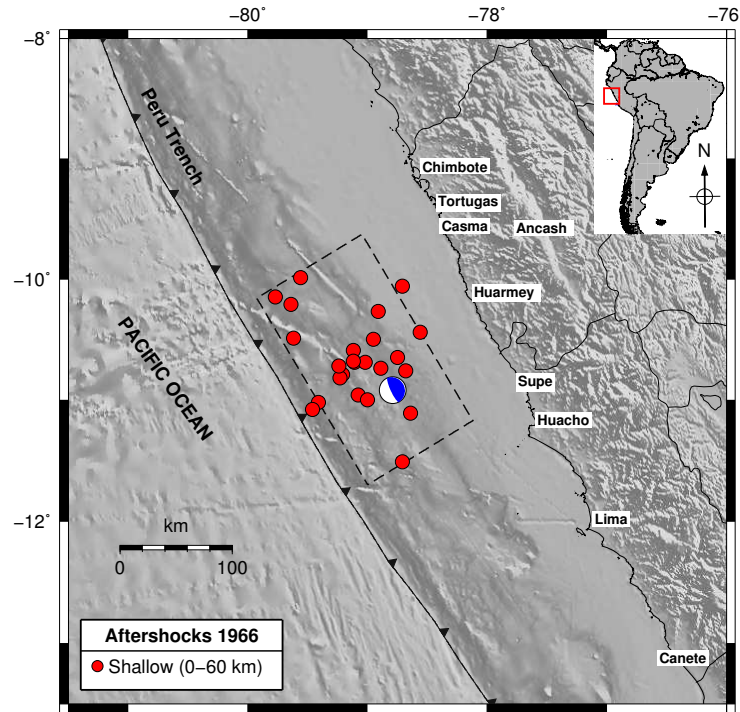
FIGURE 4.2: The red circles represent the aftershocks of the earthquake recalculated by Kelleher (1972). The geometry of the rupture area is observed. The focal diagram represents the seismic source. The rectangle of dashed lines represents the rupture geometry.

time. This type of problem is called the forward problem. On the contrary, "the inverse problem consists in using the results of certain observations to infer the values of the parameters that characterize the system" [Tar05]. In this research, the tsunami waveforms have been used to deduce the parameters of the tsunami source or slip distribution.

The calculation of the tsunami source distribution represents a typical inverse problem. "The process is considered as a linear and time-invariant system that has two important properties" [Opp97]:

a) Linearity, is a "property that allows to use the superposition principle for the Green functions and for the unitary deformations".

b) Time invariance, a system is time-invariant if a time shift in the input signal causes a time shift in the output signal. "This property allows a time shift of the observed signals and their corresponding Green functions, synchronizing the observed signals so that the arrival time of the tsunami corresponds to the minimum arrival time" (from Callao station: 51st minute), only for purposes of an efficient computation [Jim14]. So, we are not using an absolute time, but a relative time in the computational inversion process.

This last point allows the utilization of recordings from tide stations regardless of the epicentral distance. "The solution of the inverse problem is not unique, but is chosen from the set of values that provide the best correlation between observed and simulated data" [Jim14].

To calculate the slip distribution, we have used the inversion method for three available tsunami waveforms of acceptable quality.

To obtain greater detail of the tsunami source, the rupture geometry must be divided into several subfaults. According to the approximation of the linear shallow water theory, the relationship between the bathymetric depth H and the wavelength $\lambda \approx L$ must be less than $1/20$ to obtain an error smaller than 1% (Satake, 1987) [Sat87]. Considering an average bathymetric depth in the source region of $H = 1.5$ km, then the size of the subfault L should be greater than 30 km, to keep the linearity of the process.

We have conducted two inversion scenarios: the first one with 12 subfaults of dimensions 50×40 km^2 and the second one with 20 subfaults of dimensions 40×30 km^2. The second scenario is our preferred siesmic source model. In this case, the rupture area was divided into 20 subfaults or fragments of similar dimensions: $L = 40$ km and $W = 30$ km, at a depth H_j with respect to the upper side (according to the vertical coordinate) of each subfault. The relationship between the different geometric parameters of the source is explained by Jimenez et al., (2014) [Jim14].

The "coseismic deformation was calculated for each subfault with a unit slip", using the formulation of Wang et al. (2003) [Wan03] for an elastic medium, stratified by velocity layers (Table 4.3) and the focal mechanism data. The fault plane orientation parameters (azimuth, dip and rake angle) are taken from the research of Abe (1972) [Abe72] and are similar for each subfault (Table 4.2).

Green functions for the 1966 Peruvian tsunami

"The Green function (from a physical point of view), represents the system response, for example, a simulated waveform in the i-th station, when the system is perturbed by a unitary pulse, a deformation due to an unit slip in the j-th subfault" [Jim14]. As an initial condition, this deformation field is used to calculate the Green functions or elementary waveforms at each station by simulating the tsunami wave propagation by the finite difference method for each subfault, using a real bathymetry. At each station, we can express the observed tsunami waveforms as a linear combination of the calculated tsunami waveforms, such as:

$$G_{ij}(t)m_j = d_i(t) \tag{4.1}$$

Where "$G_{ij}(t)$ is the Green function calculated in the i-th station generated by the j-th subfault, m_j is the slip or dislocation in the j-th subfault and $d_i(t)$ is the waveform observed in the i-th tide gauge" [Jim14].

We have modified the TUNAMI numerical model for tsunami propagation for a single computational grid [IOC97] to calculate the Green functions corresponding to the tide stations of Chimbote, Callao and Marcona. The original TUNAMI code include a radiation condition as an open boundary condition, the modification takes into account the effect of an absorbing layer to avoid the numerical reflections in the open oceanic boundaries, in a more efficient way. In this propagation grid, a linear model for a regular bathymetric grid in spherical coordinates based on the hydrodynamic shallow water theory was used. The differential equations of continuity and conservation of linear momentum are numerically integrated using the finite difference method under the numerical scheme of "frog leap". A CFL (Courant Friedrichs Lewy) numerical stability condition less than 1.0 was established to avoid numerical instabilities.

"A commonly used method to define the initial condition for the tsunami propagation is to apply the same vertical deformation of the seabed to the ocean surface. This makes the initial surface displacement of the sea a function of the parameters of the tsunami source" [Gic08]: dimensions of the fault (length and width), focal mechanism (strike, dip and rake angles), location of one corner (latitude, longitude and depth) and slip or dislocation value. "The question is: would the tsunami waveform be sensitive to variation in source parameters? Determining the parameters that could affect the tsunami waveform would show the sensitivity of the time series to the details of the tsunami source" [Gic08]. This is done by a sensitivity test, by which certain parameters are varied and the waveform of the tsunami wave is compared [Gic07]. For example, the Satake (1987) sensitivity analysis shows that the size of the computational cell should be less than one-eighth the size of the fault, to avoid problems of numerical dispersion. Also the frequency spectrum of the waveforms depends on the size of the source: if the source is large, then the spectrum will contain low frequency components; if the source is small (keeping the linearity), it will contain high frequency components [Sat87].

In this case, the initial conditions are based on the deformation method of Wang et al. (2003), they have developed a method to solve for deformation due to a dislocation embedded in a 1D layered elastic half space [Wan03]. Coastal boundary conditions for the linear model (propagation grid) assume a vertical wall. The boundary conditions at the oceanic boundaries are open, to avoid numerical reflections at the edges an absorbing-like condition is added to absorb the energy of the wave. The TUNAMI numerical model for tsunami propagation does not take into account the effects of dispersion, which in this case are not appreciable, because the 1966 earthquake is a near field event. Non linear effects often refers to the advection term and not (frequency) dispersion and these non linear effects are important when modeling wave interaction near the coast (Satake, 1995) [Sat95].

TABLE 4.3: Velocity structure of seismic waves nearby the rupture geometry (central Peru). The thickness of the lithospheric layer is represented by t (Villegas et al., 2009).

N	v_p (km/s)	v_s (km/s)	ρ (g/cm^3)	t (km)
1	5.90	3.47	2.60	02
2	6.10	3.59	2.60	03
3	6.40	3.76	2.90	10
4	6.60	3.88	3.38	15
5	6.80	4.00	3.38	20
6	8.10	4.76	3.38	∞

4.4 Results and discussion

Checkerboard test

A reliability test or checkerboard test was carried out, in which a distribution of synthetic tsunami source of magnitude Mw 8.2 was simulated. The tsunami waveforms were simulated at the 3 stations of Chimbote, Callao and Marcona, then random noise was added at 5 percent of the maximum waveform amplitude. Finally, the synthetic data inversion process was conducted (with a time window from 50 to 90 minutes) and the original distribution was reproduced with a good approximation, except for the subfault in the southern side near the trench, as seen in Figure 4.3.

From the application of the checkerboard test, we conclude that it is possible to reconstruct a complex rupture process with only 3 tsunami recordings, provided that the azimuthal distribution of the tidal stations is adequate, as in the present case with one station to the north of the seismic source and two stations to the south (Figure 4.1).

Inversion process for 1966 Peruvian tsunami

The inversion process was conducted using the non-negative least squares method [Law74]. This method consists of comparing the simulated signal with the observed signal and minimizing the residual square:

$$|G_{ij}m_j - d_i|^2 \rightarrow 0 \tag{4.2}$$

With the condition $m_j > 0$. Additionally, an ad hoc condition has been imposed for 20th subfault (closest to Chimbote, Figure 4.4): $m_{20} = 0$ (a slip null), for a better control of the arrival time to that station. "Only the part of the waveform corresponding to the first period of the wave should be considered to avoid problems of signal contamination with reflection effects and local resonances, due to the bathymetry and morphology of the coast around each
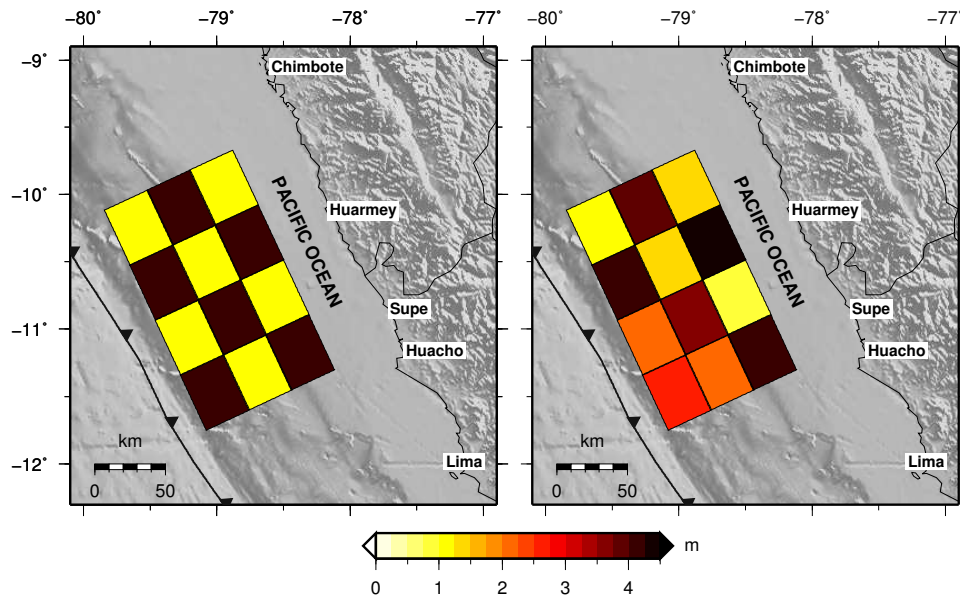
FIGURE 4.3: Test of reliability of the model: a) Distribution of the synthetic source in the form of chessboard. b) Result of the inversion process.

station" (Fujii and Satake, 2008). In this case, the time interval was taken from the onset of the leading wave until one period approximately, according to the vertical lines of Figure 4.5, for purposes of calculating the inversion [Fuj08]. With the additional condition that the difference between a simulated and observed data is less than 0.1 m, we have obtained a number of data of 96 for 20 unknowns (number of subfaults), thereby constraining the non-linear part of the time window.

"The inversion algorithm guarantees that all the values of the slip or dislocation are positive, as a necessary condition from the physical point of view. However, mathematically this model will not provide the most optimal result with respect to the simple least squares method" [Jim14]. The result of the inversion is shown in the Table 4.4. Errors are estimated using the methodology known as "delete half jack knife", by Tichelaar and Ruff (1989) [Tic89].

General results

As we have obtained the slip distribution, the total deformation field is calculated as a linear superposition of the unit deformations, which is used as the initial condition for the propagation of the tsunami waves. The maximum dislocation (slip) is 6.9 m, located in the southern side of the rupture geometry, near the epicenter (Figure 4.4). This explains the fact that the cities of Supe and Huacho were the ones that suffered the greatest impact due to the earthquake, since they are located in front of the maximum asperities. The maximum vertical coseismic deformation (uplift) was calculated at 2.2 m.

TABLE 4.4: The slip distribution or tsunami source distribution is composed of 20 subfaults. The coordinates fit with the lower left corner and the depth fits with the upper side (along the vertical axis) of the correspondent subfault.

N	Lon (°)	Lat (°)	*Slip* (m)	σ (m)	H_j (m)
1	-79.0800	-11.7500	0.00	0.63	6500
2	-78.8360	-11.6379	3.96	1.35	12737
3	-78.5919	-11.5257	1.90	1.83	18975
4	-78.3479	-11.4136	2.28	1.38	25212
5	-79.2351	-11.4222	4.01	1.57	6500
6	-78.9911	-11.3101	6.91	2.67	12737
7	-78.7471	-11.1980	1.97	2.57	18975
8	-78.5030	-11.0859	4.87	2.74	25212
9	-79.3902	-11.0945	5.84	2.30	6500
10	-79.1462	-10.9823	4.28	1.21	12737
11	-78.9022	-10.8702	0.68	0.90	18975
12	-78.6581	-10.7581	4.27	1.29	25212
13	-79.5453	-10.7667	2.20	0.85	6500
14	-79.3013	-10.6546	0.16	0.10	12737
15	-79.0573	-10.5424	0.00	0.10	18975
16	-78.8133	-10.4303	0.00	0.44	25212
17	-79.7004	-10.4389	0.60	0.20	6500
18	-79.4564	-10.3268	0.76	0.22	12737
19	-79.2124	-10.2147	0.63	0.72	18975
20	-78.9684	-10.1025	0.00	0.11	25212

Due to the position of the epicenter and the rupture area geometry, it can be inferred that the rupture process has propagated bidirectionally from the epicenter to the north and to a lesser extent to the south. Around the epicenter and in the southern region of the rupture geometry is concentrated the greater slip or asperity (zone of greater seismic energy release) (Figure 4.4). This agrees with the maximum macro-seismic intensities of VIII in Supe and Huacho, reported by Silgado (1978) [Sil78].

According to the research of Beck and Ruff (1989), the main asperity is located around the epicenter and there is another smaller asperity to the south-east, 80 km from the epicenter [Bec89].

According to Lay et al. (2010), joint inversion of seismic and geodetic data essentially averaged the slip patterns of the two solutions [Lay10]. Extrapolating this affirmation and in order to reconcile both results, inversion of teleseismic waves and inversion of tsunami waves, a joint inversion should be conducted with the two data sets. However, in general the pattern would be an averaged result: the greater asperity would be located around the epicenter and another one to the south of the epicenter.
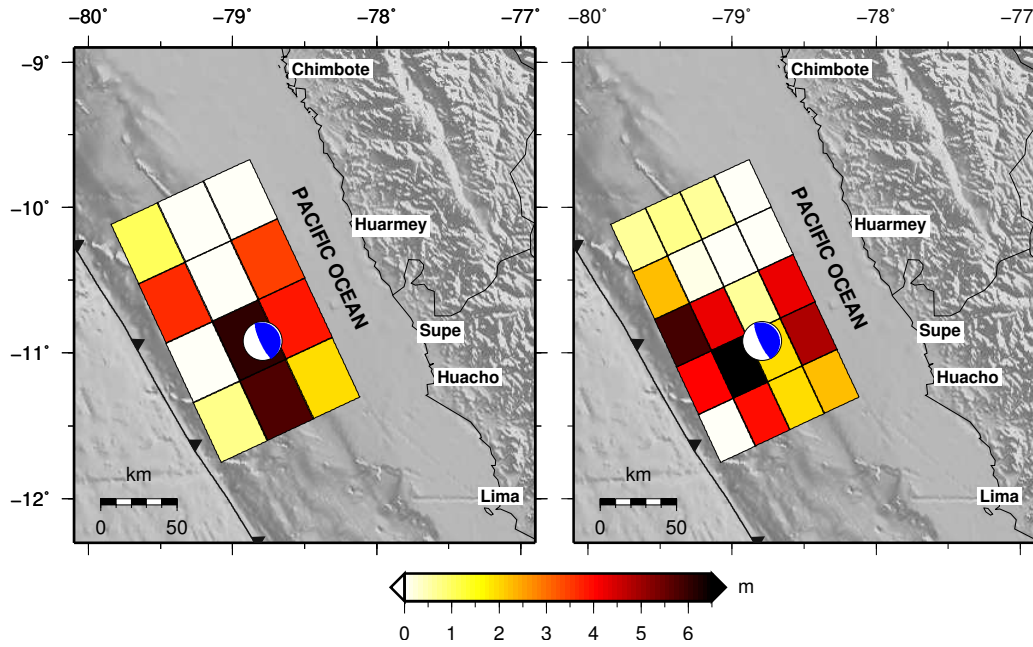
FIGURE 4.4: The distribution of the tsunami source is shown. The focal sphere is located at the position of the epicenter calculated by Dewey and Spence (1979). Note the great asperity, in dark color, in front of the cities of Supe and Huacho. The red triangles represent the tidal gauges. a) Seismic source with 12 subfaults and b) Seismic source with 20 subfaults, our preferred model.

TABLE 4.5: The correlation coefficient between the first period of the observed and simulated waveforms.

N	Station	Correlation coefficient
1	Marcona	0.76
2	Callao	0.89
3	Chimbote	0.97

Comparison of waveforms from tsunami inversion

In Figure 4.5 the results of the inversion can be observed by comparing the observed and simulated waveforms. There is a small delay in the simulated signal at the stations of Chimbote and Marcona, due to the bathimetry around these stations. Also, there is a small discrepancy in the observed and simulated amplitude of the signal at the station of Callao, due to the bathimetry around Callao. However, in general, there is a good agreement between the observed and calculated waveform for the first period. However, the lack of coverage of more tidal stations in the western South Pacific did not allow better constrain to obtain the results. Talara and Matarani stations have been overlooked because the signal to noise ratio is small.

In the Table 4.5, the correlation coefficients between the simulated and observed waveforms
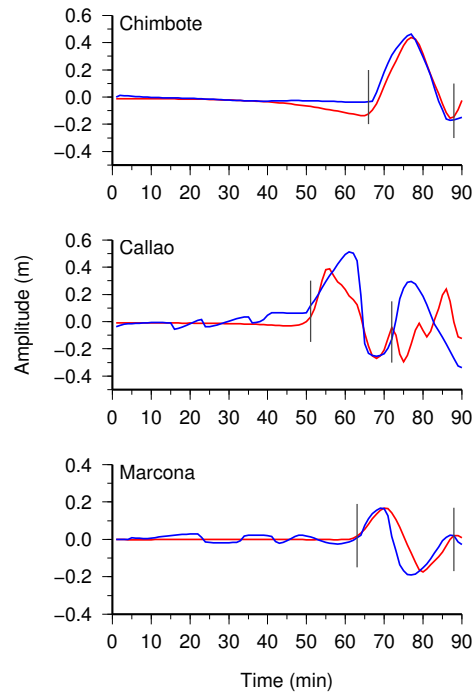
FIGURE 4.5: Comparison between the simulated and observed tsunami waveforms. In blue color the observed waveforms are shown and in red color the simulated signal. The vertical lines indicate the time frame used in the inversion process.

for each station are shown. The Chimbote station presents the highest value of the correlation coefficient (0.97). The Callao station has a correlation of 0.89 for the first period, from the 73th minute prevail phenomena such as reflections, local resonances of short period and diffraction (Figure 4.5). This last phenomena is due to the wavelength of the tsunami is comparable to the size of San Lorenzo island. The normalized error or variance of the inversion process was 0.03.

Tsunami propagation

To conduct the simulation of the tsunami propagation process, a modified version of the numerical model TUNAMI [IOC97] was used. This model integrates the equations of the linear shallow water theory by the method of finite differences. The initial condition is given by the coseismic deformation field (Figure 4.6).

Let us consider the directivity of tsunami waves, the greatest amount of energy was directed in the western direction, towards the region of the Tonga-Kermadec islands. "The directivity effect is determined by the direction perpendicular to the strike of the fault plane and by the Pacific Ocean bathymetry" [Jim14]. To avoid "numerical reflection" at the open ocean boundaries, an absorbing sponge layer of 100 grids wide was used, with an exponential attenuation coefficient.
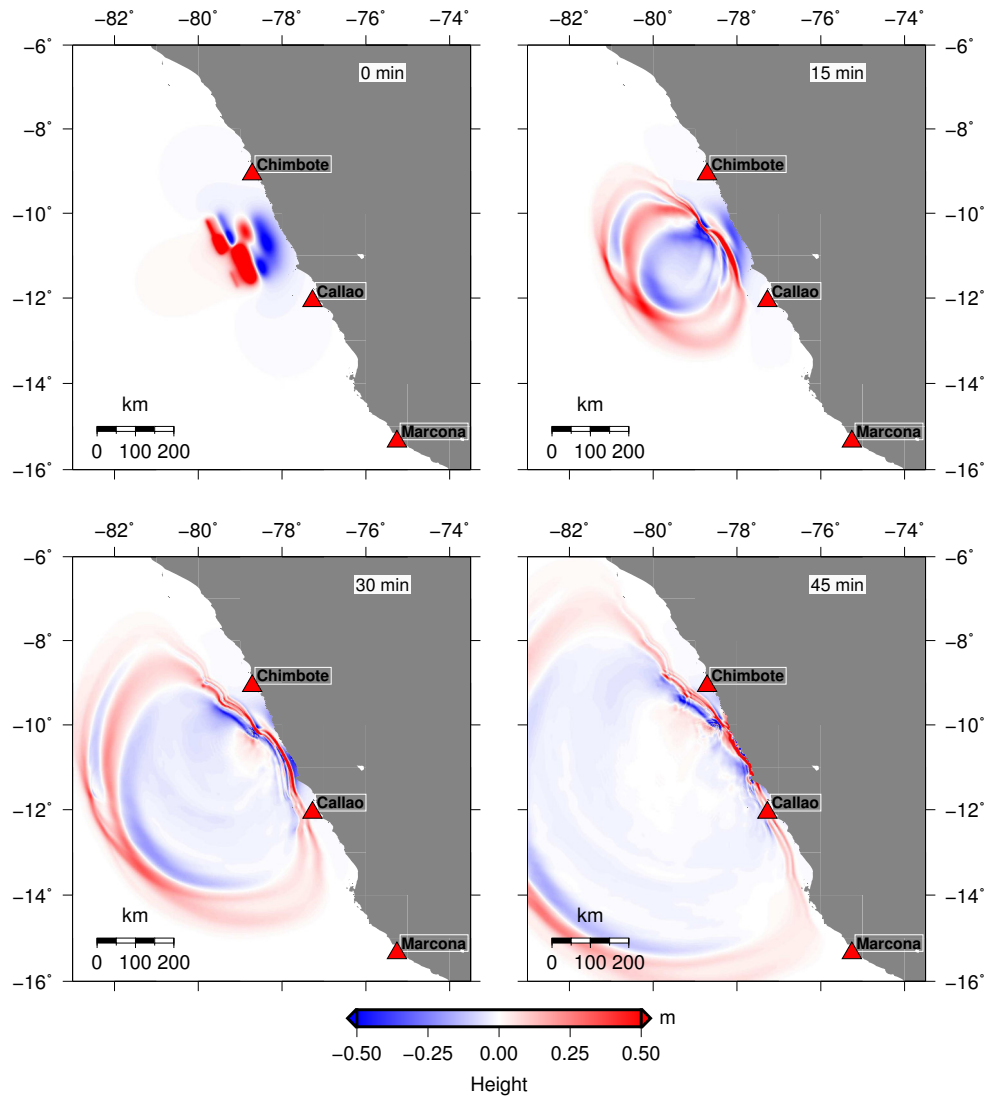
FIGURE 4.6: Propagation of the tsunami for $t = 0$ (initial condition), 15, 30 and 45 min. The red color represents the maximum values of wave height (m) while the blue color represent the minimum values.

Scalar "tsunami" moment

From the seismic source distribution and the dimensions of each subfault, it is possible to calculate the scalar seismic moment, which is defined as $M_0 = \mu LWD$, where M_0 is the seismic moment, $\mu = 4.0 \times 10^{10}$ N/m^2 is the average rigidity of the elastic medium, $L = 200$ km total length of the fault, $W = 120$ km is the total width of the fault and $D = 2.27$ m, is the mean slip or dislocation. The total seismic moment was $M_0 = 2.07 \times 10^{21}$ Nm, equivalent to a moment magnitude of Mw 8.1. Therefore, from tsunami waveforms is posible to calculate a moment magnitude equivalent to seismic moment calculated from the seismic waveforms by Abe (1972) and reported by Kanamori (1977) [Kan77]. However, both estimations have some degree of uncertainty.
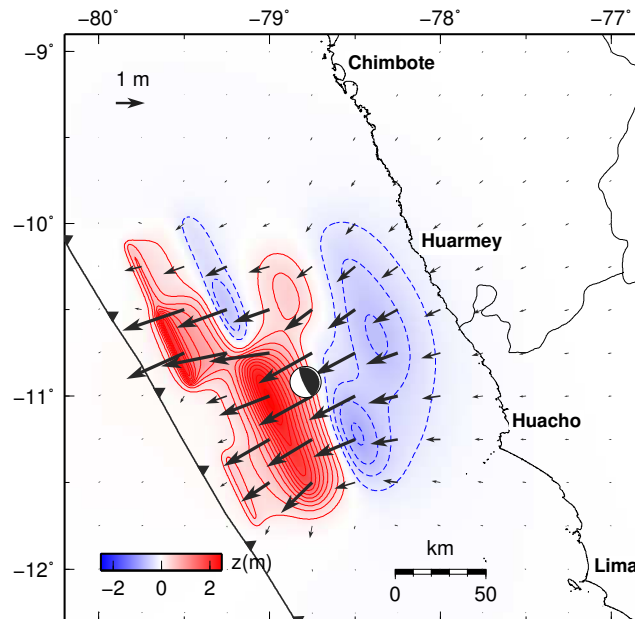
FIGURE 4.7: The positive values of the vertical component of the coseismic deformation in red and the negative values in blue are shown. The vectors represent the horizontal component of coseismic displacement. The focal diagram represents the epicenter.

Coseismic deformation and displacements

As a coseismic effect due to the occurrence of a great earthquake in a subduction zone (such as Huacho 1966), the earth's surface is abruptly and permanently deformed in the near field, forming a pattern of areas of coseismic uplift and subsidence (Figure 4.7). In general, if the seismic source is in the sea offshore, then the coastal points will undergo a coseismic subsidence; but if the seismic source is on the coast or very close to the coast, then these points could undergo a coseismic uplift, as occurred in Paracas-Ica, which uplifted around 50 cm [Oco08], during the 2007 Pisco earthquake [Jim14].

In Figure 4.7 the pattern of coseismic deformation of the crust in the region of the source is observed, the red colour represents the uplift and the blue colour represents the coseismic subsidence. Due to the position of the rupture area, the cities of Huacho and Huarmey suffered a small coseismic subsidence. The vectors represent the horizontal component of coseismic displacement and have a homogeneous behavior pointing in a South-West direction (towards the ocean), reaching an amplitude of more than 2 m near the main asperity. This implies the coseismic displacement of the cities of Huacho and Huarmey towards the sea.

This displacement pattern is consistent with the elastic rebound theory [Udi14]. In the interseismic period, the vectors of displacement and velocity point eastward towards the continent; while in the coseismic phase the tectonic stresses are relaxed and the system bounces in the opposite direction (towards the sea), as shown in Figure 4.7.

4.5 Conclusions

The results of the checkerboard test show that it is still possible to reconstruct, with some approximation, the complex process of rupture for a synthetic (and also a real) event, by inversion of 3 tsunami recordings with good azimuthal distribution, despite we do not account for data oceanward of the seismic source. The size of the subfaults can play an important role, to keep the linearity of the process, their dimensions must be greater than 30 km, at least for the Peruvian bathymetry case.

The distribution of the tsunami source, obtained in this investigation, for the 1966 Huacho earthquake, shows a high concentration of asperities or zones of greater seismic energy release in the southern side of the rupture geometry in front of the cities of Huacho and Supe, which is consistent with the macro-seismic intensity reported in these cities (VIII MM).

The solution of the inversion problem is not unique, since we choose the set of slip or dislocation parameters that provide the best fit between simulated and observed data (based on the non-negative least squares method).

To optimize the inversion results, additional tsunami waveforms should be used; however, the stations of Talara and Matarani (to the north and to the south respectively from the epicenter) did not record significant amplitudes of the event. In addition, "it is important to have a good azimuthal distribution of the tide stations around the tsunami source". On the other hand, the result will depend on the quality of the tsunami data (which in this case is regularly good, being analog records of old mechanical instruments) and the quality of the bathymetry around the stations.

The rupture process, which began at the focus or hypocenter, showed a bidirectional directivity along the azimuthal direction towards the north and, to a lesser extent, towards the south. The scalar seismic moment obtained was $M_0 = 2.07 \times 10^{21}$ Nm and the moment magnitude of the earthquake inferred from the tsunami waveforms is Mw 8.1.

To validate or verify the proposed tsunami source model, we compare the simulated and observed tsunami waveforms. In this sense, the set of observed and simulated waveforms from Chimbote station had the highest correlation coefficient (0.97). The normalized error or variance of the inversion process was 0.03.

In general, our results agree with that obtained by another researchers. For example, we have obtained the scalar seismic moment as 2.07×10^{21} Nm based on tsunami waveform inversion while Abe (1972) obtained 2.0×10^{21} Nm based on teleseismic waveform inversion. On the other hand, Kanamori (1977) assigns a moment magnitude Mw8.1 based on the scalar seismic moment from Abe (1972), similar to our results.

Chapter 5

Seismic source of the 2001 Camana-Peru earthquake (Mw 8.3) from joint inversion of geodetic and tsunami data

In this chapter, it was obtained the seismic source distribution of the 2001 Camana Earthquake. The joint inversion of observed tsunami and geodetic data stations were used to the evaluation. A coseismic effect was the generation of a local tsunami, which after 15 minutes, caused the flood and destruction of the beach resorts of Camana. Another coseismic effect was the coastal zone subsidence in the source region, evidenced by geodetic observations. The subsidence evaluated in Camana was around 82 cm, which agrees with observed Global Posittioning System (GPS) measurement of 84 cm, in contradiction to previous studies predicting a coseismic uplift of the coast of Arequipa and Moquegua. The calculated distribution of the seismic source shows a maximum slip of 14.8 m, corresponding to the main asperity located in the sea off Camana. The calculated moment magnitude of Mw 8.3 for the seismic event, was obtained from the joint inversion of tsunami and geodetic data.

5.1   Introduction

Teleseismic body waveforms can resolve temporal and spatial variations of the seismic rupture process, along the strike direction. However, the resolution in the depth direction, or along dip, is relatively poor. To overcome this limitation, we have to look another types of data,

for example, geodetic data are used for earthquakes on land, meanwhile tsunami waveforms have been used for submarine earthquakes (Satake, 1993) [Sat93].

"From a physical point of view, the joint inversion of tsunami and geodetic data provides a better result with respect to that obtained from models that use a single data set" [Jim14] (seismic, geodetic or tsunami), since the solution obtained is constrained by a greater number of data sets. The geodetic data constrains well the solution of the source located in coastal zones, but they do not have good control when the source is located in the sea far from the coast and close to the marine trench, due to the attenuation of the deformation with the epicentral distance and the low level of resolution of GPS stations. While the tsunami waveforms constrain well the solution of the seismic source located in the sea but not on the land, because a seismic source located on the land does not generate tsunami waves.

Background of previous studies

Since the occurrence of the great earthquake and tsunami in Camana 2001, many researchers have studied the seismic, geodetic and tsunamigenic aspects of this event. For example, quoting some:

Kikuchi and Yamanaka (2001), obtained the distribution of the asperities and focal mechanism from the inversion of teleseismic waves. The source time function of the seismic source indicates a duration of the rupture process of around 110 s; the rupture process starts with a small asperity around the epicenter and after 30 s the energy contained in the main asperity, of greater magnitude, spreads to the south-east. The main asperity is located in front of Camana [Kik01].

Okal et al. (2002), together with the team of researchers from the International Tsunami Survey Team (ITST), made a description and analysis of the field observations and the testimonies of the affected inhabitants about the tsunami effects, for example they measured a maximum inundation height (runup) of 8.7 m and a maximum horizontal inundation distance of 1358.5 m [Oka02].

On the part of the "Instituto Geofísico del Perú" (IGP, in spanish), Carpio et al. (2002), described the average levels of sea retreat due to the 2001 tsunami, as well as the maximum inundation heights and distances; they reported that the tsunami began 15 minutes after the earthquake of June 23 with the retreat of the sea, the same that occurred mostly between the towns of Chala and Ilo with distances ranging between 100 and 200 m. Tavera et al., (2002) made an evaluation of the macroseismic intensities, the distribution of the aftershocks and the calculation of the focal mechanism, which corresponds to a solution of inverse fault type with an almost horizontal plane dipping in the ENE direction. Ocola (2008), based on data from 3 GPS stations, conducted an analysis and evaluation of coseismic subsidence in

southern Peru due to the 2001 earthquake, finding the maximum subsidence (of 84 cm) in Camana [Oco08]

Pritchard et al., (2007) conducted the joint inversion of geodetic data (GPS + InSAR) and seismic data (teleseismic + accelerograms) to obtain the spatio-temporal distribution of the seismic source of the Camana 2001 earthquake. They obtained an average rupture velocity of 2.7 km/s, a moment magnitude of Mw 8.5 and a maximum slip of 12.8 m [Pri07].

Jimenez et al. (2011) performed the numerical simulation of the 2001 tsunami on the basis of a homogenous seismic source of dimensions 270 km by 100 km. With this seismic source, the parameters of the tsunami were obtained, such as: arrival times, the inundation zone and a synthetic tsunami waveform in Camana. The maximum height of the simulated wave is 7 m, which agrees with the reported observation [Jim11].

Chlieh et al., (2011) obtained the distribution of the seismic source of the 2001 earthquake from geodetic data (GPS + InSAR), they also calculated the distribution of the coefficient of interseismic coupling as well as the seismic potential for the central and southern Peruvian region [Chl11].

Adriano et al. (2016), evaluated the impact of the tsunami wave along the coast of Camana using a numerical model of simulation and satellite images to validate inundation levels on the coast. The distribution of the seismic source was obtained by inverting 9 tsunami records for 12 subfaults, obtaining a maximum dislocation (slip) of 11 m and a moment magnitude of Mw 8.3 [Adr16].

In this investigation, the joint inversion of tsunami waveforms recorded by 10 tidal stations with geodetic data of 16 GPS stations and an observation point (Matarani station) was conducted, to obtain the seismic source distribution: The fault plane has been divided into 21 subfaults of dimensions 43 km by 40 km. The geodetic data allow "observe" aspects that can not be obtained with the tsunami data and viceversa; however, the combination of both data sets allows obtaining better results.

Seismotectonic setting of southern Peru

Unlike the northern and central region of Peru, with a flat subduction type, the southern region of Peru is characterized by a normal subduction type, where the Nazca oceanic plate subducts beneath the continental plate with a homogeneous slope of 25° to 30°, which allows the occurrence of intense seismic and volcanic activity (Barazangi and Isacks, 1976) [Bar76].

Studies of historical seismicity report the occurrence of large earthquakes in the southern region of Peru, in 1604 (with a rupture length of 450 km, and an estimated magnitude of Mw 8.7), which caused the destruction of almost all structures over an area of approximate length

of 650 km, with generation of tsunami with wave height between 10 and 15 m (Dorbath et al., 1990). The Tacna earthquake of 1868 of magnitude estimated at Mw 9.0 [Abe79], had an estimated rupture length of 500 km and generated a tsunami with a maximum height of 14 m. It is considered that these large seismic events (1604 and 1868) are repetitive within the process of seismic recurrence [Dor90]. Significant earthquakes occurred in the interseismic period in 1687 (∼Mw 8.0) and 1784 (∼Mw 8.4), but not the magnitude of the earthquakes of 1604 or 1868. Between southern Peru (-18°) and northern Chile (-23°), the great earthquake of 1877 occurred, with a rupture length of 500 km and an estimated magnitude of Mw 9.0.

According to the studies of historical seismicity of Comte and Pardo (1991), "it is interesting to note that the rupture length of all the major historical earthquakes in the southern region of Peru, are limited by the north by a physical barrier corresponding to the Nazca Ridge" and to the south "with a geometric barrier corresponding to the change of direction of the South American coastline around Arica" [Com91].

The Camana earthquake of 2001 (Mw 8.3) and its aftershocks partially filled the seismic gap of southern Peru, which covers the rupture region of the 1868 earthquake; leaving 2 seismic gaps: the Yauca-Atico to the north and the Ilo-Arica to the south. However, the area of the main asperity of the 2001 earthquake is located in the sea near the coast and in front of the city of Camana, which suggests the existence of a possible seismic gap located near the marine trench, as is evident in this investigation (Figure 5.4) and in the investigation of Villegas et al., (2016) on the estimation of the interseismic coupling coefficient in Peru and the distribution of the seismic gaps [Vil16].

It is worth mentioning the role played by the Nazca Fracture (Figure 5.1), "since the subduction of the same leads to the complexity of the Camana 2001 earthquake rupture process" (Robinson et al., 2006) [Rob06]. The subduction zone of this tectonic structure has a low interseismic coupling coefficient (less than 0.6) [Chl11].

5.2 Acquisition and digital data processing

Tsunami data

To conduct this research, the data was obtained from different sources such as the tidal recordings of 10 digital tide gauge stations, which belong to the global tide network "Sea Level Station Monitoring Facility" (www.ioc-sealevelmonitoring.org), located in ports and coastal creeks. All these stations are located on the coast of Peru and Chile, except Santa Cruz station located in the Galapagos Islands and JUAN station located on Juan Fernandez Island (Figure 5.1). Figure 5.1 shows a good azimuthal distribution of the stations
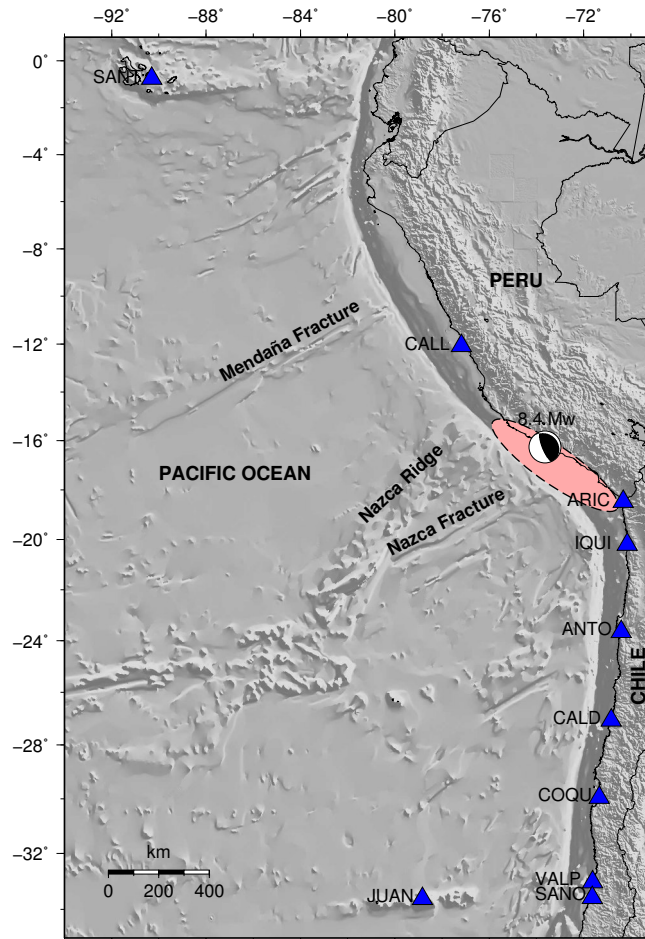
FIGURE 5.1: Distribution of the tide gauges and bathymetry. The focal diagram represents the focal mechanism in the location of the source. The blue triangles represent the tidal stations.

with respect to the seismic source; the ideal case would be to have a station offshore in front of the seismic source.

"All mareographic signals are composed of a wide spectrum of frequencies with two main components such as tides, waves and an episodic component such as tsunami waves" [Jim14]. The digital signal processing algorithms [Jim07] must be applied to study the tsunami waveforms. "First the data was interpolated with a sampling rate of 1 minute, using the cubic interpolation method, in order to homogenize the data, because each station has a different sampling rate, 1 min, 2 min or 5 min" [Jim14]. Then, the average value of the signal is removed to center it with respect to the abscissa axis. Likewise, we applied an 80-term polynomial interpolation filter to remove the very long period components (tides) and a low-pass filter constituted by the moving average of 3 consecutive samples of the signal to remove short-period components (surges), according to the equation 5.1, where y is the original signal and y_f is the filtered signal. "Finally, the time is referenced with respect to the origin time of the earthquake" [Jim14].

TABLE 5.1: Location of tide gauges used in the inversion process. The arrival time (TA) is measured from the origin time of the earthquake.

N	Station	Lati (°)	Long (°)	TA (min)
01	Santa_Cruz	-00.7520	-90.3070	238
02	Callao	-12.0710	-77.1740	093
03	Arica	-18.4760	-70.3230	035
04	Iquique	-20.2050	-70.1480	038
05	Antofagasta	-23.6530	-70.4040	060
06	Caldera	-27.0650	-70.8250	091
07	Coquimbo	-29.9500	-71.3350	122
08	Valparaiso	-33.0270	-71.6260	147
09	San Antonio	-33.5800	-71.6300	153
10	Juan_Fernandez	-33.6200	-78.8300	151

$$y_f(j) = \frac{y(j-1) + y(j) + y(j+1)}{3} \tag{5.1}$$

Geodetic data

Coseismic displacement data from a total of 17 stations have been used, of which 14 geodetic data or coseismic displacements were obtained from the publication of Pritchard et al. (2007). The remaining 3 data were obtained from the Ocola publication (2008) for the Camana and Ilo stations, and a seismic subsidence data recorded by the Matarani tidal station (Figures 5.2, 5.3 and Table 5.2).

Most of these geodetic measurements were conducted episodically (through annual observation campaigns), so the coseismic displacement data would be slightly overestimated (since the calculation would take into account the postseismic displacement component) and they would not be very reliable, which explains the poor correlation between the observed and simulated displacement vectors (Figure 5.3).

Bathymetry data

"The velocity and directivity of the tsunami waves depend on the bathymetry or marine topography" [Jim14], so it is necessary to have a good bathymetry model for the calculation of the Green functions (or elementary mareograms), by means of a numerical model of propagation of tsunami waves. The global bathymetry has been taken from the GEBCO 30 model (http://www.gebco.net), which has a resolution of 30 arcseconds or ~927 m approximately (Figure 5.1).

TABLE 5.2: Location of geodetic stations and observation points. U_x represents the co-seismic displacements in the x component. NaN (Not a Number) means that data is not available. CAM, ILO and MATA stations were taken from Ocola (2008) and the rest from Pritchard et al., (2007).

N	Station	Long (°)	Lati (°)	U_e (m)	U_n (m)	U_z (m)
01	CAM	-72.7115	-16.6248	-0.851	-0.423	-0.839
02	ILO	-71.3453	-17.6463	-0.409	0.068	-0.163
03	MATA	-72.1088	-17.0010	NaN	NaN	-0.150
04	AREQ	-71.493	-16.4660	-0.416	-0.299	-0.026
05	AYRO	-69.880	-17.750	-0.175	0.005	-0.014
06	BAJO	-70.350	-16.950	-0.346	-0.124	-0.064
07	CMOR	-70.660	-18.050	-0.206	0.014	-0.055
08	COMA	-68.440	-17.040	-0.040	-0.027	0.002
09	JHAI	-72.8570	-16.5180	-0.888	-0.604	-0.234
10	LAMP	-70.340	-15.330	-0.120	-0.113	0.004
11	MACU	-70.410	-14.080	-0.041	-0.050	0.000
12	MDRG	-71.820	-15.590	-0.182	-0.215	NaN
13	MIST	-71.430	-16.300	-0.352	-0.264	-0.028
14	PNAS	-68.490	-16.230	-0.046	-0.025	0.010
15	POCO	-71.370	-17.430	-0.782	-0.146	-0.068
16	SIGN	-71.540	-16.490	-0.515	-0.365	NaN
17	TANA	-74.450	-15.750	-0.230	0.015	NaN

The bathymetry in southern Peru is relatively deep (the depth of 1 km is 25 km from Camana) and the distance from the marine trench to the Camana coast (115 km) is less than that of central Peru (around 150 km). The velocity of the tsunami wave is proportional to the root of the bathymetric depth, so the arrival time of the first wave of the tsunami to the Camana area would be very short. The witnesses stated "that the arrival time of the first tsunami wave was around 15 minutes" (Carpio et al., 2002).

Hypocentral parameters, focal mechanism and aftershocks

The hypocentral parameters were calculated and reported by the Geophysical Institute of Peru (IGP). The epicenter was located at: Latitude = -16.20°, Longitude = -73.75°, with a depth of 29 km (Table 5.3). The National Earthquake Information Center (NEIC) reported a moment magnitude of Mw 8.4. The "Global Centroid Moment Tensor" (CMT) calculated the fault plane orientation or focal mechanism from inversion of teleseismic waveforms, with these parameters: azimuth = 305°, dip = 18° and rake angle = 63°, (Table 5.3). Therefore, the 2001 earthquake represents an event of the thrust fault type with a small dip angle.
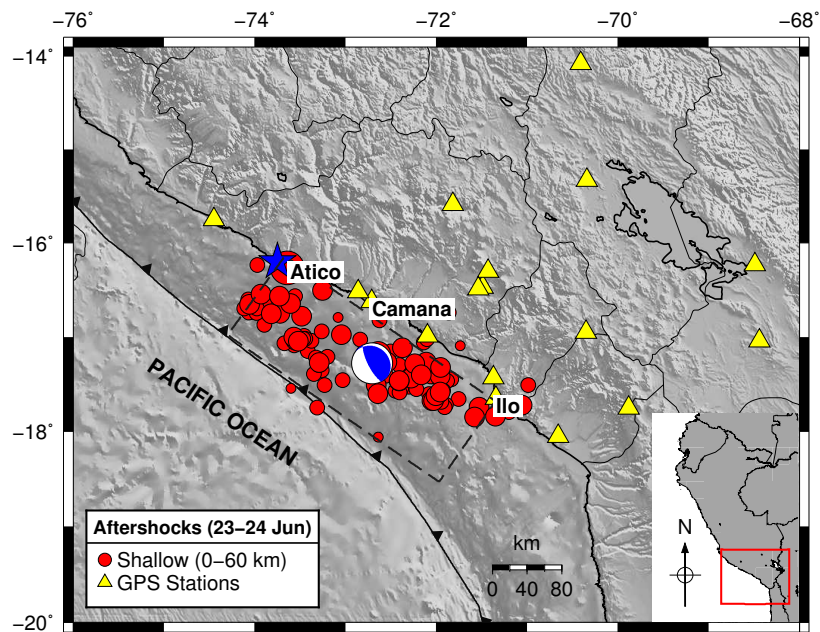
FIGURE 5.2: Aftershocks (red circles) within 24 hours and spatial distribution of the geodetic stations and observation points (yellow triangles).
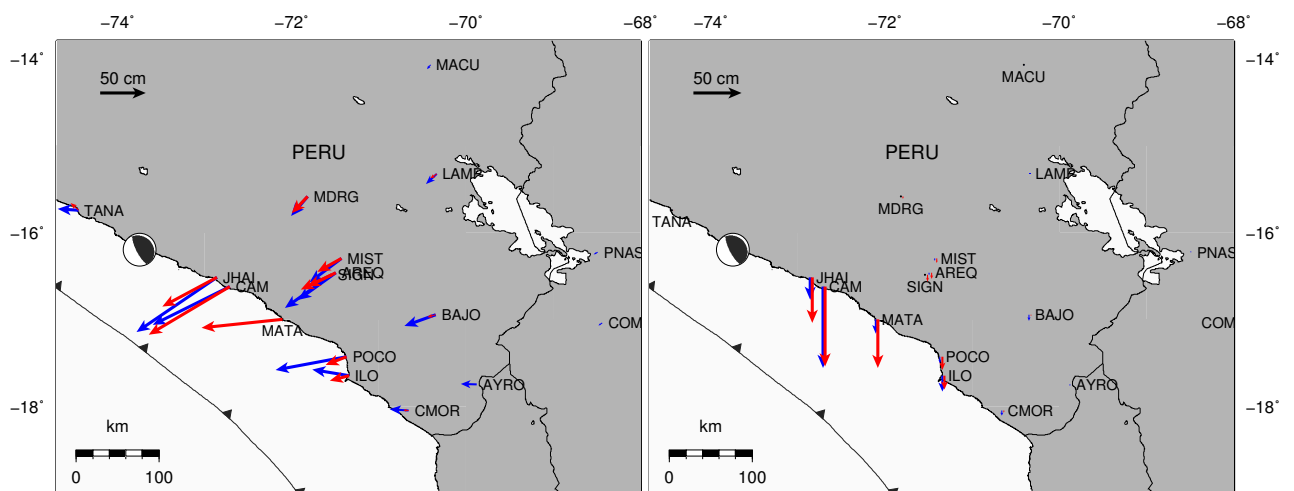
FIGURE 5.3: Coseismic horizontal vectors (left) and vertical (right), observed (blue) and simulated (red). Matarani tidal station (MATA) only recorded the vertical offset before and after the earthquake. Observed data of Pritchard et al., (2007) and Ocola (2008).

According to NEIC, there were a total of 126 aftershocks of shallow depth (less than 60 km) of magnitude between 4.0 and 5.9 Mw, in the first 24 hours, namely from the occurrence of the main earthquake (June 23, 2001) until June 24 of the same year.

The aftershocks (of shallow focal depth) are distributed mainly between the coast line and the marine trench, along the rupture area, approximately from Atico to Ilo, covering a surface with an effective area of around 300 km long by 120 km wide (Figure 5.2).

TABLE 5.3: Hypocentral parameters according to the IGP, the magnitude according to NEIC and the focal mechanism according to the CMT catalog.

Date	23 Jun 2001
GMT Time	20:33:14
Latitude	-16.20°
Longitude	-73.75°
Depth	29 km
Magnitude	Mw 8.4
Strike	$\theta = 305°$
Dip	$\delta = 18°$
Rake	$\lambda = 63°$

5.3 Methodology

The spatial dimensions of the seismic source can be estimated from the distribution of the aftershocks under the hypothesis that most aftershocks, particularly those that occur after the main earthquake, occur on or near the seismic rupture area (Lay and Wallace, 1995). From the distribution of the aftershocks (occurred within the first 24 hours) the geometry of the seismic source was obtained (Figure 5.2), which has dimensions of 300 km by 120 km. The orientation of the rupture plane is given by the parameters of the focal mechanism (Table 5.3).

In the research of Adriano et al., (2016) the seismic source was discretized in 6×2 subfaults of dimensions 50×50 km^2. In this investigation, the geometry of the seismic source was discretized in 21 rectangular subfaults, 7 in the direction of the azimuth and 3 subfaults in the direction of the dip. Each subfault has a dimension of 43×40 km^2 (Figure 5.4). This discretization allows obtaining results in greater detail.

The focal mechanism is the same for all subfaults. However, the depth of each subfault depends on its position in the direction of the dip.

The 3 components (North, East and Vertical) of the deformation field were calculated for each subfault, taking into account an unitary slip. The numerical deformation model ED-GRN/EDCMP was used, according to the formulation of Wang et al. (2003) for an elastic, isotropic and stratified medium [Wan03]. The velocity structure is given in Table 5.4.

Green function calculation

The geodetic Green functions show the synthetic coseismic displacements in the location of the GPS stations, due to a unitary slip in each subfault.

To obtain the distribution of the seismic source, it is necessary to calculate the Green functions, that is, the coseismic displacement generated in the location of the i-th geodetic station due to the unitary deformation of the j-th subfault: $G_{ij} \times m_j = d_i$, where, G_{ij} is the Green function of the i-th station generated by the j-th subfault, m_j is the dislocation or *slip* in the j-th subfault, d_i is the observed coseismic displacement (for the 3 components: north, east and vertical) in the i-th geodetic station. The coseismic deformation field was calculated based on the formulation of Wang et al. (2003) for an elastic, isotropic and stratified medium. The model of seismic wave velocities for southern Peru [Vil09] is shown in Table 5.4.

"From the physical point of view, a Green function represents the response of the system, simulated signal in the i-th station, when that system is disturbed by a unitary impulse, a deformation due to the unitary dislocation in the j-th subfault" [Jim14]. The tsunamigenic Green functions come to be the synthetic tsunami waveforms in the tidal stations due to a unitary dislocation in each subfault.

Using "the coseismic deformation field as an initial condition, waveforms or Green functions have been calculated in each tide station simulating the propagation of the tsunami by the finite difference method for each subfault, using a real bathymetry" [Jim14]. The observed tsunami waveforms in each station are expressed as a linear superposition of the synthetic waveforms: $G_{ij}(t)m_j = d_i(t)$, where $G_{ij}(t)$ is the time-dependent Green function in the i-th tidal station generated by the j-th subfault, m_j is slip amplitude in the j-th subfault and $d_i(t)$ is the observed tsunami waveform in the i-th station.

To obtain the Green functions corresponding to the tide gauge stations of Peru and Chile, a modified version of a tsunami propagation model (TUNAMI) was used for a single computational grid [IOC97]. In this propagation grid a linear model was used for a regular bathymetric grid in spherical coordinates based on the linear hydrodynamic theory of shallow water. The differential equations of continuity and conservation of linear momentum are numerically integrated using the finite difference method under the numerical scheme of the "leap frog". A numerical stability condition CFL (Courant Friedrichs and Lewy) less than 0.8 is established to avoid numerical instabilities.

The initial conditions are taken from the theory of deformation for an elastic and stratified medium [Wan03]. The border conditions on the coast for the linear model (propagation grid), suppose a vertical wall. The boundary conditions at the oceanic edges are open, to avoid reflections at the edges a sponge-like condition is added to absorb the energy of the wave. "The numerical model does not take into account the effects of dispersion (non-linear effects), which for this case, because it is a near-field and regional event, are not appreciable" [Jim18].

TABLE 5.4: Velocity structure model of seismic waves in the vicinity of the seismic source (southern Peru). The thickness of the lithospheric layer is represented by t (Villegas, 2009) [Vil09].

N	v_p (km/s)	v_s (km/s)	ρ (g/cm^3)	t (km)
01	4.50	2.54	2.60	02
02	5.50	3.11	2.60	03
03	5.90	3.33	2.90	10
04	6.10	3.45	3.38	10
05	6.50	3.67	3.38	10
06	6.80	3.84	3.38	15
07	7.70	4.35	3.37	∞

Joint inversion process

Because there are 2 datasets (tsunami and geodetic), the set of equations are modified as follows:

$$\begin{pmatrix} G_t \\ G_g \end{pmatrix} \times m = \begin{pmatrix} d_t \\ d_g \end{pmatrix} \tag{5.2}$$

where G_t represents the tsunami Green function, d_t the tsunami waveforms, G_g represents the geodetic Green function and d_g the coseismic displacements in its three components: north, east and vertical.

After combining the geodetic and tsunami data and Green functions, a "joint" inversion was conducted using the non-negative least squares method [Law74], which consists of comparing the simulated data with the observed data and minimizing the square of the residual: $|G_{ij}m_j - d_i|^2 \rightarrow 0$, with the condition $m_j \geq 0$. Due to the fact that the tide gauge stations are located in ports and bays, it is advisable to consider "the part of the tsunami signal corresponding to the first period of the tsunami wave to avoid problems of contamination of the signal with reflection effects and local resonances, due to the bathymetry and morphology of the coast around each station" [Jim14]. So, for purposes of calculating the inversion, a 45 minutes time window was taken from the start of the arrival of the wave (except for the Santa Cruz station with a time window of 25 minutes and the Juan Fernandez station with 20 minutes). We obtained $N_i = 459$ data for $N_j = 21$ unknowns, which constrain the non-linear part of the time window.

TABLE 5.5: Distribution of the seismic source of the Camana earthquake of 2001. The dimensions of each subfault are the same: $L = 43$ km and $W = 40$ km. The coordinates correspond to the lower left corner of each subfault. H represents the depth of the upper part of the subfault.

N	Lat (°)	Lon (°)	Slip (m)	Error (m)	H (m)
1	-18.5300	-71.9700	0.52	0.33	6300
2	-18.2484	-71.7633	0.53	0.41	18661
3	-17.9668	-71.5566	1.93	0.91	31021
4	-18.3071	-72.3037	0.56	0.41	6300
5	-18.0256	-72.0970	0.00	0.01	18661
6	-17.7440	-71.8903	0.00	0.06	31021
7	-18.0843	-72.6373	0.00	0.11	6300
8	-17.8027	-72.4306	0.00	0.00	18661
9	-17.5211	-72.2239	0.00	0.54	31021
10	-17.8614	-72.9710	0.00	0.18	6300
11	-17.5798	-72.7643	0.00	0.35	18661
12	-17.2983	-72.5576	12.69	5.48	31021
13	-17.6386	-73.3046	0.00	0.38	6300
14	-17.3570	-73.0979	0.00	0.04	18661
15	-17.0754	-72.8912	14.79	9.50	31021
16	-17.4157	-73.6383	0.00	0.13	6300
17	-17.1341	-73.4316	0.00	0.00	18661
18	-16.8525	-73.2249	0.00	0.21	31021
19	-17.1928	-73.9720	0.00	0.16	6300
20	-16.9113	-73.7653	0.00	0.09	18661
21	-16.6297	-73.5586	5.55	2.23	31021

"The inversion algorithm guarantees that all the values of the slip or dislocation are positive, as a necessary condition from the physical point of view" [Jim14]. The result of the inversion is shown in the Table 5.5. The error or normalized variance of the inversion process is 0.37.

5.4 Results and Discussion

Seismic source distribution

Figure 5.4 shows the distribution of asperities or areas of greater seismic energy release. The results show a small asperity around the epicenter and then the greater asperity is located in front of the city of Camana, which explains the purely local character and the great impact that the flood caused by the tsunami had in that city. The distribution of the seismic source obtained by the joint inversion of tsunami and geodetic data agrees, in general, with the pattern obtained by Kikuchi and Yamanaka (2001) by inversion of teleseismic waves [Kik01].
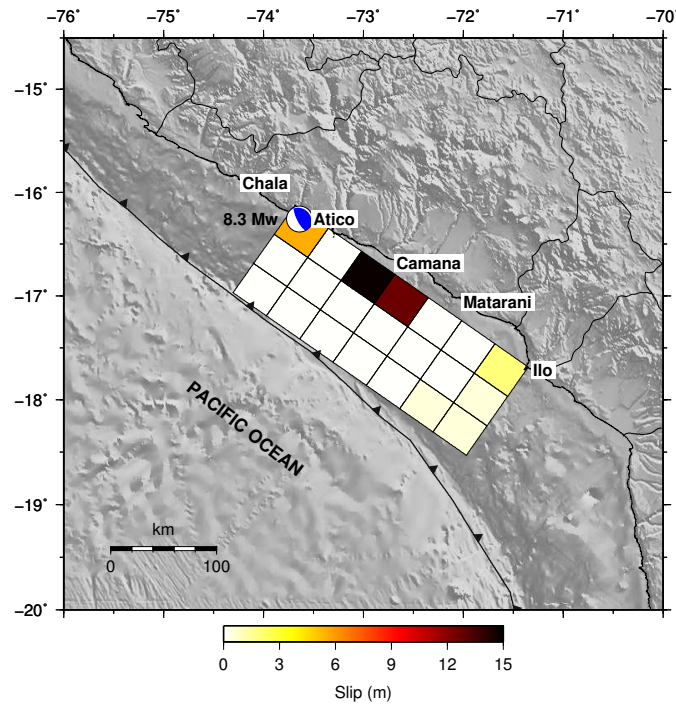
FIGURE 5.4: Distribution of the asperities of the 2001 Camana earthquake. The main asperity (in black and brown) is located in front of Camana. Notice the subfaults near the marine trench (white color) that have not been fractured and the subfaults with a small dislocation (in cream color).

The position of the subfaults and the values of the *slip* are shown in Table 5.5. The maximum *slip* was estimated at almost 14.8 m, located in front of Camana. The average value of the *slip* was estimated at 1.8 m. The subfaults adjacent to the trench show small or null slip, suggesting that the tectonic stresses in this area have not been completely relaxed, maintaining a high potential for the possibility of a new earthquake in the updip.

Scalar tsunami moment and magnitude

Having the distribution of the dislocation or *slip* and the dimensions of each subfault, it is possible to calculate the scalar seismic moment M_0 that is defined according to equation 2.9, where $\mu = 5.0 \times 10^{10}$ N/m^2 is the average rigidity of the elastic medium, $L = 300$ km total length of the source, $W = 120$ km is the total width of the source and $D = 1.83$ m, is the mean dislocation (slip). The total scalar seismic moment is $M_0 = 3.3 \times 10^{21}$ Nm, and according to the relation $M_w = \frac{2}{3} \log(M_0) - 6.07$, a magnitude of Mw 8.3 is obtained in the moment scale. This means that a value almost similar to the magnitude of Mw 8.4 calculated from the teleseismic recordings by the USGS was obtained from the tidal stations.
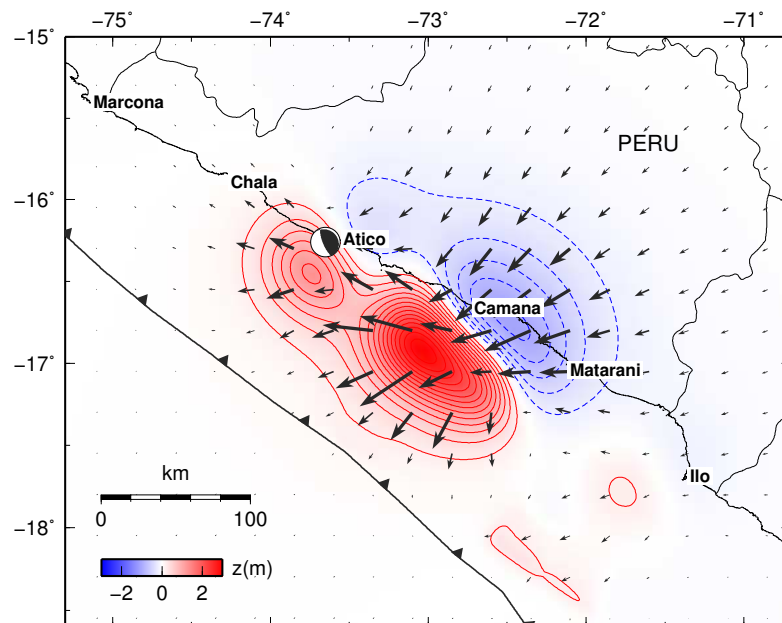
FIGURE 5.5: Coseismic deformation field. The blue areas indicate the subsidence and the red areas indicate the uplift. The arrows represent the horizontal coseismic displacement vectors. The focal sphere represents the location of the epicenter.

Coseismic deformation

After the occurrence of a large earthquake in a subduction zone (such as Camana 2001), the earth's surface is abruptly and permanently deformed in the near field as a coseismic effect, generating a pattern of coseismic uplift and subsidence zones (Figure 5.5). In general, if the seismic source is in the sea far from the coast, then the coastal points will suffer a coseismic subsidence; but if the seismic source is on the coast or very close to it, then the coastal points could suffer a coseismic uplift.

Figure 5.5 shows the vertical component of the coseismic deformation field due to the Camana earthquake of 2001. It is observed that a large part of the coastal zone of southern Peru suffered a coseismic subsidence, which agrees with the geodetic data observed at the Camana station: -84 cm, Ilo station: -16 cm and the Matarani tide gauge: -15 cm (Ocola, 2008).

The zone of maximum deformation or vertical uplift is located in the sea off the city of Camana, this explains why the greatest impact of the tsunami occurred in this city, with tsunami waves up to 7 m high.

The vectors of horizontal coseismic displacement point towards the sea and in the South-West direction, in the opposite direction to the velocity vectors during the interseismic period, which evidences the theory of elastic rebound.

TABLE 5.6: Correlation coeficients between the observed and simulated tsunami waveforms of the 2001 Camana earthquake. The time window is counted from the initial arrival time.

N	Station	Time window (min)	Correlation
1	Santa Cruz	25	0.99
2	Callao	40	0.87
3	Arica	40	0.96
4	Iquique	40	0.95
5	Antofagasta	40	0.92
6	Calderas	40	0.97
7	Coquimbo	40	0.95
8	Valparaiso	40	0.93
9	San Antonio	40	0.97
10	Juan Fernández	20	0.94

Comparison of observed and simulated waveforms

Figure 5.6 shows the results of the inversion by comparing the observed waveforms of the tsunami (in blue) and simulated (in red). In general, it is observed that there is a good correlation between the observed wave and the simulated wave. However, the presence of some tide gauge station west of the seismic source would have allowed a much better result.

In Table 5.6, the correlation coefficients between the observed signal and the simulated signal for each tide station are shown. The station of Santa Cruz presents the best value of the correlation coefficient (0.99), while the station of Callao has the lowest correlation (0.87), because of the bathymetry resolution (30 arc second) used in the computational modeling. In the Juan Fernández station from the 170th minute onwards, the non-linear effects prevail, such as the local resonances of short period; this time window has not been taken into account in the inversion process (Figure 5.6).

Figure 5.7 shows the waveform of the tsunami for a virtual tide station located in Camana. The maximum height of the synthetic wave was 7.7 m and corresponds to the third wave. The simulated arrival time was approximately 15 minutes. Before the arrival of the tsunami, there is a decrease in sea level due to coseismic subsidence.

Seismotectonic implications

In the case of the Camana 2001 event, both Kikuchi and Yamanaka (2001) [Kik01] and Pritchard et al. (2007) [Pri07], obtained a distribution of the dislocation (from teleseismic inversion) with a great asperity on the south-east side of the rupture plane, which extends (in the direction of the dip) from the trench to the continent. Both models predict a coseismic uplift of the coast of Arequipa and Moquegua, which does not agree with the observed GPS
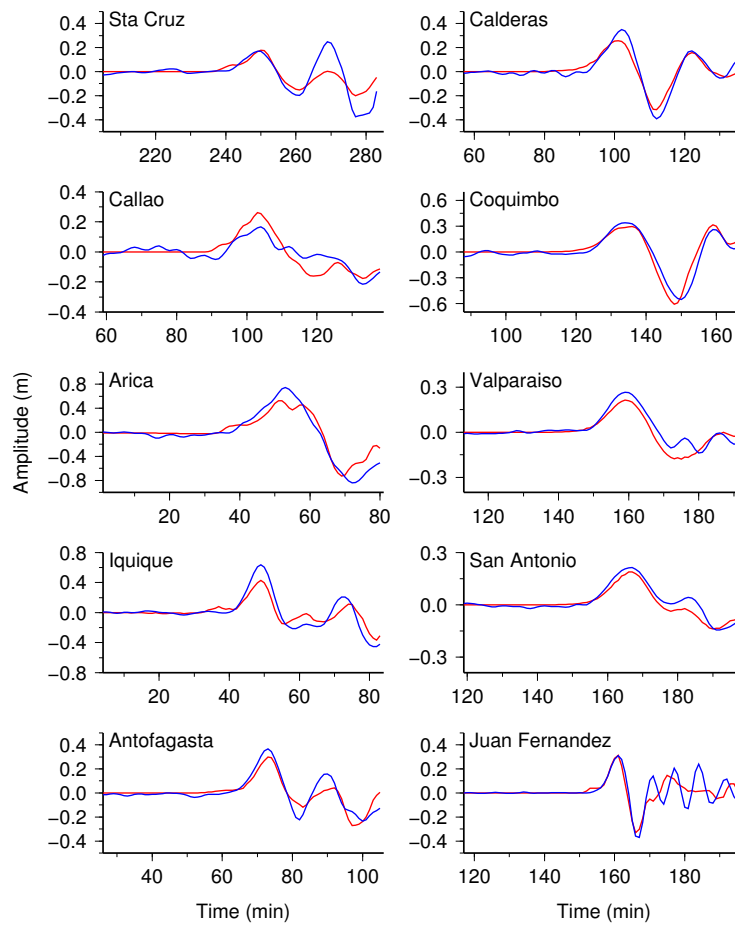
FIGURE 5.6: Comparison of the observed tsunami waveforms (in blue) and simulated (in red) of the 2001 Camana earthquake. For the case of Santa Cruz and Juan Fernández stations, only a time window shorter than a period was used for the inversion calculation.
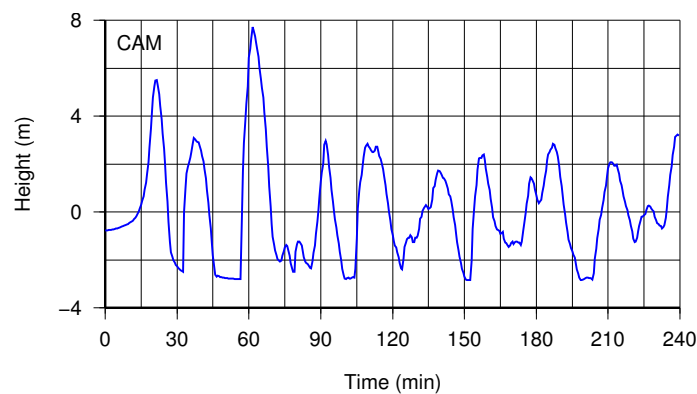
FIGURE 5.7: Simulated waveform of the tsunami in Camana. The third wave was the largest with a height of 7.7 m. The arrival time was around 15 min. There is no tidal station in Camana.

data of subsidence in Camana, Ilo and with the vertical subsidence of the Matarani tide gauge.

The pattern of vertical deformation that was obtained from the teleseismic inversion, indicates that the city of Camana was uplifted (instead of subsidizing) and close to the trench there was an appreciable dislocation or slip, according to what was obtained by Kikuchi and Yamanaka (2001) and Pritchard et al., (2007). However, a 84 cm subsidence measured by the GPS station was reported in Camana, which agrees with our theoretical model of 82.4 cm of subsidence. Therefore, the seismic model of Kikuchi and Yamanaka (2001) and Pritchard et al. (2007) does not fit the geodetic observations.

On the other hand, in the model of Chlieh et al. (2011), obtained by inversion of geodetic data (GPS + InSAR), a great asperity is observed almost in the whole rupture area [Chl11]. However, the tsunami data indicates a large inundation in Camana and a small inundation in Matarani and Ilo (located to the south east of Camana), which implies a priori, the existence of a great relative asperity near Camana and a small asperity relative to Matarani and Ilo. Therefore, the model of Chlieh et al. (2011) does not satisfy the observations of the tsunami.

According to this investigation, the slip distribution or seismic source distribution, for the event of Camana 2001, shows a small asperity near the trench (Figure 5.4), so that there is some agreement with the results of Pritchard et al. (2007) [Pri07], on the side of the trench but not on the side of the land.

This apparent discrepancy is due to the bandwidth of the seismic signals and geodetic data used in each inversion process. The ideal case would be to conduct a joint inversion of 2 or more data sets.

The combination of the geodetic and tsunami data allows to obtain a small asperity around the epicenter (which agrees with the teleseismic models), which is not possible to obtain using only tsunami data (as the result of Adriano et al., 2016 [Adr16]).

5.5   Conclusions

The joint inversion of tsunami and geodetic data provides a better result with respect to the results of models that use a single data set (seismic or tsunami), since the solution obtained is better constrained by a greater number of data. However, in the case of the Camana 2001 event, there is a predominance of tsunami data on geodetic data, so that the correlation is better between tsunami waveforms and is poor in the case of horizontal displacement vectors.

The distribution of the seismic source, obtained in this investigation, for the Camana earthquake of 2001, shows a great concentration of asperities (areas of greater seismic energy

release) in front to the city of Camana, which agrees with the macroseismic intensity reports in this city (VIII MM).

The use of a greater number of subfaults (in this case 21) in the inversion process allows us to model the tsunami waveforms in greater detail, thus achieving a better correlation, which is not achieved with a smaller number of subfaults.

The maximum dislocation or *slip* is 14.8 m and is located near the central part of the rupture area, specifically, in front of the city of Camana, in the sea and close to the coast. The maximum amplitude of the vertical component of coseismic deformation for this model is 2.8 m.

The rupture process started in the focus or hypocenter, and presented a unidirectional directivity along the azimuth direction towards the South-East. The scalar seismic moment was estimated at $M_0 = 3.3 \times 10^{21}$ Nm, which corresponds to a magnitude of Mw 8.3, a value almost similar to that calculated by the USGS (Mw 8.4) by inversion of teleseismic body waveforms. Therefore, the tsunami + geodetic model does work.

There would be a high potential of accumulated stresses that have not been completely relaxed, due to the occurrence of the earthquake in southern Peru in 2001, in the area near the trench (seismic gap?). This suggests the possibility of the occurrence of a large earthquake in the zone of rupture of the 2001 earthquake, perhaps with a concentration of asperities near the trench. However, the possibility that during the postseismic process, this area has undergone an aseismic creep is not ruled out.

Chapter 6

Seismic source of the 2014 Chile earthquake (Mw 8.1) from joint inversion of tsunami and geodetic data

In this research, we have calculated the slip distribution of the April 1, 2014 Chile earthquake, from the coseismic displacements of 20 geodetic stations, and from tsunami waveforms of 4 DART buoys of the global network. The maximum displacements were recorded by the geodetic station of Pisagua (PSGA), which suffered a coseismic subsidence of 29.4 cm, while the horizontal displacement was 94.9 cm in the south-west direction. Interseismic velocity vectors have also been calculated, which are consistent with the convergence pattern of the Nazca and South American plates. To model the deformation field, Green's functions have been calculated based on the theory of deformation for an elastic, isotropic and layered stratified medium. The distribution of the seismic source has been obtained from the joint inversion of coseismic displacements and tsunami waveforms. As a result, we have obtained a maximum dislocation of 6.2 m and a scalar seismic moment of 1.57×10^{21} Nm, corresponding to a moment magnitude of Mw 8.1. From the slip distribution calculated, we can deduce that there is still a high potential for generation of tsunamigenic earthquakes in northern Chile.

6.1   Introduction

The convergence velocity of the Nazca and South American plates due to the subduction process is around 65 mm/year in northern Chile (Norabuena et al., 1998). The subduction process generates the deformation in the earth's crust, which is quantified by geodetic or GPS (Global Positioning System) stations. The horizontal interseismic deformation rate in the coast of northern Chile and southern Peru is relatively small, in the order of 20 mm/year, towards the continent; however, when an earthquake of great magnitude (Mw>8) occurs, the coseismic displacement (recorded by the geodetic stations) can be of the order of several centimeters or even greater than 1 m (the horizontal component towards the sea) in the region of the source. For example, after the Camana earthquake of 2001 (Mw 8.4), the GPS station in that city recorded a coseismic subsidence of 84 cm (Ocola, 2008) [Oco08].

The crustal geodetic displacements can provide more information for a better understanding of how and where the deformation accumulates and thereby determine its origin. The time series of GPS geodetic stations located along the coast and inside the continent allow to establish the deformation velocity of the earth's crust. The Nazca plate moves under the South American plate at a ratio of 65 mm/year which corresponds to the velocity of convergence between both plates, this displacement is not homogeneous and there are areas that are strongly coupled (Barrientos, 2014) [Bar14]. According to Metois et al. (2013), the coefficient of interseismic coupling is very large in the northern region of Chile [Met13].

On April 1, 2014 a strong earthquake shook the northern region of Chile and southern Peru. According to National Earthquake Information Center (NEIC) report, the hypocentral parameters were: latitude = -19.642°, longitude = -70.817°, depth = 25 km, origin time 23:46:46 UTC, with a magnitude of Mw 8.1 (http://earthquake.usgs.gov). As a coseismic effect, a tsunami with local characteristics was generated, as a consequence the tsunami warning system was activated for the entire coast of Chile and southern Peru.

The tsunami waves spread throughout the Pacific Ocean, and they were recorded by the tide gauges of Chile and Peru, as well as by the offshore DART buoys. Another coseismic effect, although less perceived by the population, was the displacement and deformation of the crust in the neighbourhood of the seismic source, which was recorded by the GPS geodetic stations of northern Chile and some of southern Peru and by the tidal station of Pisagua (near the seismic source) that recorded the variation of the sea level before and after the event (Figure 6.3).
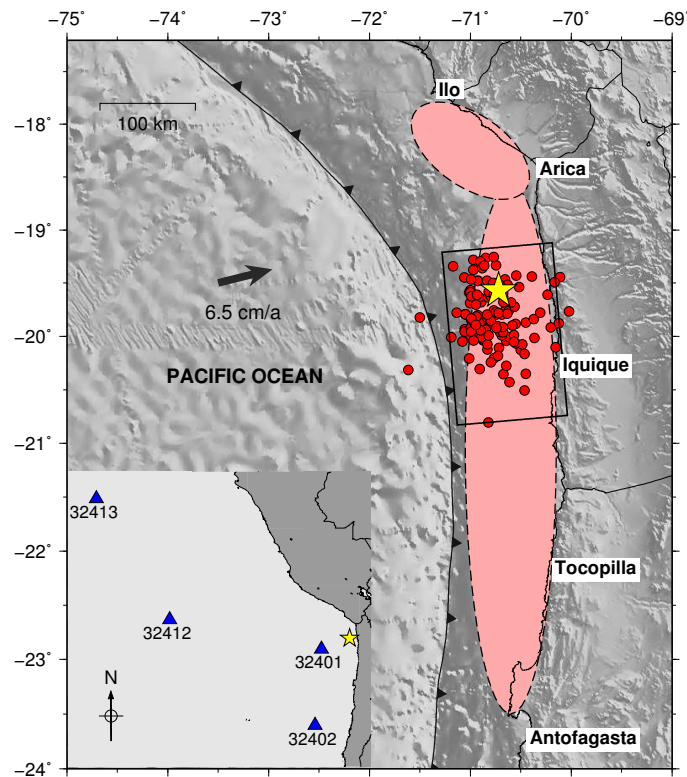
FIGURE 6.1: The ellipses represent *seismic* gaps in southern Peru (Ilo-Arica) and northern Chile (Arica-Antofagasta). The red circles represent the aftershocks of the Chile 2014 earthquake on the first day, the rectangle represents the geometry of the seismic source of dimensions: $180{\times}120$ km^2, around a quarter of the area of the seismic gap Arica-Antofagasta. The yellow star represents the epicenter. The inserted figure (lower left side) shows the location of the DART buoys.

Background of previous research

The 2014 Chile earthquake has been studied by Lay et al. (2014) who analyzed the sequence of earthquakes before and after the mainshock and obtained the distribution of the seismic source using inversion of teleseismic waves [Lay14]. Yagi et al. (2014) investigated the rupture process of the 2014 Chile earthquake in relation to the foreshock seismic activity [Yag14].

Schurr et al. (2014) used seismic data to study the evolution of the rupture process, the seismic sequence before and after the mainshock and GPS geodetic data to study interseismic deformation and interseismic coupling; they concluded that the seismic potential of this area still remains high [Sch14].

An et al., (2014) conducted the inversion of tsunami waveforms recorded by 3 DART buoys, they proposed the existence of a great asperity of $60{\times}40$ km^2 located around the epicenter; however, its inversion has not resolved the small asperity located in the southern side of the rupture geometry [Anc14].
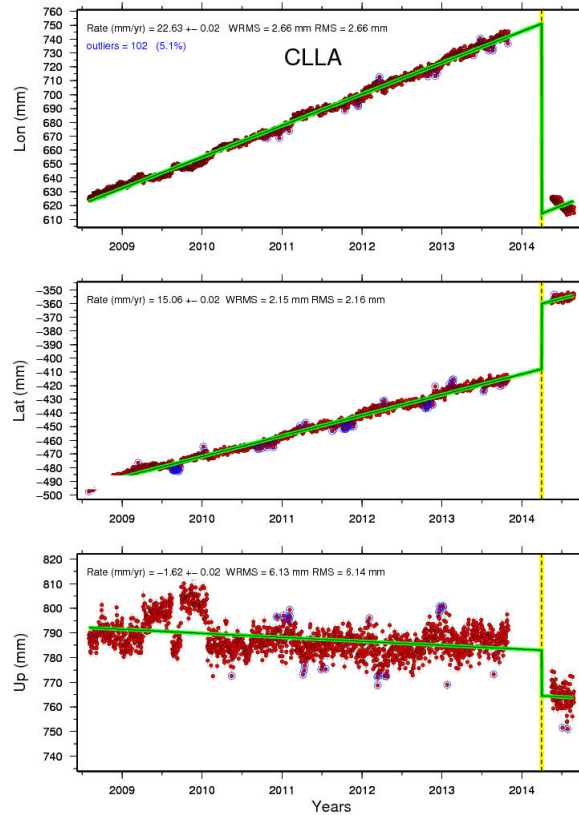
FIGURE 6.2: Time series of the CLLA geodetic station. The discontinuous vertical line indicates the time of occurrence of the seismic event: April 01, 2014. Data from Geodetic Observatory of Nevada.

Ruiz et al., (2014) studied the location and mechanism of foreshock seismic sequence; furthermore, using GPS time series, they calculated a slow slip event (occurred on March 16) in the same location as the mainshock [Rui14].

On the other hand, Gusman et al. (2015) conducted the inversion of tsunami waveforms in the near field and far field (previously they made corrections to the tsunami waves in the far field to correct the lag of the arrival time and change of polarity) together with geodetic data of coseismic deformation of 13 GPS stations. They obtained a moment magnitude of Mw 8.0 [Gus15].

In this research, interseismic velocity vectors and coseismic displacements were calculated from time series of 20 GPS stations (of 3 components) and one time series of tsunami. Then, we conducted the joint inversion of coseismic displacements and 4 tsunami waveforms of the DART buoys, to obtain the slip distribution and the deformation field of the seismic source.

Seismotectonic setting of northern Chile

According to Barazangi and Isacks (1976), the northern region of Chile has a normal subduction type with a steeper dip of 25° - 30°, likewise to southern Peru region. The seismicity
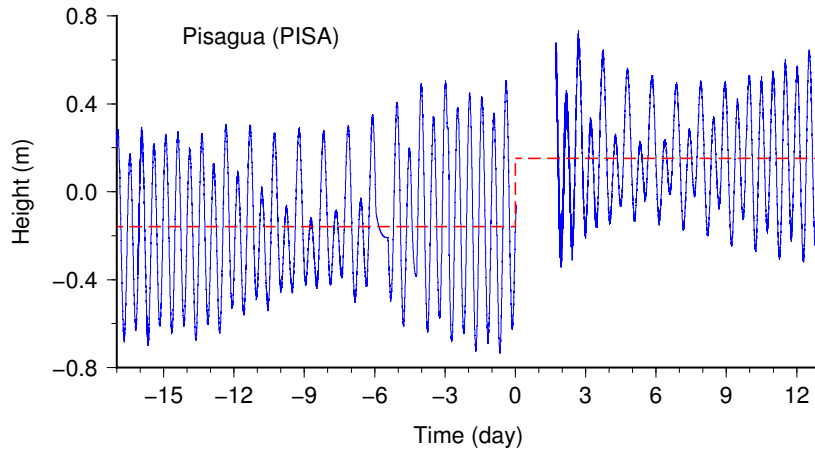
FIGURE 6.3: Time series of the Pisagua tidal station (PISA). The discontinuity of the mean sea level (vertical red line) after the event of April 01 was 30.9 cm, which represents the vertical coseismic displacement. The horizontal red line represents the mean sea level, before and after the mainshock. Data from Sea Level Station Monitoring Facility.

profile has a homogeneous slope from the trench to a depth around 300 km. Therefore, the Quaternary volcanoes are well developed in this region [Bar76].

The historical seismicity of northern Chile and southern Peru has been characterized by the occurrence of large earthquakes in the past (Dorbath et al., 1990 [Dor90]). According to Silgado (1978) [Sil78], the largest earthquakes reported in these areas date back to 1868 (south of Peru) and 1877 (north of Chile). Kausel (1986) [Kau86] estimated the magnitude of these events in the order of Mw 9.0. The seismic *gap* of northern Chile corresponds to the region between Arica to the north, including the rupture zone of the Tocopilla 2007 earthquake (Mw 7.7) to Antofagasta to the south. The rupture zone of the Tocopilla earthquake is confined only to the deepest sector of the contact zone between both plates, so that the contact segment located under the sea, towards the trench, was still before April 1, 2014 without seismically activating (Barrientos, 2014) [Bar14], so it is considered that the seismic *gap* of northern Chile would cover from Arica to Antofagasta (Figure 6.1).

In the south of Peru, after the earthquake of Camaná 2001 (Mw 8.4) the seismic *gap* of southern Peru would be reduced to the region between Ilo and Arica, with 150 km in length, while the Arica-Antofagasta seismic *gap* would have a length of more than 500 km.

For a gross estimation, considering that the interface does not necessarily retain the total convergence due to the subduction between the Nazca and South American plates, the equivalent accumulated displacements reach: (2014-1877 = 137 years)×6.5 cm/year, that is, approximately 9 m. Therefore, since the occurrence of the great earthquake in northern Chile in 1877 to the present, an equivalent displacement to approximately 9 m have been accumulated.

TABLE 6.1: Location of the geodetic and tide stations (Figure 6.4 and 6.5). PISA corresponds to the Pisagua tidal station. Δ represents the time window of the respective signal.

N	STN	Long (°)	Lati (°)	Z (m)	Δ (year)
01	AEDA	-70.1780	-20.5460	60.0	07.08
02	ATJN	-70.1370	-19.3010	1598.0	08.66
03	CGTC	-70.0690	-20.1770	1238.9	04.84
04	CHMZ	-69.1940	-19.6690	3784.0	06.95
05	CLLA	-69.3570	-20.9540	1554.8	06.07
06	COLC	-69.6390	-19.2760	3754.9	07.09
07	CRSC	-70.0800	-20.9180	1517.9	08.78
08	IAC1	-70.3330	-18.4800	46.0	02.81
09	IQQE	-70.1320	-20.2740	38.9	06.51
10	LTAC	-70.2770	-18.0510	482.8	03.51
11	LYAR	-70.5690	-18.1340	351.6	06.34
12	MNMI	-69.5960	-19.1310	2351.0	07.45
13	PCCL	-70.1070	-18.4580	1143.7	08.86
14	PCHA	-69.4320	-19.8690	1683.1	09.11
15	PICC	-69.3210	-20.4850	1373.0	07.81
17	PISA	-70.2160	-19.5970	04.3	00.09
16	PSGA	-70.1230	-19.5970	1002.0	07.50
18	PTRE	-69.5740	-18.1940	3607.7	10.11
19	TRTA	-70.0410	-17.4820	3201.8	05.69
20	UAPE	-70.1410	-20.2430	56.2	14.01
21	UTAR	-70.2170	-18.4910	87.7	07.60

Aftershocks of the 2014 Iquique earthquake that occurred within the first day after the mainshock are concentrated mostly between the trench to the coastline and between latitudes -19° to -20.8° approximately. The distribution of the aftershocks on the first day defines the geometry of the seismic source (Figure 6.1).

6.2 Acquisition of geodetic and tsunami data

Geodetic time series and calculation of interseismic velocity

The pre-processed time series of 20 continuous GPS geodetic stations located in northern Chile and southern Peru were used; while the time series of the Pisagua tide station (PISA) corresponds to the station closest to the epicenter.

The geodetic time series (Figure 6.2) for the 3 components: North, East and Vertical, with a sampling interval of 1 day have been processed by several research groups and are available on the network, for example:

FIGURE 6.4: Vector map of interseismic velocity with respect to the stable plate of South America (SOAM).

Geodetic Observatory of Nevada:

"http://geodesy.unr.edu/NGLStationPages/gpsnetmap/GPSNetMap.html"

GNSS Network of Chile (DT-INSU-France):

"https://gpscope.dt.insu.cnrs.fr/chantiers/chili"

Before performing the analysis of the geodetic time series, it should be verified that there is a good signal-to-noise ratio, this generally corresponds to the near-field GPS stations with respect to the seismic source. The geodetic time series in the international terrestrial reference frame ITRF2008 (Altamimi et al., 2011) [Alt11] were analyzed with the CATS software (Williams, 2008) [Wil08]. This software was used to clean the signal of the outliers, as well as to analyze the properties of the white noise, the seasonal components, the displacement or coseismic jump and the interseismic velocities using an algorithm for estimating maximum likelihood (D 'Agostino et al., 2008) [Dag08]. However, the CATS software algorithm overestimated coseismic displacement offsets, so we have implemented an algorithm to obtain these displacements.

The Table 6.1 shows the location of the selected stations as well as the time window of each signal. "The stations with an observation period greater than 3.0 years have been considered, except for the IAC1 station (with a time window of 2.8 years). Shorter intervals may result in biased estimates of linear interseismic velocities" (Blewitt and Lavalle, 2002) [Ble02].

To obtain the interseismic velocity, the numerical algorithm calculates the slope of a time window of the signal from the beginning of the series of time to the time of occurrence of the

TABLE 6.2: Location of the DART buoys, used in the inversion process.

N	Station	Long (°)	Lati (°)	Depth (m)
01	Dart 32412	-86.3740	-17.9840	4363
02	Dart 32401	-73.4290	-20.4730	4831
03	Dart 32402	-73.9830	-26.7430	4071
04	Dart 32413	-93.5170	-07.4060	4017

seismic event, without considering the coseismic or post-seismic component. This interseismic velocity is calculated with respect to the international terrestrial reference frame ITRF2008. To calculate the velocities relative to the South American stable plate (SOAM), an absolute rotation must be applied to the velocities with respect to the pole of the South American plate. The parameters of the pole of the SOAM plate of the ITRF2008 model are: latitude = -21.306°, longitude = -128.014° and angular velocity = 0.118°/million years.

The interseismic velocities and rotated velocities with respect to the SOAM pole are shown in Figure 6.4. It is observed that all directions of the velocities are coherent with the deformation pattern due to the convergence between the tectonic plates of Nazca and South America. The highest calculated horizontal interseismic velocity corresponds to the CRSC station with 29.23 mm/year.

Tsunami waveforms

The tsunami waveform of Pisagua station was obtained from the Sea Level Station Monitoring Facility (available at: http://www.ioc-sealevelmonitoring.org), for a 30-day time window. The sampling interval is 1 minute. The tidal station closest to the seismic source is Pisagua PISA (Figure 6.3).

Tsunami waveforms have been obtained from DART buoys, located on the high seas (Figure 6.1), (http://www.ndbc.noaa.gov/dart.shtml). The privileged location of these DART stations allows to obtain good results in the inversion process (as we will show later), since non-linear phenomena (such as coastal reflections and resonances) are minimized.

To remove the effects of the tide, a polynomial interpolation filter of 80 terms was applied to remove the very long period components (tides) and a lowpass filter constituted by the moving average of 3 consecutive samples of the signal to remove the components of short period (waves).

FIGURE 6.5: Vector map of observed coseismic displacement. The color scale indicates the vertical component of observed deformation.

6.3   Results and Discussion

Coseismic displacement calculation

The coseismic displacements were calculated using an algorithm implemented in Matlab and using the CATS software (Williams, 2008), which remove noise and seasonal variations, then an algorithm for estimating maximum likelihood was applied to finally calculate coseismic displacement. Figure 6.5 shows a map of the horizontal coseismic displacement vectors and Table 6.3 summarizes the calculated displacements. The maximum horizontal displacement was obtained at the GPS station of Pisagua: -278.76 mm (U_N) and -906.68 mm (U_E).

For the case of the tidal waveform, the differential vertical displacement was calculated by averaging the series before and after the seismic event, the result indicates a subsidence of 30.9 cm, which represents the maximum subsidence obtained within the overall stations (Figure 6.3). The difference between the vertical displacement of the geodetic station (-293.51 mm) and of the tide gauge (-309.0 mm) of Pisagua is due to the separation distance between the two stations, which is around 10 km. The mean sea level varies continuously, not only due to the effects of climate change, but also due to the continuous and slow tectonic deformation in the interseismic period and abruptly due to the occurrence of large-magnitude earthquakes, such as the 2014 Chile earthquake (Mw 8.1).

TABLE 6.3: Coseismic displacement for 3 components: North (U_N), East (U_E) and Vertical (U_Z) (Figure 6.5). PISA corresponds to the Pisagua tidal station, only the vertical component. σ represents the uncertainty of the displacement and is similar for the three components. NC: Not calculated.

Station	U_N (cm)	U_E (cm)	U_Z (cm)	σ (mm)
AEDA	-9.433	-38.982	5.768	0.08
ATJN	-31.219	-61.714	-18.504	0.11
CGTC	2.092	-62.339	-9.711	0.12
CHMZ	-6.684	-32.986	-1.573	0.12
CLLA	5.887	-11.674	-1.813	0.09
COLC	-6.192	-17.382	0.569	0.08
CRSC	-2.468	-11.895	-1.752	0.09
IAC1	-8.770	-8.243	-3.381	0.16
IQQE	-1.244	-28.431	-0.694	0.08
LTAC	-4.533	-3.359	-0.802	0.32
LYAR	-2.486	-2.120	-1.542	0.18
MNMI	-17.025	-33.362	-3.315	0.09
PCCL	-10.472	-9.862	-2.428	0.09
PCHA	-6.911	-45.847	-5.902	0.09
PICC	3.013	-29.561	-5.347	0.08
PISA	NC	NC	-30.900	NC
PSGA	-27.876	-90.668	-29.351	0.09
PTRE	-8.673	-7.593	0.079	0.07
UAPE	.313	-59.034	9.244	0.07
UTAR	-11.621	-9.594	-2.853	0.07
TRTA	-3.246	-1.260	-0.005	0.08

Fault plane parameterization

The rupture geometry of the seismic source was defined from the aftershocks distribution within the first day (Figure 6.1), which had dimensions of 180×120 km². This rupture geometry was divided into 24 subfaults (6 in the strike direction and 4 in the dip direction) of dimensions 30×30 km² each (Figure 6.6). The length of the subfault L must meet the condition: $h/L < 1/20$, where h is the average bathymetry depth in the fault plane region, in this case $h \sim 1.5$ km; therefore $L > 30$ km to meet the linear equations of shallow water theory (Satake, 1987) [Sat87].

The focal mechanism was obtained from the Global CMT catalogue (www.globalcmt.org) and corresponds to a thrust fault, the parameters are: strike = 355°, dip = 18° and rake angle = 109°. These parameters are the same for all subfaults. The depth of the hypocenter was set at 15 km.

TABLE 6.4: Velocity structure model of seismic waves in the neighbourhood of the source (northern Chile) [Lut00].

N	v_p (km/s)	v_s (km/s)	ρ (g/cm^3)	$Thickness$ (km)
01	4.00	2.30	2.50	01
02	6.05	3.48	2.91	08
03	6.28	3.61	2.96	13
04	6.39	3.67	2.98	10
05	6.51	3.74	3.00	35
06	7.60	4.37	3.22	23
07	8.10	4.66	3.32	60

Green functions calculation

To calculate the distribution of the seismic source it is necessary to calculate the Green functions, that is, the coseismic displacements generated in the location of the i-th geodetic station due to the unitary deformation of the j-th subfault:

$$G_{ij} \times m_j = d_i \tag{6.1}$$

where, "G_{ij} is the Green function of the i-th station generated by the j-th subfault, m_j is the dislocation or *slip* in the j-th subfault, d_i is the coseismic displacement observed in the i-th station". The coseismic deformation field was calculated based on the formulation of Wang et al. (2003) [Wan03] for an elastic medium, isotropic and stratified by velocity layers (Table 6.4).

The tsunami Green functions have been calculated for the DART buoys located offshore (Figure 6.1). The physical process is considered almost entirely linear. The synthetic tsunami waveforms have been calculated with the TUNAMI-F1 numerical model (Imamura et al., 2006) [Ima06], which has been modified according to our input and output file formats. The initial condition was obtained from the formulation of Wang et al. (2003), for an elastic, linear and stratified medium.

Inversion model

The inversion process was conducted using the "non-negative least squares method. This iterative method compares the simulated and observed data until the square of the difference is minimal under the condition that the dislocation or *slip* is positive $m_j > 0$" (Lawson and Hanson, 1974) [Law74].

$$|G_{ij}m_j - d_i|^2 \to 0 \tag{6.2}$$
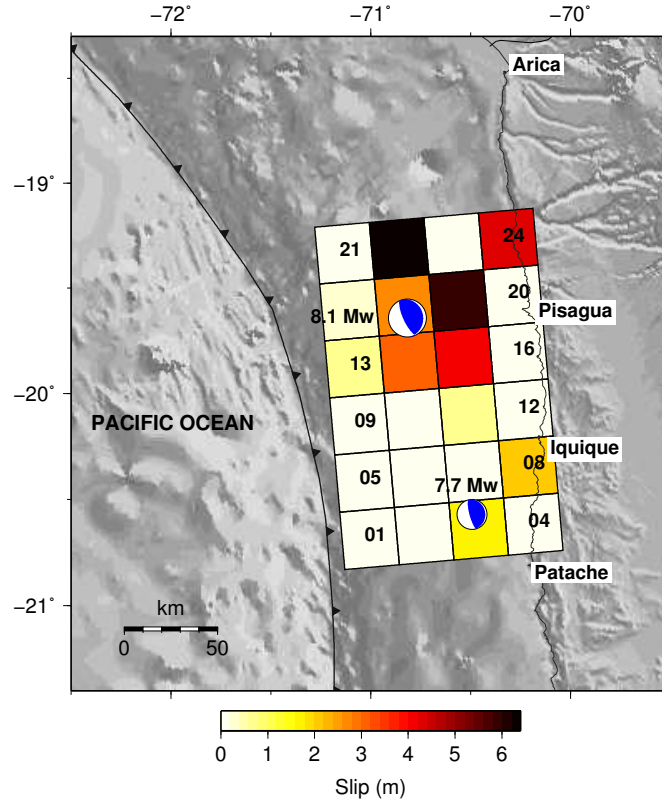
FIGURE 6.6: Distribution of the seismic source (slip). The focal diagrams represent the mainshock of Mw 8.1 and the largest aftershock of Mw 7.7.

Table 6.3 shows that there are 61 geodetic data (20 U_N, 20 U_E and 21 U_Z). Furthermore, 4 tsunami waveforms, totaling 380 data, to solve the system of equations given by the equation 6.1, so there is an overdetermined system, that is, the number of data is greater than the number of equations.

The normalized variance (or error) is defined in the equation 6.3:

$$Var = \frac{\sum_{i=1}^{N_i} \sum_{j=1}^{N_j} [G_{ij}m_j - d_i]^2}{\sum_{i=1}^{N_i} (d_i)^2} \qquad (6.3)$$

Where N_i is the data number ($N_i = 380$) and N_j is the number of unknowns or subfaults ($N_j = 24$). The smaller the value of the normalized or residual variance, the better the correlation between observed and simulated data. The normalized variance of the inversion was 0.10. The errors for each dislocation value, have been calculated using the methodology known as "delete half jack knife", by Tichelaar and Ruff (1989) [Tic89].

The results (Table 6.5) show that the maximum dislocation or *slip* was 6.22 m and the scalar seismic moment obtained was 1.57×10^{21} Nm. The corresponding magnitude was Mw 8.1, a value similar to that obtained by inversion of teleseismic waves.

TABLE 6.5: Distribution of coseismic displacement (*slip*). The depth H corresponds to the upper side of the subfault.

N	Longitude (°)	Latitude (°)	Slip (m)	H (km)
1	-71.1300	-20.8300	0.00 ± 0.00	6.718
2	-70.8569	-20.8075	0.01 ± 0.02	15.988
3	-70.5838	-20.7851	1.69 ± 0.79	25.259
4	-70.3107	-20.7626	0.00 ± 0.81	34.530
5	-71.1551	-20.5600	0.00 ± 0.01	6.718
6	-70.8820	-20.5376	0.00 ± 0.00	15.988
7	-70.6089	-20.5151	0.00 ± 0.00	25.259
8	-70.3358	-20.4926	2.16 ± 0.89	34.530
9	-71.1802	-20.2900	0.00 ± 0.14	6.718
10	-70.9071	-20.2676	0.00 ± 0.21	15.988
11	-70.6340	-20.2451	0.64 ± 0.36	25.259
12	-70.3609	-20.2227	0.00 ± 0.98	34.530
13	-71.2054	-20.0201	0.61 ± 0.31	6.718
14	-70.9323	-19.9976	3.07 ± 1.77	15.988
15	-70.6591	-19.9751	4.07 ± 2.27	25.259
16	-70.3860	-19.9527	0.00 ± 0.07	34.530
17	-71.2305	-19.7501	0.27 ± 0.12	6.718
18	-70.9574	-19.7276	2.75 ± 1.26	15.988
19	-70.6843	-19.7052	5.85 ± 3.42	25.259
20	-70.4112	-19.6827	0.00 ± 0.05	34.530
21	-71.2556	-19.4801	0.00 ± 0.07	6.718
22	-70.9825	-19.4576	6.22 ± 2.24	15.988
23	-70.7094	-19.4352	0.00 ± 0.45	25.259
24	-70.4363	-19.4127	4.35 ± 2.10	34.530

TABLE 6.6: Correlation coefficients between the observed and simulated tsunami waveforms of the 2014 Chile earthquake. The time window is counted from the initial arrival time.

N	Station	Time window (min)	Correlation
1	DART 32412	94	0.93
2	DART 32401	94	0.96
3	DART 32402	94	0.92
4	DART 32413	94	0.85

The maximum vertical coseismic displacement (*uplift*) calculated was 0.95 m and the maximum coseismic subsidence was 0.32 m (Figure 6.7).

Figure 6.8 shows the comparison between the observed and simulated tsunami waveforms from the offshore DART bouys. Table 6.6 shows the correlation coefficients between the observed and simulated tsunami waveforms, the best correlation is for DART32401 buoy with a value of 0.96.
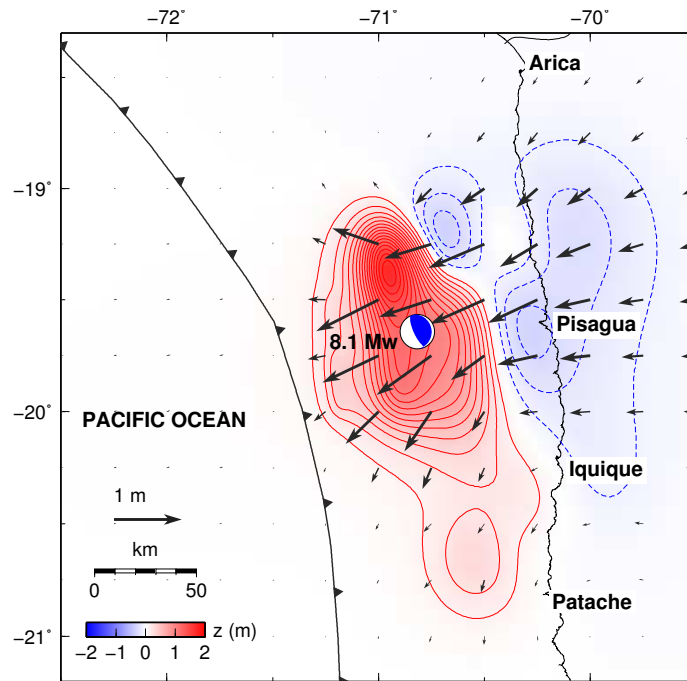
FIGURE 6.7: Coseismic deformation field, the red colour indicates the uplift and the blue colour indicates the subsidence. The arrows represent the horizontal displacement components. The interval of the deformation level curves correspond to 0.1 m. The focal diagram represents the mainshock.
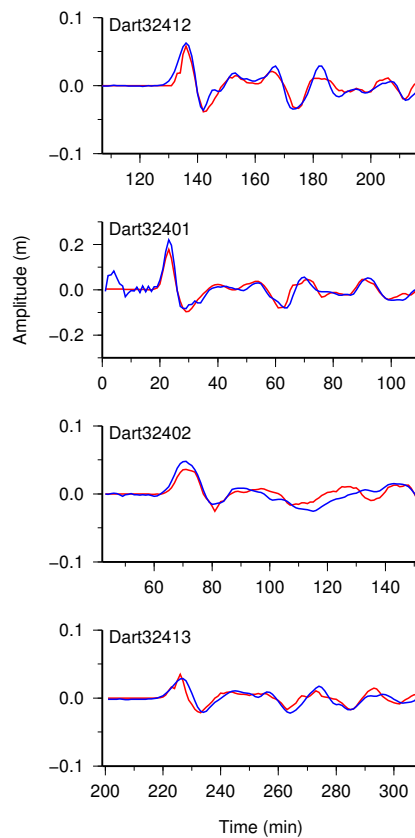
FIGURE 6.8: Comparison of observed tsunami waveforms (blue) and synthetic waves (red). A good correlation is observed, even after several periods.

Comparison with another results

Barrientos and Ward (1990) made the inversion of surface deformation in the coast to calculate the distribution of the displacement (*slip*) of the 1960 Chile earthquake and obtained an underestimated geodetic moment which was only one fifth of the seismic moment; it was speculated that the explanation of this discrepancy was due to the coastal geodetic data is insensitive to dislocation generated near the marine trench [Bar90].

According to the results (Figure 6.6), 2 main asperities are observed in the strike direction separated by a distance of around 100 km. The larger asperity is located near the epicenter in the northern side of the rupture geometry and the smaller one is located in the southern side of the fault plane. Seismic inversion models (Lay et al., 2014) underestimate the amplitude of the second asperity (to the south), probably due to the presence of a strong component of seismic displacement in this area (recordable by GPS geodetic stations but not registrable by the seismic stations) [Lay14].

Our results are very close to those of An et al., (2014) [Anc14]; however, they do not resolve the small asperity located in the southern side of the rupture geometry (Figure 6.6, Figure 6.7). This fact may be due to they are considering only 3 DART bouys (in this research we are considering 4 DART buoys plus 20 geodetic stations) and they take into account only the first period of the tsunami waveform in the inversion process, while we are taking a window time of 2 periods. Furthermore, they considered a subfault size of 20×20 km^2, while we are considering a dimension of 30×30 km^2, according to the condition of linearity of shallow water theory.

6.4 Conclusions

After the seismic event there was a permanent subsidence on the northern coast of Chile, in the region of the seismic source. The Pisagua GPS station recorded a subsidence of 29.4 cm while the Pisagua tide gauge recorded a subsidence of 30.9 cm (both stations are separated by 10 km distance).

The mean sea level varies continuously, not only due to the effects of climate change, but also due to the continuous and slow tectonic deformation in the interseismic period and abruptly due to the occurrence of large magnitude earthquakes with rupture area in the sea or close to the coastline.

The seismic source of the 2014 Chile earthquake is of a complex nature with 2 main asperities located to the north and south of the rupture geometry, separated by an average distance of 100 km. The larger asperity is located around the epicenter offshore the port of Pisagua.

From the results of the coseismic displacements and interseismic velocities, it is observed that the coseismic displacement vectors have opposite directions to the interseismic velocity vectors, thus verifying the elastic rebound theory, after the occurrence of a large magnitude earthquake, such as the 2014 Chile earthquake (Mw 8.1).

From the analysis of the geodetic time series, it can be deduced that most of the horizontal displacement vectors converge toward the region of the closest asperity, in the case of a multiple or composite seismic source.

The inversion model estimates the value of the scalar seismic moment at 1.57×10^{21} Nm, a value similar to that obtained by inversion of teleseismic waves. The equivalent moment magnitude is Mw 8.1.

The seismic *gap* of Arica-Antofagasta still maintains a high potential for seismic energy, since the occurrence of the 2014 Chile earthquake has only fractured no more than 25% of the total dimensions of the seismic *gap* area.

Chapter 7

Numerical procedure to forecast the tsunami parametes from a database of pre-simulated seismic unit sources

We have implemented a numerical procedure to forecast the parameters of a tsunami, such as the arrival time of the front of the first wave and the maximum wave height in real and virtual tidal stations along the Peruvian coast, with this purpose a database of pre-computed synthetic tsunami waveforms (or Green functions) was obtained from numerical simulation of seismic unit sources (dimension: 50×50 km^2) for subduction zones from southern Chile to northern Mexico. A bathymetry resolution of 30 arc-second (approximately 927 m) was used. The resulting tsunami waveform is obtained from the superposition of synthetic waveforms corresponding to several seismic unit sources contained within the tsunami source geometry. The numerical procedure was applied to the Chilean tsunami of April 1, 2014; in the case of the Arica tide station an error (from the maximum height of the observed and simulated waveform) of 3.5% was obtained, for Callao station the error was 12% and the largest error was in Chimbote with 53.5%. The aim of the present research is tsunami early warning, where speed is required rather than accuracy. Based on our results, we state an accuracy within 15% of error (Jiménez et al., 2018) [Jim18].

7.1   Introduction

According to historical seismicity (Silgado, 1978 [Sil78]; Beck and Nishenko, 1990 [Bec90]), many destructive earthquakes have occurred in Peru. Some of which have generated tsunamis that have affected ports and coastal towns, for instance, the remarkable tsunami of Callao 1746 in central Peru (Dorbath et al., 1990; Jiménez et al., 2013; Mas et al., 2014 a) and the tsunami of southern Peru in 1868, both megathrust earthquakes with a magnitude around Mw 9.0. In the 20th century, there were the tsunamigenic earthquakes of 1960 in Lambayeque (Mw 7.6), 1966 in northern Lima (Mw 8.1), 1974 in southern Lima (Mw 8.1) (Beck and Ruff, 1989), 1996 in Chimbote (Mw 7.5) and 1996 in Nazca (Mw 7.7). According to instrumental seismicity (after 1960), only in the 21st century there have been two major tsunamigenic earthquakes in Peru: Camana in 2001 (Mw 8.4) (Adriano et al., 2016) and Pisco in 2007 (Mw 8.1) (Jimenez et al., 2014) [Jim14]. Accordingly, regarding tsunami hazard, the main issue in Peru is the near field tsunami event, where the tsunami arrival time is in the range of 15 min to 60 min (Mas et al., 2014 b). Therefore, it is necessary to develop a system to forecast, in the shortest possible time, the tsunami parameters from a database of pre-simulated seismic unit sources.

The Centro Nacional de Alerta de Tsunamis from Peru (CNAT in Spanish, corresponding to Peruvian Tsunami Warning Center) is the official representative to international institutions such as the Pacific Tsunami Warning Center (PTWC), responsible for issuing information bulletins, alert or alarm in case of occurrence of tsunamis for near-field or far-field origin. For near field events, it is not convenient to compute a numerical tsunami simulation immediately after the occurrence of an earthquake because this process may take several hours and the arrival time is in order of the minutes. For this purpose, it is required to process quickly and accurately the seismic information (hypocenter location and magnitude) provided by the Instituto Geofísico del Perú (IGP) for earthquakes generated in the near field (local) or by USGS (United States Geological Survey) for earthquakes generated in the far field. To accelerate the processing of information is necessary to implement some numerical procedure to process such information automatically from a database of pre-computed tsunami scenarios.

State of the knowlegde on tsunami forecasting

As research antecedents, Gica et al. (2008), implemented a database of pre-calculated seismic events to forecast tsunami parameters (arrival time, maximum tsunami height) with seismic unit sources of 50×100 km^2 using a bathymetry of 4 arc-minute resolution. This system is used by the National Oceanic and Atmospheric Administration (NOAA) and this pre-computed database serves as input to an intermediate resolution model along the coast [Gic08]. On the other hand, Greenslade et al. (2011) implemented a model to forecast

tsunamis from a database of seismic scenarios, which is used by the Tsunami Warning Center in Australia for buoys at off-shore (not for tidal gauges on the coast), the bathymetry resolution is 4 arc-minute and the size of the seismic source is $100{\times}100$ km^2 [Gre11].

Jiménez (2010), presented a numerical procedure to determine the occurrence of tsunamis based on hypocentral parameters and magnitude. Also, an algorithm to calculate quickly the arrival time of the first tsunami wave (based on a linear trajectory followed by the tsunami wave according to actual bathymetry) was implemented. That research was the starting point for the next step: the calculation of the tsunami wave height from tsunami numerical modeling [Jim10].

In this chapter, the results of Jiménez (2010) are extended to calculate the arrival time of the front of the first tsunami wave and the maximum wave height (of the whole computation time) for real and virtual coastal tide gauge stations. This is based on a database or catalogue of synthetic tsunami waveforms (or Green functions) obtained by tsunami numerical simulation of unitary seismic sources of dimensions $50{\times}50$ km^2, unitary dislocation with a focal mechanism based on Global Centroid Moment Tensor (CMT) catalogue and a 5 km depth for the shallower end of the sub-fault that is near the trench. The bathymetry has a grid resolution of 30 arc-secs (approximately 927 m). Hence, this paper covers important and interesting work being undertaken to develop a tsunami scenario database for Peru. It will provide a tool that can be used to determine if tsunami warnings are needed for parts of the Peruvian coastline.

7.2 Data Acquisition

Bathymetry data

The tsunami wave speed and directivity depend on bathymetry; therefore, a good description of bathymetry is important to conduct numerical simulation of propagation of tsunamis. The global bathymetry model is taken from GEBCO 30 (2016), which has a grid resolution of 30 arc-second or approximately 927 m. The fine bathymetry in coastal zones has been updated from marine soundings provided by the Directorate of Hydrography and Navigation (DHN) of the Peruvian Navy. Figure 7.1 shows the bathymetry of the whole Pacific Ocean, the seismicity for 2015 and the principal subduction zones.

Focal mechanism parameters and seismicity

The focal mechanism parameters (azimuthal or strike angle θ, dip angle δ, and rake angle λ) are taken from historical averages of the catalogue of the Global Centroid Moment Tensor
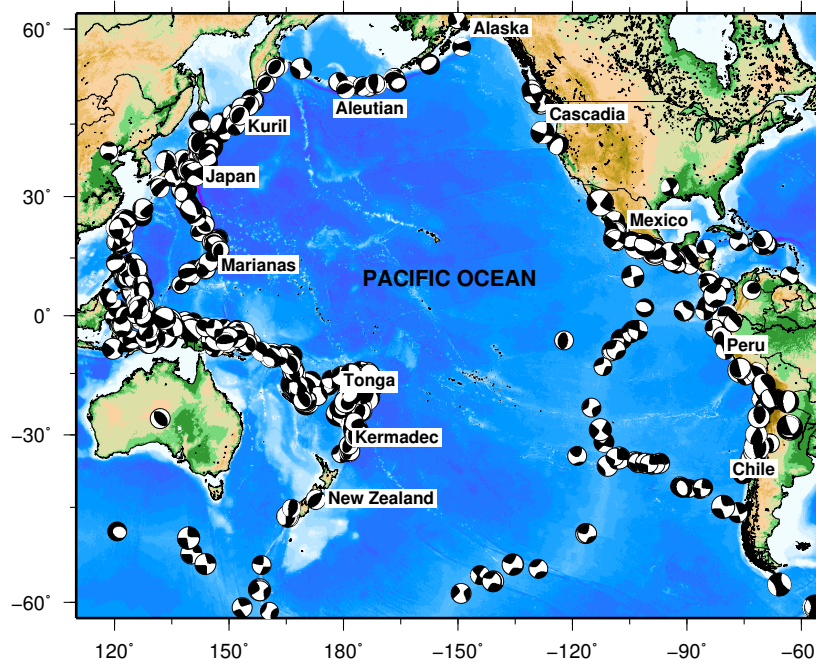
FIGURE 7.1: Bathymetry of the Pacific Ocean from GEBCO model. The focal mechanism of seismic events of 2015 are represented by circles (Mw > 5.0) from Global CMT catalogue. The principal subduction zones are represented by tags.

(CMT) for a given subduction zone, (http://www.globalcmt.org, last accessed: December 2015). In some cases, the strike angle is taken according to the orientation of the trench or parallel to the coast, also the rake or dislocation angle is taken as 90° to obtain a maximum vertical seafloor deformation. The upper side depth of the subfault near the trench is taken as 5 km; according to dip angle, the intermediate depth subfault is set to 17–21 km and the depth of the subfault close to coast is around 30 km.

To define the computational grid, it is necessary to know the location of the subduction zones in the Pacific Ocean. From seismicity data and focal mechanism parameters is possible to deduce the seismic subduction zones along the Pacific Ocean. These subduction zones contain: Chile, Peru to Central America up to northern Mexico, Cascadia zone, Alaska, Aleutians islands, Kuril Islands, Japan, Marianas trench, Tonga and Kermadec (Figure 7.1).

7.3 Methodology

The methodology could be summarized in the following form: First, the coseismic deformation must be calculated and used as the initial condition for the tsunami wave propagation. Later, a database or catalogue of synthetic tsunami waveforms was implemented from tsunami numerical simulation of unitary seismic sources.
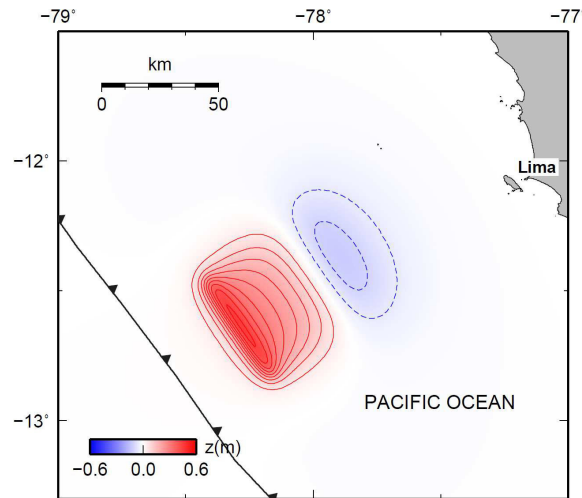
FIGURE 7.2: Vertical coseismic deformation field of a seismic unit source located offshore Lima. The red colour represents the uplift and blue colour represents subsidence. The barbed lines represents the Peruvian trench.

Coseismic deformation

The initial condition for tsunami propagation is calculated using the deformation model of Okada (1992) for an elastic, homogeneous and isotropic semi-infinite medium [Oka92]. Seismic sources are considered of dimensions $50{\times}50$ km^2, unitary dislocation (slip $= 1$ m) and depth of the upper side of the shallower unit source is 5 km; the depths of the deeper unit sources will depend on the dip angle and the width (50 km, in this case) of the unit source. The focal mechanism parameters are taken from the mean values of the CMT catalogue and the seismicity of the corresponding subduction zone (from southern Chile to northern Mexico).

We assume that the generation of coseismic deformation of the seafloor produces an immediate and identical deformation on the ocean surface (due to the incompressibility of the fluid). As the ocean is a fluid, the deformation does not hold its shape and the initial displacement radiates away from the source creating a tsunami wave that propagates in all directions (Okal, 2009) [Oka09]. Figure 7.2 shows an example of deformation field.

Tsunami numerical modeling

A modified version of TUNAMI-F1 (IOC, 1997) numerical model was used. This code was written in Fortran. The algorithm corresponds to a linear model in a regular grid-system using spherical coordinates based on shallow water theory. The differential equations (linear momentum conservation and mass conservation or continuity equation) are integrated numerically using the method of leap frog in a finite differences scheme. A numerical stability condition (CFL condition) of less than 0.8 was used to avoid numerical instabilities.

The initial conditions are based on the deformation theory by Okada (1992) [Oka92]. The boundary conditions along the coastline (for the linear model) represent a vertical wall, so we suggest the use of a correction factor for the synthetic tsunami waveform of each tidal station (to approximate a nonlinear system).

The numerical code is written in Fortran and runs in a Linux system. The digital processing of input data and output results were made in Matlab. The graphical user interface (GUI) was implemented also in Matlab. The final application runs under Windows or Linux.

Unitary seismic sources and Green functions

The set of unitary seismic sources and tsunami waveforms form the database of the model. The number of unitary seismic sources is proportional to the geographical extent of the database. Therefore, the chances of predicting the tsunami parameters of an earthquake generated somewhere in the Pacific Ocean will be greater.

Taking into account the seismicity of the Peruvian coast and adjacent countries, the computational domain was initially chosen from Antofagasta (Chile) to Ecuador. For the first stage, this area has been divided into 130 unitary seismic sources of dimensions 50×50 km^2. The idea is to simulate the propagation of tsunami waveforms for each seismic unit source and calculate the Green functions $G(t)$ or synthetic mareograms at each port and coastal town in Peru, where real and virtual tide gauge stations have been selected. Currently and in a second stage, 465 seismic unit sources have been modeled, from southern Chile to northern Mexico.

Virtual tidal stations

There are 17 numerical tide gauge station within the computational area, many of them correspond with the actual location of real tidal stations. These virtual stations correspond to ports and coastal towns (Figure 8.2). The geographical coordinates and the empirical correction factor of each station are shown in Table 7.1.

A major aspect of the database is the development of correction factors for each individual tidal station. These correction factors account for the amplification or attenuation of the tsunami waves in shallow waters due to non linear processes that cannot be simulated by using linear model. These correction factors are determined in an empirical way as the rate of the maximum observed tsunami height over the maximum simulated tsunami height.

TABLE 7.1: Virtual and real tide stations used in the numerical calculation. The parameter K_i represents the empirical correction factor to take into account the linearity.

N	Station	Latitude (°)	Longitude (°)	K_i
1	Arica	-18.4758	-70.3232	0.700
2	Ilo	-17.6445	-71.3486	0.790
3	Matarani	-17.0009	-72.1088	0.800
4	Camaná	-16.6604	-72.6838	0.400
5	Atico	-16.2311	-73.6944	1.000
6	San Juan	-15.3556	-75.1603	0.600
7	Pisco	-13.8061	-76.2919	0.650
8	Cerro Azul	-13.0253	-76.4808	0.820
9	Callao	-12.0689	-77.1667	0.800
10	Huacho	-11.1218	-77.6162	0.950
11	Huarmey	-10.0718	-78.1616	1.050
12	Chimbote	-09.0763	-78.6128	0.460
13	Salaverry	-08.2279	-78.9818	0.700
14	Pimentel	-06.8396	-79.9423	0.750
15	Paita	-05.0837	-81.1077	0.940
16	Talara	-04.5751	-81.2827	0.880
17	La Cruz	-03.6337	-80.5876	0.740
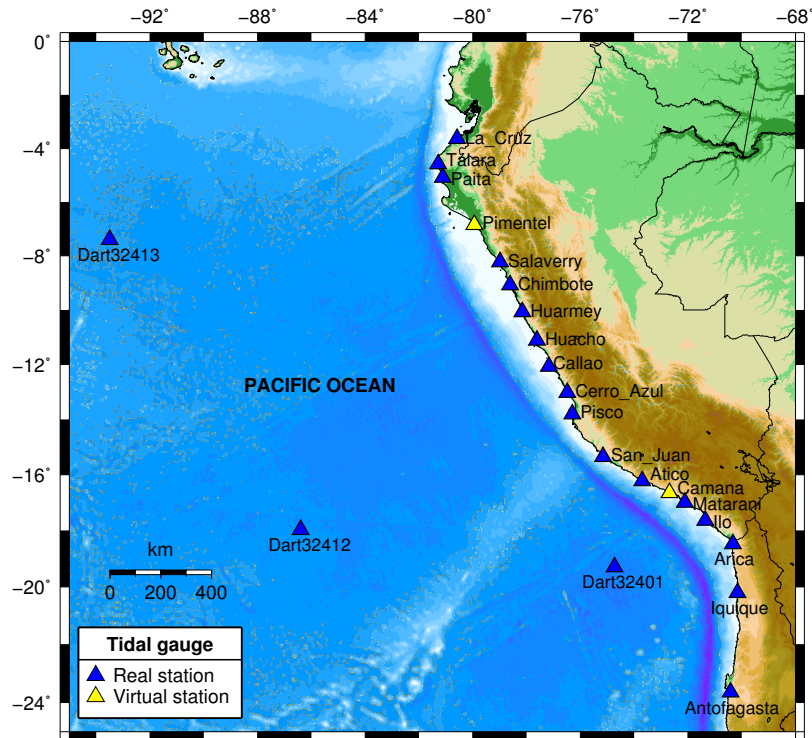
FIGURE 7.3: Location of virtual and real tide gauge station to be considered in the numerical simulation.

Governing equations of the numerical model

All the equations are highly dependent on earthquake magnitude Mw and epicenter location. According to scaling laws between the dimensions of a fault plane or seismic source (of rectangular geometry) and the magnitude of the earthquake for subduction zones (Papazachos, et al., 2004), we have the basic empirical relations [Pap04]:

$$log10(L) = 0.55Mw - 2.19 \tag{7.1}$$

$$log10(W) = 0.31Mw - 0.63 \tag{7.2}$$

Where L is the length (in km) of the seismic source, W is the width (in km) of the seismic source, Mw is the moment magnitude (Mw). The seismic moment defined by (Aki, 1966) [Aki66], is:

$$M_0 = \mu L W D \tag{7.3}$$

Where μ is the mean rigidity modulus (4×10^{10} N/m^2) of the rupture zone and D is the dislocation or slip of the seismic source. The relationship between seismic moment (in Nm) and the moment magnitude is given by the relation:

$$log10(M_0) = 1.5Mw + 9.1 \tag{7.4}$$

The model output (tsunami waveform) is the linear combination of the synthetic tsunami waveforms or Green functions $G(t)$ corresponding to the seismic unit sources contained in the rupture geometry (Figure 7.4). The number of seismic unit sources is given by:

$$N = \frac{LW}{L_0 W_0} \tag{7.5}$$

Where L_0=50 km, W_0=50 km, corresponding to the dimensions of the unitary seismic source. Therefore, for an earthquake of Mw 7.0 only one seismic source is required; but for an earthquake of Mw 8.0, 5 seismic sources are required (Table 7.2). The criterion in selecting the deeper or shallower unit seismic source is based on an algorithm that takes into account the nearest distance from the epicenter. Also, an amplification factor is required: the dislocation or mean slip D. To linearize the model, an empirical correction factor K_i for each coastal tidal station is required. The signal of the tsunami $f_i(t)$ in i-th tidal station is given by:
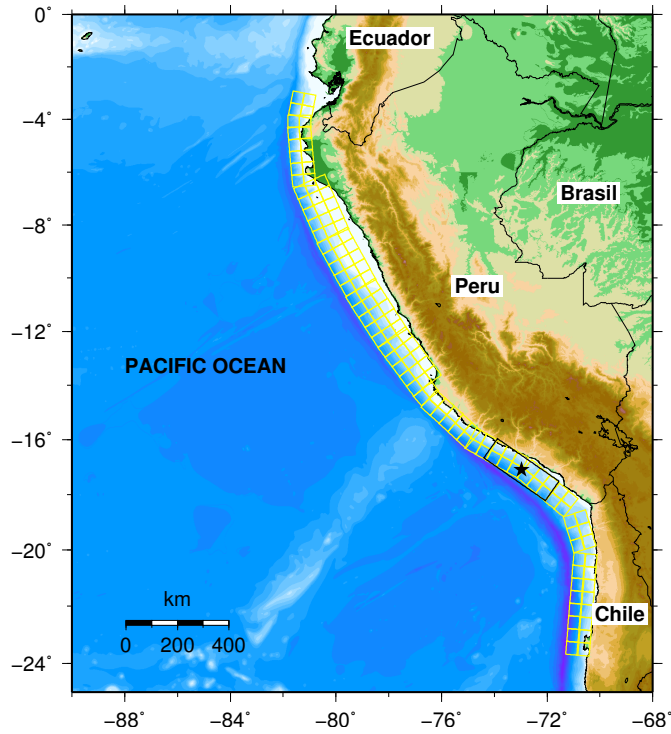
FIGURE 7.4: Location of unit seismic sources and an example of a major earthquake (black rectangle). The black star represents the epicentroid (gravity center of the seismic source).

TABLE 7.2: Number of unit sources N required by the fault plane geometry, according to the magnitude of the earthquake.

Magnitude (Mw)	N
7.0	1
7.5	2
8.0	5
8.5	12
9.0	32

$$f_i(t) = DK_i \sum_{j=1}^{N} G_{ij}(t) \tag{7.6}$$

Where D is the mean slip, K_i is the correction factor according to Table 7.1 and $G_{ij}(t)$ is the Green function (synthetic or simulated tsunami waveform) for the i-th tidal station due to the j-th seismic unit source.
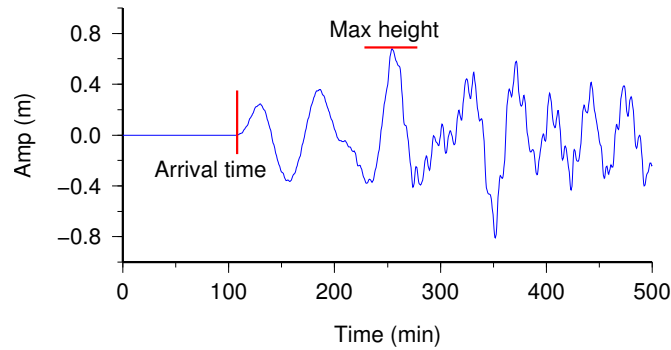
FIGURE 7.5: A synthetic tsunami waveform. The horizontal red line represents the maximum tsunami height and the vertical red line, the arrival time.

7.4   Results and Discussion

Graphical User Interface: "Pre-Tsunami"

With the information of hypocentral parameters, conditions of tsunami generation and algorithm of precomputed seismic unit sources, we have implemented an application with a graphical user interface developed in Matlab programming language. The input data are the hypocentral parameters: magnitude Mw, hypocentral depth (this is used for discriminating the sources greater than 60 km depth), geographical latitude and longitude of the epicenter and origin time. The outputs are the parameters of seismic source geometry and a diagram of the likely rupture geometry on a map.

The subroutine Arrival Time calculates the arrival times from the dependence of wave velocity with respect to the bathymetry. The subroutine Catalogue calculates the arrival time of the front of the first wave and the maximum wave height of the tsunami (Figure 7.5) in ports and coastal towns of Peru, from a database of synthetic tsunami waveforms or Green functions. The time of calculation is very fast, in the order of a few seconds due to the pre-calculated synthetic tsunami waveforms.

The subroutine Automatic IGP loads the hypocentral parameters from the web site of the seismological service of IGP (Instituto Geofísico del Perú, in spanish), to avoid the manual introduction of these parameters in the case of some big earthquake in the near field reported by the Peruvian seismological service of IGP.

The graphical user interface of Pre-Tsunami application is quite friendly and easy to use by the operator of the tsunami warning and constitutes an important computational tool to forecast and decision making for issuing bulletins, alert or alarm in case of occurrence of tsunamis. The last version (V4.6) was updated in August 2016 (Figure 7.6).
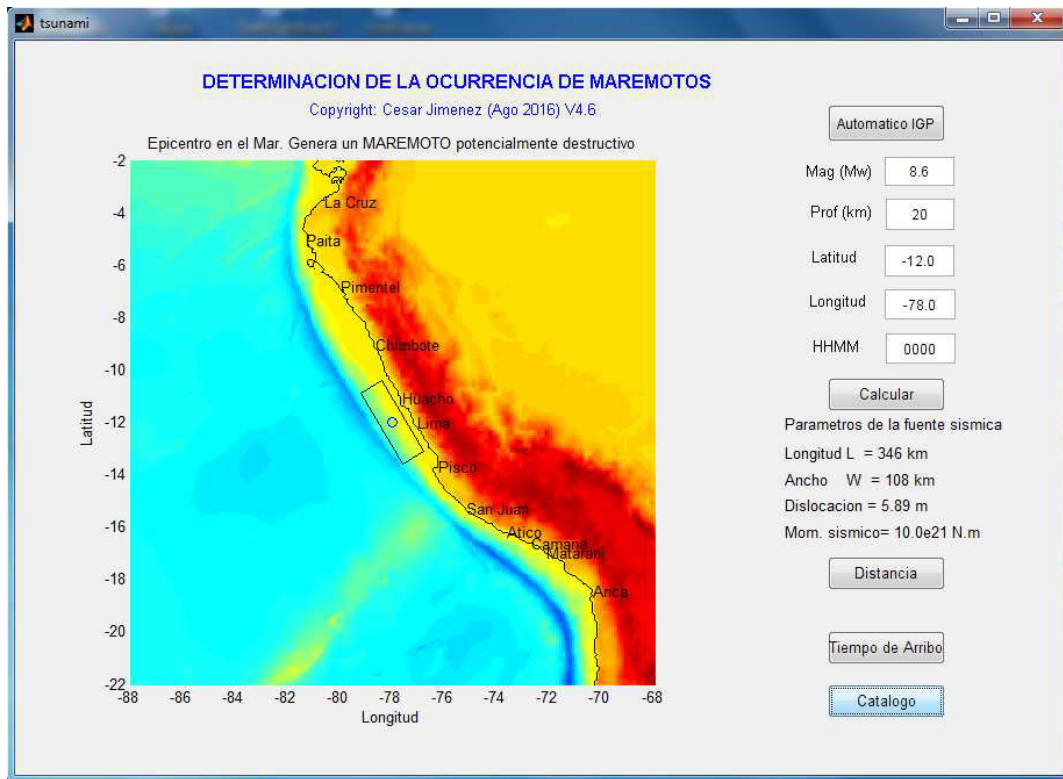
FIGURE 7.6: The "Pre-Tsunami" Graphical User Interface (Version 4.6).

Output of the application Pre-Tsunami

The output of the model will be useful to forecast tsunamis in the near, regional and far field. The output parameters are: the arrival time of the front of the first wave and the maximum height of the tsunami wave. These results will be useful for issuing the alert or alarm of the tsunami. For example, for a hypothetical Mw 8.6 magnitude earthquake with epicenter offshore of Lima (Lat = -12.00°, Lon = -78.00°, Depth = 20 km, origin time: 00:00), according to the threshold of tsunami heights of PTWC, maximum evacuation ($H_{max} > 3$ m) would be declared for Huacho, Callao and Cerro Azul (Table 7.3).

Application to the tsunami of Chile 2014 (Mw 8.2: USGS preliminary report)

A big earthquake and tsunami was generated in Iquique Chile on 01 April 2014 (Lay et al., 2014; An et al., 2014). The hypocentral parameters (longitude, latitude, depth and origin time) reported by NEIC-USGS (http://earthquake.usgs.gov/earthquakes/map) were: lon=-70.817°, lat=-19.642°, z=25 km, origin time: 23:46:46 UTC.

The acquisition of data from the National Tide Gauge Network of Peru (www.dhn.mil.pe) and Arica Station (tide gauge from Chilean network: http://www.ioc-sealevelmonitoring.

TABLE 7.3: Results of the numerical model: arrival time T_A and maximum tsunami height Hmax. Region: Northern (Nor), Central (Cen) and Southern (Sou).

Port	Zone	T_A	H_{max} (m)
La_Cruz	Nor	01:54	0.74
Talara	Nor	01:05	0.26
Paita	Nor	01:15	0.12
Pimentel	Nor	01:42	0.52
Salaverry	Nor	01:34	2.70
Chimbote	Cen	01:11	1.39
Huarmey	Cen	00:22	2.32
Huacho	Cen	00:20	3.41
Callao	Cen	00:24	6.75
Cerro_Azul	Cen	00:37	3.35
Pisco	Cen	00:40	2.10
San_Juan	Cen	00:43	0.91
Atico	Sou	00:55	0.28
Camaná	Sou	01:15	0.28
Matarani	Sou	01:09	0.18
Ilo	Sou	01:22	0.40
Arica	Sou	01:39	0.59

org) was performed. Digital signal processing was performed for these signals; a highpass Butterworth filter with cut frequency: $fc = 6.94 \times 10^{-5}$ Hz and a lowpass filter (fc = 0.0083 Hz) was applied to remove components of long period (tides) and short period (surges); so, the maximum amplitude of the tsunami wave was calculated (Table 7.4). The calculation of the parameters of the simulated tsunami was conducted using the Pre-Tsunami application (version 4.6). This event has allowed calibrating the values of the correction factor K_i for each station.

The results show a good correlation within the margins of error (15%), except for Pisco and Chimbote stations. For the case of Arica station, the error was of 3.5% and Ilo's error was 5.7%. In the case of Callao station, the error was 12% and the largest error was in Chimbote with 53.5%. This does not mean that the method presented is flawed and not useful, rather it shows the limitations of the method. With additional data from DART buoys and future tsunamis, updating and calibration of Pre-Tsunami application will be performed (i.e., the empirical correction factors of each tidal station), achieving on the future a greater reliability.

Projection of the catalog of seismic unit sources

The current addition in the database of the simulation is shown in Figure 7.7, geographically, from southern Chile to northern Mexico with 465 seismic unit sources simulated. We hope to conduct the simulation of seismic unit sources for the entire Pacific Ocean corresponding

TABLE 7.4: Comparison of the observed and simulated maximum tsunami wave heights at gauge sites for Chilean earthquake and tsunami of 01 April 2014. Negative values (-) indicate underestimation.

Station	Observed (m)	Simulated (m)	Error (%)
Arica	2.00	2.07	03.5
Ilo	1.05	1.11	05.7
Matarani	0.52	0.60	15.4
San_Juan	0.45	0.51	13.3
Pisco	0.23	0.31	34.8
Callao	0.25	0.28	12.0
Chimbote	0.15	0.23	53.5
Salaverry	0.20	0.18	(-)10.0
Paita	0.10	0.11	10.0

to subduction zones of Pacific Seismic Ring. This implies a large computational effort with the simulation of more than 1000 seismic unit sources, for a computational grid around the Pacific Ocean with 30 arc-sec resolution or 1 min resolution for the far field.

The Directorate of Hydrography and Navigation (DHN) of the Peruvian Navy have acquired, at beginning of 2016, a high-performance computer or cluster with 32 cores or processors for scientific numerical calculations to conduct these tsunami numerical simulations. The computation time will be considerably reduced with the use of this high performance computer: each seismic unit source simulation is computed in approximately 30 minutes for a computational grid of 3720×5760 elements, while this very computation lasted more than 3 hours in a personal computer with microprocessor i7 of 3.40 GHz.

In the future, we expect to conduct the inversion of tsunami waveforms to obtain the distribution of the seismic source.

Limitations of the model

A linear model is used to simulate a nonlinear phenomenon, for this reason we suggest the use of an empirical correction factor for each tidal station. This correction factor must be calibrated with every new tsunami event.

The model is strongly dependent on the seismic magnitude and epicenter location. In addition, the model takes the mean values of the focal mechanism CMT catalogue, if the variation of focal mechanism is great, the forecast will not be very good.

In most of the cases, if the epicenter does not match with the epicentroid, the results will be biased due to the position of the seismic source. It is difficult to obtain the geometry of the
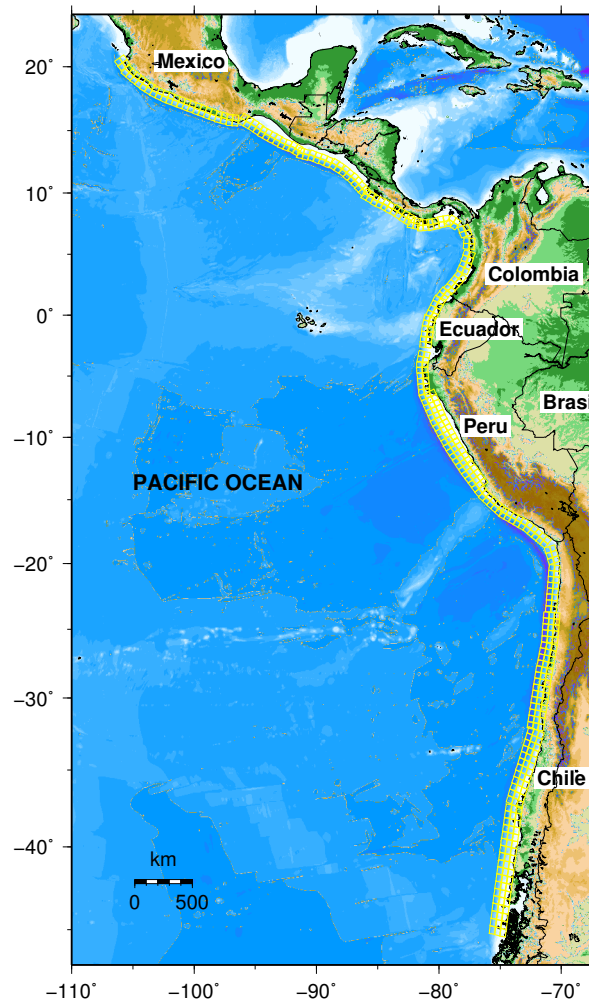
FIGURE 7.7: The unitary pre-calculated seismic sources are represented by the small yellow squares. It covers the subduction zone from northern Mexico to southern (Chile) with 465 seismic sources.

seismic source immediately after the occurrence of the earthquake; this issue can be resolved with the aftershock distribution, many hours later.

For the far field, the numerical model does not take into account the effects of dispersion, which is a non-linear effect. The model assumes homogeneous and regular deformation; the reality is that the seismic source can have a heterogeneous asperity distribution.

Strengths of the Model

The time that the application spends to provide the tsunami parameters is immediate, since it has a database of simulations previously computed. The model works well when the epicenter matches with the epicentroid or gravity center of the rupture geometry, as the case of Chile earthquake of 2014.

This model is applicable for seismic events in the near and regional field, due to the reaction time is in the order of a few minutes to one hour. On the other hand, for tsunamis in the far field, the forecaster has a greater reaction time, in the order of many hours.

The GUI (Graphical User Interface) is user friendly and easy to use by an operator (it is not necessary the operator be an expert in programming or numerical simulation). As a post-tsunami analysis, the Green functions of the model can be used to obtain the distribution of the seismic source, with an inversion calculation.

We have mentioned that this model requires the aftershock distribution to solve the location of the seismic source. Therefore, in a real application, the accuracy of this system without knowing the real rupture geometry is good, from the point of view of the tsunami early warning operator.

7.5 Conclusions

We have presented a numerical procedure to determine quickly the occurrence of a tsunami and to forecast some parameters: the arrival time of the front of the first tsunami wave and the maximum tsunami wave height in the different coastal cities. The application Pre-Tsunami is of practical use in the Peruvian Tsunami Warning Center.

The numerical model tries to reproduce a physical process (as is the process of interaction of tsunami waves near the coast) through a linear simulation model (as is the process of propagation of the tsunami) to use the principle of superposition of the Green functions. This could suggest the use of a linearity correction factor for each tidal station, which can be empirically calibrated and updated with each new tsunami event.

Despite the limitations of the model, the results are of practical use as a first approximation for purposes of fast estimation of tsunami parameters to issue the alerts and warnings of tsunamis in the near field, due to the speed with which the tsunami parameters are obtained.

The application of the model to the earthquake and tsunami in northern Chile 2014 (Mw 8.2) indicates a good correlation between the maximum heights of observed and simulated waves. In the case of tidal station of Arica, the error was 3.5%, Ilo's error was 5.7%, Callao's error was 12%, but the largest error was in Chimbote with 53.5%. We must take into account that the aim of the research is tsunami early warning, where speed is required rather than accuracy. Based on our results, we state an accuracy within 15% of error.

Chapter 8

Discussion and Conclusions

After having shown the theory and applications of the geophysical inversion method to obtain the distribution of the seismic source of tsunamigenic events in the region of Peru and northern Chile, this chapter discusses the important issues related to parameterization of the inversion process. Additionally, the future work to be carried out is described, for example the joint inversion of seismic waves, tsunami waves and geodetic data.

8.1 Discussion of important issues

In this section the effects of the main variables of the parameterization of the inversion process are discussed, such as the role of the number and dimensions of the subfaults: conditions for the choice of the minimum dimension of the subfault, the role of the time window of the signal to be inverted, the role of the azimuthal distribution of the gauge stations and the effects of numerical reflection of the wave at the open oceanic boundaries.

Role of the number of subfaults and their dimensions

The most critical parameter is the number of subfaults and their dimensions. A poor correlation between the observed and simulated signals may simply be the result of the sub-parametrization of the source. By dividing the geometry of the seismic source into smaller and more numerous subfaults, the inversion process is provided with more freedom, and the observed signals would have a better correlation, because short-period waves can be modeled in greater detail [Joh99].

It was found that this is an important factor in several studies. For example, in the case of the Chile 2014 earthquake, the simulation was initially carried out with 12 subfaults, then

with 20 and finally with 24 sub-sources, obtaining a better correlation in the latter case. This suggests that further subdivisions of the subfaults would improve the correlation between the observed and simulated signals. However, the dimensions of the subfaults can not be so small, but have a lower limit. According to the approximation of the linear hydrodynamic theory of shallow water, the relationship between the bathymetric depth h and the wavelength λ must be less than 1/20 to obtain an error less than 1% (Satake, 1987) [Sat87]. But, the wavelength λ is comparable to the dimension L of the subfault, therefore:

$$\frac{h}{L} < \frac{1}{20} \tag{8.1}$$

Considering an average bathymetric depth in the source region of $h = 1.5$ km, then the size of the subfault must be greater than $L = 30$ km. For dimensions smaller than 30 km, the error increases and there is a risk of losing linearity.

Role of the time window of the signal to be inverted

In general, the first wave period of the tsunami contains information about the physical processes in the seismic source. Parameters such as maximum amplitude and wavelength (of the first period) bear the stamp of the initial coseismic deformation.

In the case of offshore stations or DART buoys, there is no restriction regarding the size of the time window of the signal to be inverted, due to the linearity of the process and the absence of (non-linear) reflection effects in the coast and local resonances. For example, in the case of the Iquique-Chile earthquake in 2014, a time window with a duration of 90 minutes was used, which contained around 4 wavelengths (Figure 8.1).

However, in the case of gauge stations in coastal zones, only the first period of the wave in the inversion process should be used, because the subsequent waves would be contaminated with reflections due to the coast, local resonances in case of bays and other non-linear phenomena. For example, in the case of the Huacho-Perú earthquake of 1966 (8.1 Mw), a time window with a duration of 40 minutes (in the inversion process) was used, which covered a little more than one period of the tsunami waveform.

Role of azimuthal distribution of stations

The azimuthal distribution of the tide gauge and/or geodetic stations plays an important role in determining the distribution of the seismic source and the stability of the solution. A uniform azimuthal distribution around the source region is a necessary condition to obtain a reliable solution.
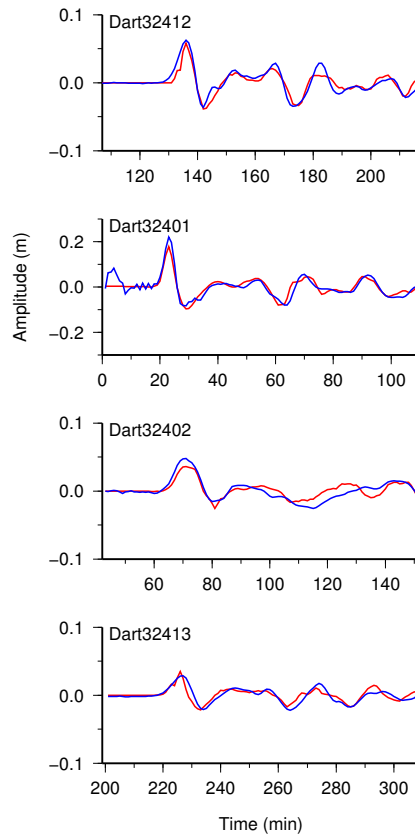
FIGURE 8.1: Comparison of waveforms of the 2014 Chilean tsunami: observed (blue) and synthetic (red). The time window is 90 min, covering around 4 periods of the wave.

Currently, the National Tidal Network of Peru is constituted by 19 operational coastal tide stations (www.dhn.mil.pe) (Figure 8.2). Additionally, in the Pacific Ocean, the DART program has installed more than 40 buoys offshore ("www.ndbc.noaa.gov/dart.shtml", last accessed: Dec 2017). This implies that for the next big earthquake that will occur in the central region of Peru, there will be good azimuthal coverage of tide gauge stations.

Unfortunately, for ancient tsunamigenic seismic events (such as the Huacho earthquake of 1966, for which only three tide gauge stations were available) or for small tsunamigenic events (Mw ~ 7.0), it is not always possible to have good azimuth coverage of stations. However, by means of a reliability test (such as the checkerboard test) it can be decided whether it is still possible to recover the distribution of the seismic source from only 3 or more tide gauge stations.

Effects of numerical reflection on open oceanic boundaries

A recurring problem in the numerical calculation is the design of artificial boundaries. How can a domain be numbered numerically, to keep the scale of calculations within reasonable limits, even until it ends with a solution that approximates the correct result for an unlimited
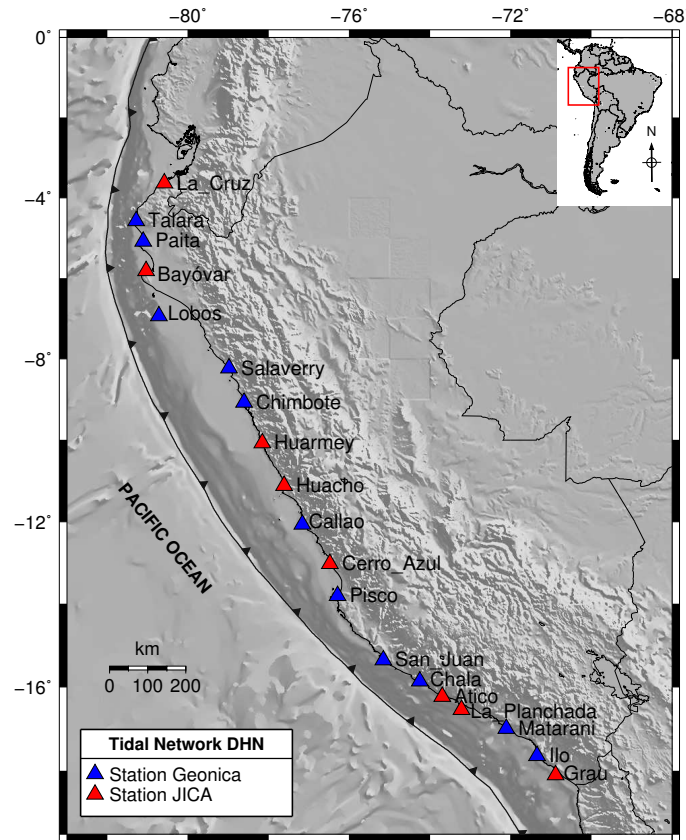
FIGURE 8.2: Location map of the stations of the National Mareographic Network of Peru.

domain? For example, in the calculation of the propagation of a tsunami, what should the conditions of open ocean borders be like to avoid numerical reflections?

One of the numerical methods for working with open or unlimited boundaries in numerical models is the method of the "sponge layer", where the idea is to surround the region of physical interest (usually open oceanic boundaries) with a layer of point grids in which the same equations are solved, except with an additional dissipative term to absorb the energy and, therefore, prevent numerical reflections at the boundaries. This "sponge layer" can have a width of 10 to 100 grids. For example, in some cases you could choose 100 grids: 50 within the domain and 50 outside the simulation domain (Figure 8.3).

Figure 8.4 shows a graph that represents the variation of the attenuation coefficient for the sponge layer that varies between 1 and 5. So in this layer, the value of the amplitude of the wave is attenuated by the inverse of such coefficient:

$$z(i,j) = \frac{z(i,j)}{spon(i)} \tag{8.2}$$

Where $z(i,j)$ represents the propagation of the wave, $spon(i)$ is the coefficient of the sponge layer in the i direction.

FIGURE 8.3: Limits of the absorbing layer or sponge (in red color). The black rectangle represents the limits of the computational grid. A virtual gauge has been placed: TG4.
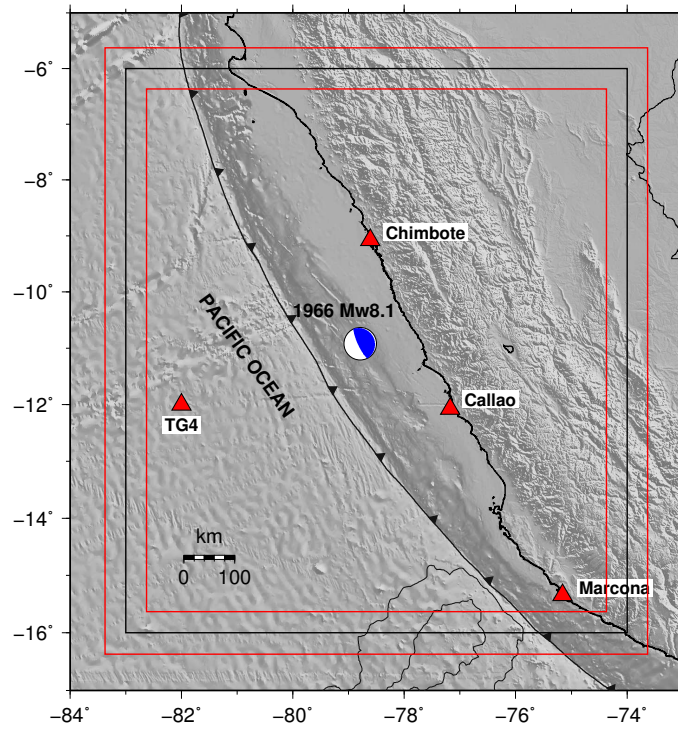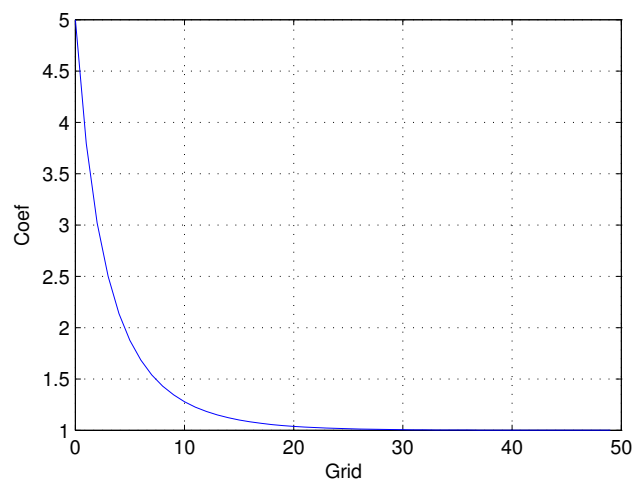

FIGURE 8.4: Coefficient of attenuation of the sponge layer.
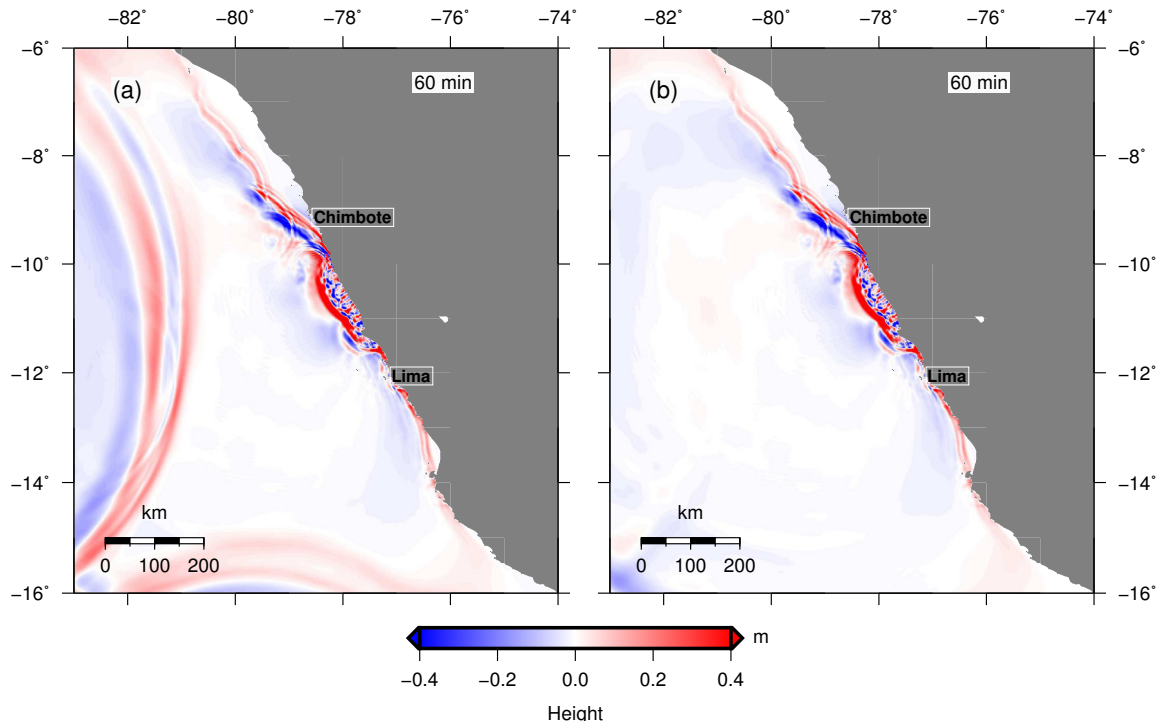
FIGURE 8.5: Propagation of the tsunami: a) Including the effect of reflection on the open oceanic edges. b) Excluding the effect of reflection on the oceanic edges, by means of a layer of the sponge type.

A fragment of the subroutine in the programming language Fortran that performs the simulation of the absorbing effect of the sponge layer for two dimensions, is shown below:

```
do j=1,je
    do i=1,50
        z(i,j,2) = z(i,j,2)/spo(i)
        z(ie+1-i,j,2) = z(ie+1-i,j,2)/spon(i)
        if (abs(z(i,j,2)) < gx) z(i,j,2) = 0.0
        if (abs(z(ie+1-i,j,2)) < gx) z(ie+1-i,j,2) = 0.0
    end do
end do
```

In Figure 8.5 (a) the effect of reflection on the tsunami wave propagation is observed; while in Figure 8.5 (b) the previous situation is observed but taking into account the effect of the sponge layer, which practically attenuated the numerical reflection of the wave at the open boundaries.

Figure 8.6 shows the waveforms for a TG4 virtual tide station, for the case of total reflection (without considering the effect of the sponge layer), for the case in which the sponge layer is considered, where the reflected wave has been almost totally attenuated and finally the residual is shown between both cases.
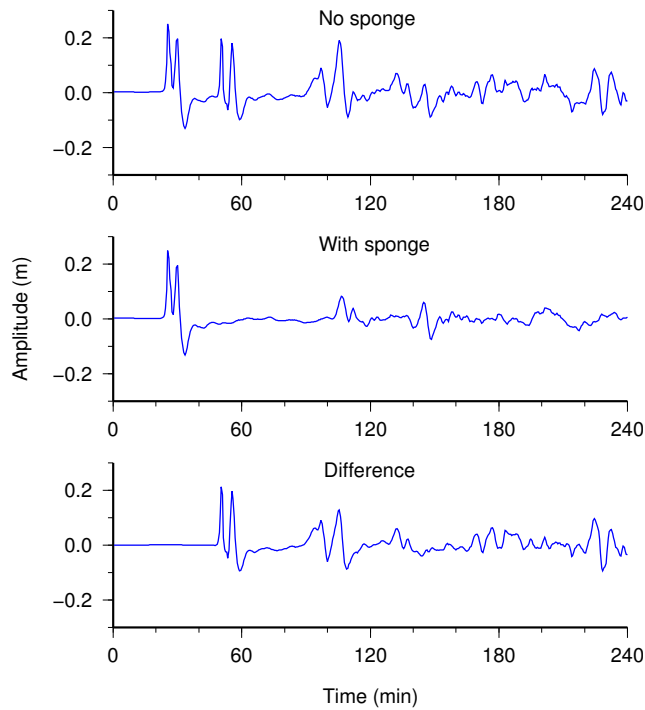
FIGURE 8.6: Comparison of the synthetic waveforms of the TG4 virtual gauge.

8.2 General conclusions

According to numerical experiment for the 1940 Lima tsunami, there is a good correlation between the simulated waves for the non-linear model and the linear model, only for the first period of the wave. This fact allows the use of the linear model in the inversion processes, for being of low "computational cost".

The joint inversion of 2 or more data sets provides better results because there is better control of the inversion process. Tsunami + Geodetic data inversion provides a better result than seismic data inversion.

The seismic source must be discretized with as many sub-sources as possible to obtain greater detail. According to the approximation of the linear theory of shallow water, it is required that: $h/L < 1/20$. Which implies that $L_{min} = 30$ km, in the case of Peru.

The time window of the tsunami waveform to be inverted is of one period of the wave, in the case of coast stations, due to non-linear effects. For buoys at offshore (DART), the time window to be inverted may include several periods due to the linearity of the tsunami wave propagation process.

It is important to have a good azimuthal coverage of stations; however, with only 3 stations (properly distributed) it is still possible to recover the distribution of the seismic source (as in the case of the 1966 Huacho tsunami).

The effect of "numerical reflection" on the open ocean boundaries can be effectively attenuated with the inclusion of an absorbent sponge layer, which absorbs the energy and linear momentum of the wave before reaching the open boundary.

The principle of superposition (for linear systems) allows the use of pre-simulated unit seismic sources to implement an early warning system to forecasting tsunami parameters (Pre-Tsunami software).

8.3 Future work

One subject to be investigated is the joint inversion of seismic waves (on the near and far field), tsunami waves and geodetic data (GPS + InSAR + observations in the coast of subsidence or uplift). The combination of all these dataset better constrain the seismic source model.

Of great help would be the contribution of the crustal deformation data from satellite images of radar interferometry (InSAR), since it would be possible to map the deformation in the region of the seismic source with a good spatial coverage on continent, but not in the ocean.

In the case of geodetic data, it is necessary to address the problem of correction by attenuation of the deformation with respect to the epicentral distance, which is the reason why in many studies has been obtained an underestimated seismic moment.

It would also be important to conduct an evaluation or reliability test of the model with synthetic data, in which a seismic source is simulated, obtaining the synthetic tsunami and displacements for the different stations. Then the inversion of the synthetic data is conducted and it is evaluated if the original distribution can be retrieved with a certain approximation.

References

[Abe72] Abe, K. (1972). Mechanism and tectonic implications of the 1966 and 1970 Peru earthquakes. Physics of the Earth and Planetary Interiors, vol 5, pp 367-379.

[Abe78] Abe, K. (1978). A dislocation model of the 1933 Sanriku earthquake consistent with tsunami waves. J. Phys. Earth, vol 26, No. 4, pp 381-396.

[Abe79] Abe, K. (1979). Size of Great Earthquakes of 1837-1974 inferred from tsunami data. JGR, vol 84, No. B4, pp 1561-1568.

[Adr16] Adriano, B., Mas, E., Koshimura, S., Fujii, Y., Yanagisawa, H. and Estrada, M. (2016). Revisiting the 2001 Peruvian Earthquake and Tsunami impact along Camana beach and the coastline using numerical modeling, doi 10.1007/978-3-319-28528-3-1.

[Aid69] Aida, I. (1969). Numerical experiments for the tsunami propagation of the 1964 Niigata tsunami and 1968 Tokachi-Oki tsunami. Bull. Earthq. Res. Inst. Univ. Tokyo, vol 47, No. 4, pp 673-700.

[Aki66] Aki, K. (1966). Estimation of earthquake moment, released energy, and stress-strain drop from the G wave spectrum. Bull. Earthquake Res. Inst. 44, 73-88.

[Alt11] Altamimi, Z., Collilieux, X. and Metivier, L. (2011). ITRF2008: an improved solution of the international terrestrial reference frame. Journal of Geodesy, vol 85, pp 457–473.

[Anc14] An, C., Sepúlveda, I. and P. L.-F. Liu (2014). Tsunami source and its validation of the 2014 Iquique, Chile Earthquake. GRL, vol 41, doi:10.1002/2014GL060567.

[Bar76] Barazangi, M. and Isacks, B. (1976). Spatial distribution of earthquakes and subduction of the Nazca plate beneath South America. Journal of Geology, vol 4, pp 686-692.

[Bar90] Barrientos, S. and Ward, S. (1990). The 1960 Chile earthquake: inversion for slip distribution from surface deformation. Geophysical Journal International, vol 103, pp 589–598.

[Bar14] Barrientos, S. (2014). Informe Técnico del Terremoto de Iquique, Mw=8.2 del 01 de abril de 2014. Centro Sismológico Nacional. Universidad de Chile.

[Bec89] Beck, S. and Ruff, L. (1989). Great earthquakes and subduction along the Peru trench. Physics of the Earth and Planetary Interiors, vol57, pp 199-224.

[Bec90] Beck, S. and Nishenko, S. (1990). Variations in the mode of great earthquake rupture along the Central Peru subduction zone. GRL, v 17, N 11, pp 1969-1972.

[Ble02] Blewitt, G. and D. Lavalle (2002). Effect of annual signals on geodetic velocity. JGR, 107(B7), 2145, doi:10.1029/2001JB000570.

[Car02] Carpio, J., Zamudio, Y. y Salas, H. (2002). Características generales del Tsunami asociado al terremoto de Arequipa del 23 de Junio 2001 (Mw=8.2). Instituto Geofísico del Perú, CNDG, pp 121-128.

[Chl11] Chlieh, M., Perfettini, H., Tavera, H., Avouac, J., Remy, D., Nocquet, J., Rolandone, F., Bondoux, F., Gabalda, G. and Bonvalot, S. (2011). Interseismic coupling and seismic potential along the Central Andes subduction zone. JGR, vol 116, (B12405), pp 21.

[Com91] Comte, D. and Pardo, M. (1991). Reappraisal of great historical earthquakes in the northern Chile and southern Peru seismic gaps. Natural Hazards, vol 4, pp 23-44.

[Dag08] D'Agostino, N., Avallone A., Cheloni, D., D'Anastasio, E., Mantenuto, S. and Selvaggi, G. (2008). Active tectonics of the Adriatic region from GPS and earthquake *slip* vectors. JGR, vol 113, B12413, doi:10.1029/2008JB005860.

[Dew79] Dewey, J. and Spence, W. (1979). Seismic gaps and zones of recent large earthquakes in coastal Peru. PAAG, vol117, pp 1148-1171.

[Dor90] Dorbath, L., Cisternas, A., Dorbath, C. (1990). Assesment of the size of large and great historical earthquakes in Peru. BSSA, Vol 80, No. 3, pp 551-576.

[Fri08] Fritz, H., Kalligeris, N., Borrero, J., Broncano, P. and Ortega, E. (2008). The 15 August 2007 Peru tsunami runup observations and modeling. GRL, vol 35, L10604.

[Fuj06] Fujii, Y. and Satake, K. (2006). Source of the July 2006 west Java tsunami estimated from tide gauges records. GRL, 41 (24), L24317.

[Fuj08] Fujii, Y. and Satake, K. (2008). Tsunami waveform inversion of the 2007 Bengkulu, southern Sumatra, earthquake. Earth Planets Space, vol 60, pp 993-998.

[Fuj12] Fujii, Y. and Satake, K. (2012). Slip distribution and Seismic Moment of the 2010 and 1960 Chilean Earthquakes inferred from Tsunami Waveforms and Coastal Geodetic Data. PAGEOPH, doi 10.1007/s00024-012-0524-2.

[Gic07] Gica, E., M. Teng, M. Asce, P. Liu, F. Asce, V. Titov and H. Zhou (2007). Sensitivity analysis of source parameters for earthquake generated distant tsunamis. Journal of Waterways, Port, Coasts and Ocean Engineering, 133:429–441.

[Gic08] Gica, E., Spillane, M., Titov, V., Chamberlin, C. and Newman, J. (2008). Development of the forecast propagation database for NOAA's short-term inundation forecast for Tsunamis (SIFT). NOAA Technical Memorandum OAR PMEL-139, pp 89.

[Gre11] Greenslade, D., Allen, S. and Simanjuntak, M. (2011). An Evaluation of Tsunami Forecasts from the T2 Scenario Database. PAGEOPH, vol 168, pp 1137-1151.

[Gus15] Gusman, A., Murotani, S., Satake, K., Heidarzadeh, M., Gunawan, E., Watada, S. and Schurr, B. (2015). Fault slip distribution of the 2014 Iquique Chiloe, earthquake estimated from ocean-wide tsunami waveform and GPS data. GRL, doi:10.1002/2014GL062604.

[Hei01] Heidarzadeh, M. and Satake, K. (2015). New insights into the Source of the Makran tsunami of 27 November 1945 from tsunami waveforms and coastal deformation data. PAAG, vol 172, No. 3, pp 621-640.

[Hen01] Henry, C. and Das, S. (2001). Aftershock zones of large shallow earthquakes: fault dimensions, aftershock area expansion and scalling relations. Geophyscial Journal International, vol 147, pp 272-293.

[Ide07] Ide, S. (2007). Slip Inversion. Treatise on Geophysics, vol 4, chap 7. pp 193-223. Elsevier.

[Ima96] Imamura, F. (1996). Review of tsunami simulation with a finite difference method. Long Wave Runup Models. World Scientific, pp 25-42.

[Ima06] Imamura, F., Yalciner, A. and Ozyurt G. (2006). Tsunami Modelling Manual (TU-NAMI model). Tohoku University, Japan. pp 58. Available on: http://www.tsunami.civil.tohoku.ac.jp/hokusai3/J/projects/manual-ver-3.1.pdf

[IOC97] Intergovernmental Oceanographic Commission (1997). TIME project numerical method of tsunami simulation. UNESCO, Paris.

[Iou13] Ioualalen, M., Perfettini, H., Yauri, S., Jiménez, C. and Tavera, H. (2013). Tsunami Modeling to Validate Slip Models of the 2007 Mw8.0 Pisco Earthquake, Central Peru. PAAG, DOI 10.1007/s00024-012-0608-z.

[Jic07] Ji Chen (2007). National Earthquake Information Center: earthquake.usgs.gov/earthquakes/eventpage/usp000fjta#finite-fault

[Jim07] Jiménez, C. (2007). Procesamiento digital de señales sísmicas con Matlab, Rev. Inv. Fis. vol 10, No. 2, pp 23.

[Jim10] Jiménez, C. (2010). Software para determinación de ocurrencia de maremotos. Boletín de la Sociedad Geológica del Perú. Vol 104, pp 25-31.

[Jim11] Jiménez, C., Adriano, B., Koshimura, S. and Fujii, Y. (2011). The Tsunami of Camana 2001. 8th CUEE Conference Proceedings, pp 1567-1571.

[Jim12] Jiménez, C., Moggiano, N., Saavedra, M. (2012). Fuente sísmica del terremoto de Pisco 2007 a partir de inversión de registros mareográficos. Revista de Investigación de Física, vol. 15, No. 2.

[Jim13] Jiménez, C., Moggiano, N., Mas, E., Adriano, B., Koshimura, S., Fujii, Y. and Yanagisawa, H. (2013). Seismic source of 1746 Callao Earthquake from tsunami numerical modelling, JDR, vol 8, No. 2, pp 266-273.

[Jim14] Jiménez, C., Moggiano, N., Mas, E., Adriano, B., Fujii, Y. and Koshimura, S. (2014). Tsunami waveform inversion of the 2007 Peru (8.1 Mw) earthquake. JDR, vol 9, No. 6, pp 954-969.

[Jim16] Jiménez, C., Moggiano, N.,Yauri, S. y Calvo, M. (2016). Fuente sísmica del terremoto de Huacho-Perú 1966 de 8.1 Mw a partir de inversión de registros mareográficos. Rev. Inv. Fis. vol 19, No. 1, pp 9.

[Jim18] Jiménez, C., Carbonel, C. and Rojas, J. (2018). Numerical Procedure to Forecast the Tsunami Parameters from a Database of Pre-Simulated Seismic Units Sources. PAAG, vol 175, pp 1473-1483.

[Jim18b] Jiménez, C. (2018). Seismic source characteristics of the intraslab 2017 Chiapas-Mexico earthquake (Mw8.2). Physics of the Earth and Planetary Int, vol 280, pp 69-75.

[Joh97] Johnson J., and Satake K. (1997). Asperity Distribution of Alaskan-Aleutian Earthquakes: Implications for Seismic and Tsunami Hazards. In: Hebenstreit G. (eds) Perspectives on Tsunami Hazard Reduction. vol 9. pp 67-81. Springer.

[Joh99] Johnson, J. (1999). Heterogeneous coupling along Alaska-Aleutians as inferred from tsunami, seismic and geodetic inversions. Advances in Geophysics, vol 39, pp 116.

[Jor02] Jordanovski, L. and Todorovska, M. (2002). Inverse studies of the earthquake source mechanism from near-field strong motion records. Journal of Earthquake Technology, vol 39, No. 1-2, pp 73-91.

[Kan77] Kanamori, H. (1977). The energy release in great earthquakes. Journal of Geophysical Research, vol 82, pp 2981-2987.

[Kau86] Kausel E. (1986). Los terremotos de Agosto de 1868 y Mayo de 1877 que afectaron el sur del Perú y norte de Chile. Bol. Acad. Chil. Cienc., vol 3, pp 8–12.

[Kel72] Kelleher, J. (1972). Rupture zones of large South American earthquakes and some predictions. Journal of Geophysical Research, vol 27, pp 2087-2103.

[Ken03] Kendrick, E., Bevis, M., Smalley, R., Brooks, B., Barriga, R., Lauria, E and Souto, L. (2003). The Nazca South America Euler vector and its rate of change. Journal of South American Earth Sciences, vol 16, pp 125-131.

[Kik91] Kikuchi, M. and Kanamori, H. (1991). Inversion of Complex Body Waves III. BSSA, vol 81, No. 6, pp 2335-2350.

[Kik93] Kikuchi, M., Kanamori, H. and Satake, K. (1993). Journal of Geophysical Research, vol 98, No. B9, pp 15797-15808.

[Kik01] Kikuchi, M. and Yamanaka, Y. (2001). Near coast of Peru earthquake (Mw 8.2) on June 23, 2001. EIC seismological note No. 105, http://wwweic.eri.u-tokyo.ac.jp/topics/200106232033/index.html

[Lan95] Langer, C. and Spence, W. (1995). The 1974 Peru Earthquake Series. BSSA, vol 85, No. 3, pp 665–687.

[Law74] Lawson, C. y Hanson, R. (1974). Solving least squares problems. Prentice–Hall, New York.

[Lay95] Lay, T. and Wallace, T. (1995). Modern Global Seismology. International Geophysics Series, vol 58, pp 535.

[Lay10] Lay, T., Ammon, C., Kanamori, H., Koper, K., Sufri, O., and Hutko, A. (2010). Teleseismic inversion for rupture process of the 27 February 2010 Chile (Mw8.8) earthquake. Geophysical Research Letters, vol 37, L13301.

[Lay14] Lay, T., Yue, H., Brodsky, E. and An, C. (2014). The 1 April 2014 Iquique, Chile, Mw 8.1 earthquake rupture sequence. GRL, vol 41, pp 3818–3825.

[Lev16] Levin, B. y Nosov, M. (2016). Physics of Tsunamis (2nd Edition), Springer International Publishing, New York.

[Lom68] Lomnitz, C. and Cabré, R. (1968). The Peru earthquake of October 17, 1966. Bulletin of the Seismological Society of America, vol 58, pp 645-661.

[Lut00] Luth, S. (2000). Results of wide angle investigations and curstal structure along a traverse across the Central Andes at -21°. Free University of Berlin, Germany.

[Liu98] Liu, P. Woo, S. and Cho, Y. (1998). Computer programs for tsunami propagation and inundation. Technical report, Cornell University, 104 pp.

[Mad98] Madariaga, H. (1998). Sismicidad de Chile (Spanish). Fisica de la Tierra, vol 10, pp 221-258.

[Loc85] Lockridge, P. (1985). Tsunamis in Peru-Chile. National Geophysical Data Center, Report SE-39, pp 97.

[Mas14a] Mas, E., Adriano, B., Kuroiwa, J. and Koshimura, S. (2014 a). Reconstruction Process and Social Issues after the 1746 Earthquake and Tsunami in Peru: Past and Present Challenges After Tsunami Events. In Post Tsunami Hazards, vol 44, pp 97-109.

[Mas14b] Mas E., Adriano, B., Pulido, N., Jimenez, C. and Koshimura, S. (2014 b). Simulation of Tsunami Inundation in Central Peru from Future Megathrust Earthquake Scenarios. JDR, vol 9, No. 6, pp 961-967.

[Men89] Menke, W. (1989). Geophysical data analysis: Discrete Inverse Theory. Academic Press, INC, San Diego, USA.

[Men18] Menke, W. (2018). Geophysical data analysis: Discrete Inverse Theory (4th Edition). Academic Press, Elsevier Inc. USA.

[Met13] Metois, M., Soquet, A. and Vigny, C. (2013). Revisiting the north Chile seismic gap segmentation using GPS derived interseismic coupling. Geophys. Journal International, doi: 10.10937gji/ggt183.

[Mor12] Moreno, M., Melnick, D., Rosenau, M., Baez, J., Klotz, J., Oncken, O., Tassara, A., Chen, J., Bataille, K., Bevis, M., Socquet, A., Bolte, J., Vigny, C., Brooks, B., Ryder, I., Grund, V., Smalley, B., Carrizo, D., Bartsch, M. and Hase, H. (2012). Toward understanding tectonic control on the Mw8.8 2010 Maule Chile earthquake. Earth and Planetary Science Letters, vol 321-322, pp 152-165.

[Mur75] Murty, T. and Wigen, S. (1975). Tsunami Water Levels and Spectra for Peru (tide gage recordings). Tsunami Newsletter, Vol. 8, No. 1, pp 2- 17.

[Nor98] Norabuena, E., Leffler, L., Mao, A., Dixon, T., Stein, S., Sacks, S., Ocola, L. and Ellis, M. (1998). Space Geodetic Observations of Nazca-South America Convergence across the Central Andes. Science, vol 279, pp 358.

[Nor99] Norabuena, E., Dixon, T., Stein, S. and Harrison, C. (1999). Deceleration and Nazca-Pacific plate motions. GRL, vol 26, pp 3405.

[Oco07] Ocola, L. (2007). Aspectos físicos del maremoto de Pisco del 15 de agosto de 2007 y las inundaciones máximas. El terremoto de Pisco del 15 de agosto de 2007 (7.9 Mw). Instituto Geofísico del Perú.

[Oco08] Ocola, L. (2008). Southern Peru coseismic subsidence: 23 June 8.4 Mw earthquake. Advances in Geosciences, vol 14, pp 79-83.

[Oka85] Okada, Y. (1985). Surface deformation due to shear and tensile faults in a half-space. Bulletin of the Seismological Society of America, vol 75, No. 4, pp 1135-1154.

[Oka92] Okada, Y. (1992). Internal deformation due to shear and tensile faults in a half space. BSSA, Vol. 82, No. 2, pp 1018-1040.

[Oka02] Okal, E., Dengler, L., Araya, S., Borrero, J., Gomer, B., Koshimura, S., Laos, G., Olcese, D., Ortiz, M. (2002). Field survey of the Camana, Peru Tsunami of 23 June 2001. Seismological Rsearch Letters, vol 73, No. 6, pp 907-920.

[Oka06] Okal, E., Borrero, J. and Synolakis, C. (2006). Evaluation of Tsunami Risk from Regional Earthquakes at Pisco, Peru. BSSA, vol 96, No. 5, pp 1634-1648.

[Oka09] Okal, E. (2009). Excitation of Tsunamis by Earthquakes, chapter V, pp. 137 – 177. The Sea: Tsunamis, volume 15. Harvard University Press. London.

[Opp97] Oppenheim, A. (1997). Signals and Systems, 2nd Edition. Prentice–Hall, New York.

[Pap04] Papazachos, B., Scordilis, E., Panagiotopoulos D., Karakaisis, G. (2004). Global relations between seismic fault parameters and moment magnitude of Earthquakes. Bulletin of the Geological Society of Greece vol. XXXVI, p. 1482-1489.

[Par74] Pararas-Carayannis, G. (1974). An Investigation of Tsunami Source Mechanism off the Coast of Central Peru. Marine Geology, vol 17, pp 235-247.

[Per10] Perfettini, H., Avouac, J., Tavera, H., Kositsky, A. (2010). Seismic and aseismic slip on the Central Peru megathrust. Nature, vol 465, pp 78-81.

[Pri07] Pritchard, M., Norabuena, E., Ji, C., Boroschek, R., Comte, D., Simons, M, Dixon, T. and Rosen, P. (2007). Geodetic, teleseismic and strong motion constraints on slip from recent southern Peru subduction zone earthquakes. JGR, vol 112, B03307, pp 24.

[Rav06] Rabinovich, A., Thomson, R. y Stephenson, F. (2006). The Sumatra tsunami of 26 December 2004 as observed in the North Pacific and North Atlantic oceans. Surv. Geophys. **27**, 647.

[Ren18] Ren, Z., Ji, X., Hou, J., Shan, D. and Zhao, L. (2018). Source inversion and numerical simulation of 2017 Mw 8.1 Mexico earthquake and tsunami. Natural Hazards, vol 94, No. 3, pp 1163-1185.

[Rob06] Robinson, D., Das, S. and Watts, A. (2006). Earthquake Rupture Stalled by a Subducting Fracture Zone. Science, vol 312, pp 1203-1205.

[Rom09] Romano, F. (2009). The rupture process of recent tsunamigenic earthquakes by geophysical data inversion. Universita di Bologna, PhD Thesis.

[Rui14] Ruiz, S., Metois, M., Fuenzalida, A., Ruiz, J., Leyton, F., Grandin, R., Vigny, C., Madariaga, R. and Campos, J. (2014). Intense foreshocks and a slow slip event preceded the 2014 Iquique Mw 8.1 earthquake. Sience, doi: 10.1126/science.1256074.

[Sat87] Satake, K. (1987). Inversion of Tsunami Waveform for the Estimation of a fault heterogeneity: method and numerical experiment. J. Phys. Earth, vol 35, pp 241-254.

[Sat91] Satake, K., Kanamori, H. (1991). Use of Tsunami Waveform for Earthquake Source Study. Natural Hazards, vol 4, pp 193-208.

[Sat93] Satake, K. (1993). Depth distribution of coseismic slip along tyhe Nankai Trough, Japan, from joint inversion of geodetic and tsunami data. JGR, vol 98, No. B3, pp 4553-4565.

[Sat95] Satake, K. (1995). Linear and non linear computations of the 1992 Nicaragua earthquake tsunami. PAAG, vol 144, No. 3-4, pp 455-470.

[Sch14] Schurr, B., Asch, G., Hainzl, S., Bedford, J., Hoechner, A., Palo, M., Wang, R., Moreno, M. (2014). Gradual unlocking of plate boundary controlled initiation of the 2014 Iquique earthquake. Nature, vol 512, pp 299–302.

[Shi12] Shi, F., Kirby, J. and Tehranirad, B. (2012). Tsunami benchmark results for spherical coordinate of FUNWAVE-TDV (version 2.0). Research Report, No. CACR-12-02, Center for Applied Coastal Research, University of Delaware.

[Sil78] Silgado, E. (1978). Historia de los sismos más notables ocurridos en el Perú (1513-1974). Instituto de Geología y Minería, Lima.

[Sla10] Sladen, A., Tavera, H., Simons, M., Avouac, J., Konca, A., Perfettini, H., Audin, L., Fielding, E., Ortega, F. and Cavagnoud, R. (2010). Source model of the 2007 Mw 8.0 Pisco, Peru earthquake. JGR, Vol. 115, B02405.

[Sla10b] Sladen, A. (2010). A coseismic distributed slip model for the 2010 Mw 8.8 Maule (Chile) earthquake. Proceedings: Chapman Conference on Giant Earthquakes and their Tsunamis. Chile.

[Ste03] Stein, S. and Wysession, M. (2003). Introduction to seismology, earthquakes and earth structure. Blackwell Publishing, Oxford, pp 498.

[Sup10] Suppasri, A., Imamura, F. and Koshimura, S. (2010). Effects of the rupture velocity of fault motion. Coastal Engineering J. vol 52, No. 2, pp 107.

[Tar05] Tarantola, A. (2005). Inverse problem theory and methods for model parameter estimation. Ed. Society for Industrial and Applied Mathematics, Philadelfia.

[Tav01] Tavera, H. and Buforn, E. (2001). Source mechanism of earthquakes in Peru. Journal of Seismology, vol 5 pp 519-539.

[Tav02] Tavera, H. Buforn, E., Bernal, I., Antayhua, Y. and Vilcapoma, L. (2002). The Arequipa (Peru) earthquake of June 23, 2001. Journal of Seismology, vol 6 pp 279-283.

[Tav08] Tavera, H. y Bernal, I. (2008). The Pisco (Perú) Earthquake of 15 August 2007. Seismological Res. Lett. vol 79, No. 4, pp 510.

[Tic89] Tichelaar, B. and Ruff, L. (1989). How good are our best models? EOS, Vol 70, No. 20, pp 593, 605-606.

[Tit03] Titov, V., Gonzalez, F., Mojfeld, H. and Venturato, A (2003). NOAA time Seattle tsunami mapping project: procedures, data sources and products. NOAA Technical Memorandum OAR PMEL-124, 21 pp.

[Udi14] Udías, A., Madariaga, R. and Buforn, E. (2014). Source Mechanism of Earthquakes: Theory and Practice. Cambridge University Press, 1st Edition, pp 302. United Kingdom.

[Vig11] Vigny, C., Socquet, A., Peyrat, S., Ruegg, J., Metois, M., Madariaga, R. (2011). The 2010 Mw8.8 Maule Megathrust Earthquake of Central Chile Monitored by GPS. Science, 332:1417.

[Vil09] Villegas, J. (2009). Modelos de velocidad unidimensional para las regiones norte, centro y sur de Perú. Tesis de Grado, UNSA, Perú.

[Vil14] Villegas, J. (2014). Earthquake cycle and continental deformation along the Peruvian subduction zone. PhD Thesis, University of Nice-Sophia, pp 164.

[Vil16] Villegas, J. (2016). Active tectonics of Peru: Heterogeneous interseismic coupling along the Nazca megathrust, rigid motion of the Peruvian Sliver and subandean shortening accomodation. JGR, doi 10.1002/2016JB013080, pp 24.

[Wan03] Wang, R., Lorenzo, M. and Roth, F. (2003). Computation of deformation induced by earthquakes in a multilayer elastic crust - Fortran programs EDGRN/EDCMP. Computers and Geosciences, vol 29, pp 195-207.

[Wan06] Wang, R., Lorenzo, F. and Roth F. (2006). PSGRN/PSCMP a new code for calculating co and postseismic deformation, geoid and gravity changes based on the viscoelastic gravitational dislocation theory. Computers and Geosciences vol 32, pp 527-541.

[Wan12] Wang, K., Hu, Y. and He, J. (2012). Deformation cycles of subduction earthquakes in a viscoelastic Earth. Nature, vol 484, pp 327-332.

[Wil08] Williams, S. (2008). CATS: GPS coordinate time series analysis software, GPS solutions, 12(2), pp 147–153.

[Yag14] Yagi, Y., Okuwaki, R., Enescu, B., Hirano, S., Yamagami, Y., Endo, S. and Komoro, T. (2014). Rupture process of the 2014 Iquique Chile earthquake in relation with the foreshock activity. GRL, vol 41, pp 4201-4206, doi:10.1002/2014GL060274.

[Yam09] Yamazaki, Y., Kowalik, Z., Cheung, K. (2009). Depth-integrated, non hydrostatic model for wave breaking and run-up. Int. J. Numer. Methods Fluids, 61, 473-497 pp.